MONASH University

P-band Microwave Radiometry and Soil Moisture Retrieval

Xiaoji Shen

MSc in Geography

BSc in Geographic Information Science

A thesis submitted for the degree of Doctor of Philosophy at
Monash University in 2022
Department of Civil Engineering

Copyright Notice

This page is intentionally left blank.

To my mother,

with love and gratitude.

This page is intentionally left blank.

Abstract

It has been over ten years since the successful launch of the first-ever dedicated satellite for global soil moisture monitoring; Soil Moisture and Ocean Salinity (SMOS). Looking towards the future, P-band (0.3-1 GHz) is a promising technique to replace or enhance the L-band (1.4 GHz) SMOS and SMAP (Soil Moisture Active Passive) missions, because of the expected greater moisture retrieval depth and reduced impact from surface roughness and vegetation as a result of its lower frequency. However, there has been no observational evidence in P-band radiometry to demonstrate the above-postulated benefits. Accordingly, this research has established a long-term (2017-2021) tower-based experiment known as the P-band Radiometer Inferred Soil Moisture (PRISM, see https://www.prism.monash.edu) tower project, for undertaking a comprehensive evaluation of a P-band radiometer at 0.75 GHz in soil moisture remote sensing under a range of moisture, roughness, and vegetation conditions. This study therefore aimed to pave the way for a successful P-band radiometer-based mission to obtain deeper and more accurate global soil moisture information. The findings of this research are summarized here from the aspects of moisture retrieval depth, roughness effects, and vegetation effects.

This research proposed a model to estimate moisture retrieval depth by utilizing the coherent radiative transfer model and the Fresnel equations, with the results being subsequently compared to empirical evidence from tower-based observations. Both predictions and observations agreed that P-band has the potential to retrieve soil moisture over a deeper layer than L-band, being ~7 cm rather than ~5 cm for the wavelength and conditions observed. The results also demonstrated that moisture retrieval depth is expected to increase with further increases in wavelength, with the potential to achieve a moisture retrieval depth greater than 10 cm for P-band below 0.5 GHz.

In terms of soil roughness, P-band was compared with L-band over bare flat and periodic soil surfaces. Physical simulations based upon the Improved Integral Equation Model demonstrated that P-band was less impacted by random roughness

than L-band. Moreover, the potential to retrieve soil moisture without discriminating periodic and flat surfaces was investigated by applying the roughness parameters calibrated for flat soil to retrieve the moisture of periodically rough soil. The results showed that soils with periodic surface profiles needed to be discriminated at L-band but not at P-band due to the reduced impact at P-band, supported by the more comparable RMSE at P-band (variation of up to 0.012 m^3/m^3) than L-band (variation of up to 0.022 m^3/m^3) across different roughness configurations.

For vegetation, the tau-omega model was evaluated at P- and L-band over bare and wheat-covered flat and periodic soil surfaces. Comparable RMSE values across these different surfaces at both P- and L-band indicated that the periodic surfaces did not need to be discriminated when the vegetation canopy "masked" the roughness structure underneath. Moreover, a reduced vegetation impact at P-band was demonstrated, with an RMSE of 0.029 m^3/m^3 achieved when completely ignoring the wheat existence with under 4-kg/m^2 vegetation water content, whereas at L-band the RMSE increased to 0.063 m^3/m^3. Soil moisture retrieval was also carried out over a much denser corn canopy with up to 20-kg/m^2 vegetation water content when accounting for vegetation impact using the tau-omega model. The RMSE at P-band was found to be around 0.062 - 0.079 m^3/m^3, which was considered acceptable given the extremely high vegetation water content. Conversely, L-band was unable to sense the soil moisture beneath such a dense corn canopy at an acceptable accuracy, with RMSE higher than 0.1 m^3/m^3.

Declaration

This thesis is an original work of my research and contains no material which has been accepted for the award of any other degree or diploma at any university or equivalent institution and that, to the best of my knowledge and belief, this thesis contains no material previously published or written by another person, except where due reference is made in the text of the thesis.

Print Name: Xiaoji Shen

Date: 23/01/2022

This page is intentionally left blank.

Acknowledgments

It has been a long and at times daunting journey for the past three years and five months. This thesis would not have been possible without the inspiration and support of a number of great individuals.

I owe my deepest gratitude to my main supervisor Prof. Jeffrey Walker, who is always ready to provide me with his immense knowledge and generous support. I feel so fortunate to have Jeff as my supervisor for letting me understand what a good scientist and supervisor is supposed to be. I have benefited greatly from his excellent self-management, coordination, and critical thinking skills, leading to the preparedness to be an independent academic. Moreover, he always patiently provides detailed changes and suggestions on every sentence on the paper drafts and milestone reports I sent him. I have carefully archived all of them and will refer to them whenever I am unsure about making a statement.

I gratefully acknowledge the contributions of my co-supervisor A/Prof. In-Young Yeo for her insightful comments on this thesis from a hydrologist's view. I also express my warmest appreciation to my PhD review panel Dr. Jean-Pierre Wigneron, A/Prof. Valentijn Pauwels, and A/Prof. Edoardo Daly for their constructive suggestions. I would also like to thank my collaborators Dr. Edward Kim, Dr. Yann Kerr, and Dr. Thomas Jackson, who provided insightful suggestions and comments towards the publication of several journal papers.

It is a pleasure to thank my dear friends and group-mates Nan Ye, Liujun Zhu, Xiaoling Wu, Ying Gao, Adrien Guyot, Chaoxun Hang, Stefania Grimaldi, Nithyapriya Boopathi, Yuxi Zhang, Linlin Zhang, Foad Brakhasi, Rahul Raj, Elaheh Ghafari, Thi Mai Nguyen, Jaya Pudashine, Yuval Sadeh, Antara Dasgupta, Amir Tophel, Louis Jalenques, Richa Prajapati, Luisa White Murillo, Lixiaozhou Zhou, and Ziwei Xiong for making this lengthy PhD journey exciting and memorable. I would like to extend my thanks to my housemates Nan Ye and Liujun Zhu, who are like my elder brothers and accompany me in both life and research at U2 2027 Dandenong Rd.

Special gratitude goes to Xiaoling Wu and Luisa White Murillo for taking care of the experimental site and collecting data for me when I was away from Melbourne. I also wish to thank my colleagues Pascal Mater, Kiri Mason, Gordon Privitera, and Sarvan Mani for their help with the experimental equipment and site maintenance. Thanks also to Mr. Wayne Tymensen for kindly providing the land for the experiment site.

Finally, my deep and sincere gratitude goes to my beloved family and my partner, Jingya, for their continuous and unparalleled love, help, and support. They selflessly encouraged me to explore new directions in life and seek my destiny, and therefore I dedicate this milestone to them.

Table of Contents

List of Symbols

Symbols	Units	Definitions
b	[Np·m^2/kg]	Empirical vegetation parameter
e	-	Emissivity
$e^{\sin}$	-	Emissivity of sinusoidal surfaces
f	[Hz]	Frequency
f_P	-	Fractional absorption
k	[m^{-1}]	Free space wavenumber
l	[cm]	Correlation length
m	-	Slope parameter
n	-	Refractive index
s	[cm]	Root-mean-square height
tt	-	Vegetation structural parameter
z	[m]	Soil depth
A	[m]	Surface amplitude
C	[%]	Clay content
H_R	-	Roughness intensity parameter
N_R	-	Roughness parameter characterizing polarization and angle dependence
P	-	Polarization
Q_R	-	Polarization mixing factor
R	-	Correlation coefficient

$\mathrm{SM_v}$	[m^3/m^3]	Volumetric soil moisture
SM_s	[m^3/m^3]	Moisture content at the soil surface
T	[K]	Physical temperature
T_{depth}	[K]	Physical temperature of deep soil
$T_{\mathrm{eff}}^{\mathrm{s}}$	[K]	Effective soil temperature
$T_{\mathrm{eff}}^{\mathrm{v}}$	[K]	Effective vegetation temperature
T_{surf}	[K]	Physical temperature of soil surface
Z	[m]	Surface height
α	-	Power absorption coefficient
β	[cm^{-1}]	Moisture gradient of the profile
θ	[°]	Incidence angle
θ_s	[°]	Zenith of the scattering direction
κ	-	Normalized attenuation coefficient
λ	[m]	Wavelength
σ	-	Standard deviation
τ	[Np]	Vegetation optical depth
τ_{NAD}	[Np]	Vegetation optical depth at nadir
ω	-	Vegetation single scattering albedo
ϕ	[°]	Azimuth of the incident direction
ϕ_s	[°]	Azimuth of the scattering direction
γ_P	-	Vegetation transmissivity
δ_m	[m]	Moisture retrieval depth

δ_t	[m]	Temperature sensing depth
ε_r	-	Complex relative dielectric constant
ε_r'	-	Real part of the complex relative dielectric constant
ε_r''	-	Imaginary part of the complex relative dielectric constant
ρ_b	[g/cm^3]	Soil bulk density
σ^s	[dB]	Bistatic scattering coefficient
Γ	-	Reflectivity
Γ^*	-	Specular reflectivity
Γ^{coh}	-	Coherent soil surface reflectivity
Γ^{non}	-	Noncoherent soil surface reflectivity
$\Delta\mathrm{SM}$	[m^3/m^3]	Increment of moisture with depth
$\Delta\Gamma$	-	Magnitude of depolarization effect
Λ	[m]	Surface spatial period

This page is intentionally left blank.

List of Abbreviations

Abbreviations	Full Names
2S Model	Two-Stream Model
AIEM	Advanced Integral Equation Model
AirMOSS	Airborne Microwave Observatory of Subcanopy and Subsurface
ALOS	Advanced Land Observing Satellite
AMSR-E	Advanced Microwave Scanning Radiometer - Earth Observing System sensor
ATBD	Algorithm Theoretical Baseline Document
CCI	Climate Change Initiative
CF	Cost Function
CIMR	Copernicus Imaging Microwave Radiometer
CRNP	Cosmic-Ray Neutron Probes
dB	Decibels
DCA	Dual Channel Algorithm
DMSP	Defense Meteorological Satellite Program
DoI	Degree of Information
ECMWF	European Centre for Medium-Range Weather Forecasts
E-DCA	Extended Dual Channel Algorithm
EM	Electromagnetic
ESA	European Space Agency

GCOM-W	Global Change Observation Mission - Water "SHIZUKU"
GIS	Geographic Information System
GNSS	Global Navigation Satellite System
GPR	Ground Penetrating Radar
GPS	Global Position System
GRACE	Gravity Recovery and Climate Experiment
GSMDB	Global Soil Moisture Data Bank
HDAS	Hydra-probe Data Acquisition System
I^2EM	Improved Integral Equation Model
IEM	Integral Equation Model
ISMN	International Soil Moisture Network
JPL	Jet Propulsion Laboratory
LAI	Leaf Area Index
L-MEB	L-band Microwave Emission of the Biosphere
LPRM	Land Parameter Retrieval Model
MEMLS	Microwave Emission Model for Layered Snowpack
MODIS	Moderate Resolution Imaging Spectroradiometer
MPDI	Microwave Polarization Difference Index
MT-DCA	Multi-Temporal Dual Channel Algorithm
NASA	National Aeronautics and Space Administration
NDVI	Normalized Difference Vegetation Index
NDWI	Normalized Difference Water Index

NMM3D	Numerical Maxwell Model in 3-D Simulations
PLMR	Polarimetric L-band Multi-beam Radiometer
P-MEB	P-band Microwave Emission of the Biosphere
PPMR	Polarimetric P-band Multi-beam Radiometer
PRISM	P-band Radiometer Inferred Soil Moisture
QA4SM	Quality Assurance for Soil Moisture
RAMSES	Radar Aéroporté Multi-spectral d'Etude des Signatures
RFI	Radio Frequency Interference
RMS	Root Mean Square
RMSE	Root Mean Squared Error
SAOCOM	Satélite Argentino de Observación COn Microondas
SAR	Synthetic Aperture Radar
SCA	Single Channel Algorithm
SM	Soil Moisture
SMAP	Soil Moisture Active Passive
SMAP L2SMP	SMAP Level 2 Soil Moisture Passive
SMAPEx	Soil Moisture Active Passive Experiment
SMOS	Soil Moisture and Ocean Salinity
SMOS-HR	Soil Moisture and Ocean Salinity - High Resolution
SNoOPI	SigNals of Opportunity: P-band Investigation
TRMM	Tropical Rainfall Measuring Mission
TWRS	Terrestrial Water Resources Satellite
UAVSAR	Uninhabited Aerial Vehicle SAR

ubRMSE	unbiased Root Mean Squared Error
UWBRAD	The Ultra-Wideband Software Defined Microwave Radiometer
VWC	Vegetation Water Content
WCOM	Water Cycle Observation Mission

List of Figures

This page is intentionally left blank.

List of Tables

This page is intentionally left blank.

1 Introduction

This thesis is the first investigation that compared P-band (~40-cm wavelength/0.75 GHz) and L-band (~21-cm wavelength/1.41 GHz) radiometers in parallel using a long-term tower-based experiment site in Victoria, Australia, where various moisture, roughness, and vegetation configurations were covered, to determine if there is an improvement in soil moisture sensing capability at P-band due to the expected greater moisture retrieval depth and reduced roughness and vegetation impact when using a longer wavelength. This thesis is the first investigation that P- and L-band radiometers were compared in parallel. Although the footprints of P- and L-band radiometers were not completely overlapped when using the same incidence angle, potentially leading to slight uncertainties to this research, this thesis paves the way for a successful P-band mission in the future for sensing deeper and more accurate soil moisture from space.

1.1 Background

The amount of water in the Earth's soil is around just 17,000 km^3 (Oki and Kanae, 2006), merely accounting for 0.05% of the total freshwater and 0.001% of the total water on/in the Earth (Shiklomanov, 1993). However, this small amount of water plays a crucial role in the Earth system because it nourishes vegetation, animals, and billions of humans. Moreover, soil moisture (SM) is a key parameter in the hydrological cycle that influences infiltration, runoff, and evapotranspiration (Seneviratne et al., 2010). Furthermore, it controls the division of the available energy at the land surface into sensible and latent heat fluxes (Koster et al., 2004).

Measuring soil moisture is challenging because of its high variability across temporal and spatial scale due to the heterogeneity of soil properties, topography, rainfall, and land cover characteristics (Owe et al., 2008). Over the past four decades, researchers have conducted numerous ground-, air- and space-based near-surface soil moisture remote sensing studies using visible (Liu et al., 2002, Lobell and Asner, 2002), thermal-infrared (Maltese et al., 2013a, Maltese et al., 2013b, Zhang and Zhou, 2016), active

microwave (Panciera et al., 2014, Zhu et al., 2019a, Zhu et al., 2019b, Zhu et al., 2020) and passive microwave (Wigneron et al., 1995, Panciera et al., 2009b, Zhao et al., 2020b).

Microwave is the region of electromagnetic (EM) spectrum ranging approximately from 1 mm to 1 m in wavelength or correspondingly from 300 GHz to 0.3 GHz in frequency. Soil roughness is well known to complicate the interpretation of microwave data (Choudhury et al., 1979, Newton and Rouse, 1980). In addition, the vegetation canopy attenuates (absorbs and scatters) the soil emission and adds its own contribution to the overall emission (Jackson et al., 1982). Of all the current techniques for soil moisture sensing, L-band (~1-2 GHz) passive microwave remote sensing has been most widely employed due to: 1) the direct relationship of its response in the form of brightness temperature (TB) and soil moisture through the soil dielectric constant; 2) its greater soil moisture retrieval depth and 3) reduced roughness and vegetation impact compared to higher frequencies; and 4) having a protected band (1.400-1.427 GHz) allocated exclusively for radio astronomy use, meaning that it should be clear of Radio Frequency Interference (RFI) (Wigneron et al., 2017).

To meet the growing need for global soil moisture data in hydrology, agriculture, drought, and flood forecasting, weather prediction, climate change, etc., the European Space Agency (ESA) launched the Soil Moisture and Ocean Salinity (SMOS) satellite (Kerr et al., 2010) in 2009 and the National Aeronautics and Space Administration (NASA) launched the Soil Moisture Active Passive (SMAP) satellite (Entekhabi et al., 2010) in 2015. Both use L-band (1.4 GHz/21-cm wavelength) radiometers to measure the microwave emission from the Earth in the form of TB, which is a function of the emissivity and physical temperature of the target. The emissivity of bare soil varies from approximately 0.5 for smooth and very wet soil to close to 1 for rough and very dry soil (Ulaby et al., 1982), being the primary link between soil moisture and TB. The advancement of satellite observations and retrieval algorithms has made global soil moisture maps available every three days or less with overall accuracy of 0.04 m^3/m^3.

1.2 Problem and Objective

Despite the above-mentioned achievements, global soil moisture sensing is still facing a few challenges. First, the moisture retrieval depth of the current L-band missions is believed to be 5 cm or even shallower (Escorihuela et al., 2010, Liu et al., 2012a, Zheng et al., 2019), which limits direct application of the data in disciplines that require deeper soil moisture information, e.g., weather prediction and climate research. Second, current SMAP and SMOS algorithms do not specifically consider any correction of the periodic row structure, which is a common type of soil tillage used for cultivation purposes and often affects soil emission to a substantial degree (Ulaby et al., 1986) because of the lack of global information on temporally varying row shape, height, and orientation. Third, the accuracy of these satellite products varies for different land surfaces. As an example, although the SMAP radiometer-based soil moisture data meets its overall target accuracy, errors for croplands are considerably larger (Chan et al., 2016, Colliander et al., 2017b, Walker et al., 2019).

P-band (0.3-1 GHz/100-30-cm wavelength) is a promising candidate for conquering some of the difficulties faced at L-band due to its longer wavelength. It is a widely held understanding that a longer waveband should have a deeper moisture retrieval depth and reduced impact from surface roughness and vegetation (Ulaby et al., 1986), resulting in a more useful contributing depth and an overall higher soil moisture retrieval accuracy over vegetated rough/periodic soil surfaces.

In terms of microwave radiometry, however, no observational evidence has been reported to demonstrate the postulated benefits of using P-band TB observations until this PhD research where the P-band Radiometer Inferred Soil Moisture (PRISM, see https://www.prism.monash.edu) tower project of Monash University was established. Taking advantage of the concurrently collected P- and L-band TB time series over a range of roughness and vegetation conditions, this PhD research aimed to demonstrate the potentially superior capability of a P-band radiometer over an L-band radiometer for soil moisture sensing from three aspects: 1) increased moisture retrieval depth, 2) reduced roughness impact, and 3) reduced vegetation impact. Global soil moisture

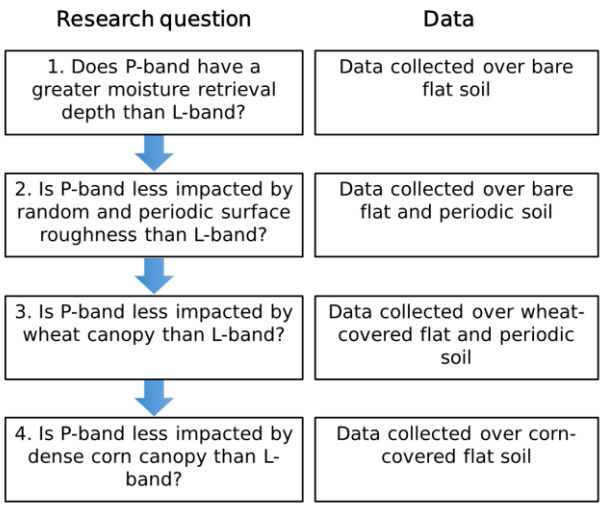

Figure 1-1: Diagram illustrating the four research questions with data used in this PhD research.

sensing could be substantially improved in terms of the moisture retrieval depth and retrieval accuracy if such hypotheses are proven to be true.

1.3 Outline of Approach

As Figure 1-1 presents, this thesis is organized around four key questions:

1. Does P-band have a greater moisture retrieval depth than L-band?

In this thesis, moisture retrieval depth was defined as the equivalent soil thickness for obtaining an average soil moisture that equates emissivity through the Fresnel equations to the theoretical emissivity from the coherent model. According to this definition, a moisture retrieval depth model was proposed to theoretically estimate the moisture retrieval depth for a range of typical soil profiles. To confirm this proposed method, empirical correlation analysis was also performed on the radiometric and soil moisture observations collected over bare flat soil.

2. Is P-band less impacted by random and periodic surface roughness than L-band?

The roughness effects herein involve two aspects: random roughness over flat soil and periodic roughness over furrowed soil for cultivation purposes. Accordingly, four different soil surfaces were included: flat soil, sinusoidal bench soil, and sinusoidal soil with a parallel and perpendicular orientation to the tower-looking direction. First, physical simulations were performed to seek theoretical evidence on the reduced roughness impact at P-band. Subsequently, the roughness model parameters were calibrated over the four soil surfaces. Finally, the parameters calibrated over the flat soil were applied to all four soil surfaces for soil moisture retrieval. The roughness impact of P- and L-band was compared based on the similarity of the retrieval performance across different soil surfaces.

3. Is P-band less impacted by wheat canopy than L-band?

This research question used the data for the same soil surfaces as in research question 2 but covered by a wheat canopy with no more than 4 kg/m^2 of vegetation water content (VWC). Based on the calibrated roughness parameter in research question 2, the vegetation parameters were further calibrated prior to the soil moisture retrieval. By comparing the retrieval performance across different soil surfaces, it was investigated whether the periodic surfaces need to be discriminated from the flat surfaces when covered by wheat in soil moisture retrieval at P- and L-band. Moreover, the vegetation impact at P- and L-band was compared by comparing the retrieval errors induced from ignoring the wheat canopy in the forward model.

4. Is P-band less impacted by a dense corn canopy than L-band?

This research question aimed to extend the investigation from the wheat with low-to-intermediate VWC in research question 3 to dense corn with an extremely high VWC of up to 20 kg/m^2. Similar to the methodology in research questions 2 and 3, roughness and vegetation parameters were calibrated separately and applied to soil moisture retrieval. The retrieval performance was subsequently compared at P- and L-band to demonstrate the expected reduction in vegetation impact at P-band.

1.4 Thesis Organization

This thesis consists of 9 chapters. Chapter 2 provides an extensive review of the literature pertaining to different aspects of radiometry for soil moisture retrieval. Chapter 3 describes the PRISM tower experiment and the data sets used in the following analysis chapters, including P- and L-band TB observations, station soil moisture and temperature measurements, roughness and vegetation sampling, etc. Chapter 4 elaborates on the physical and semi-empirical models briefly introduced in Chapter 2 that are subsequently used throughout this thesis.

Chapter 5 investigated research question 1 by theoretically and empirically estimating the moisture retrieval depth at P- and L-band. Chapter 6 answered part of research question 2 through physical simulation and soil moisture retrieval over different bare soil surfaces. Chapter 7 investigated part of research questions 2 and 3 over wheat-covered flat and periodic soil surfaces. Chapter 8 further addressed research question 4 by extending the investigation of vegetation to a higher-end VWC. Finally, Chapter 9 presents the conclusions of this thesis and discusses further research requirements in order to ensure a successful P-band mission.

2 Literature Review

This chapter presents the definition and importance of soil moisture and the techniques for soil moisture measurements. These techniques include 1) in-situ methods, and 2) remote sensing methods consisting of the visible, near- and thermal-infrared, and active and passive microwave techniques. Subsequently, passive microwave satellite missions are introduced, focusing on SMOS and SMAP, which is followed by the evolution of soil moisture measurement from microwave radiometry from the aspects of dielectric constant, sensing depth, effective temperature, soil surface roughness, and vegetation canopy. The soil moisture retrieval algorithms of current satellite missions are then reviewed. Finally, the knowledge gap and challenges at P-band are identified.

2.1 Definition and Importance of Soil Moisture

Soil moisture (or soil water content) is generally defined as the amount of water stored between the soil surface and water table, also known as the unsaturated zone. In practice, the water content is usually expressed in either the forms of volumetric or gravimetric soil moisture as follows (Seneviratne et al., 2010):

- volumetric soil moisture, $SM_v = \frac{v_w}{v_m}$ (m^3/m^3), where v_m and v_w are the volume of the moist soil and its water constituent, respectively; and
- gravimetric soil moisture, $SM_g = \frac{m_w}{m_m}$ (kg^3/kg^3), where m_m and m_w are the mass of the moist soil and its water constituent, respectively.

Other terms include the ratio of saturation, soil moisture index, and absolute water content (Seneviratne et al., 2010). This thesis uses volumetric soil moisture in absolute terms (m^3/m^3) unless otherwise specified.

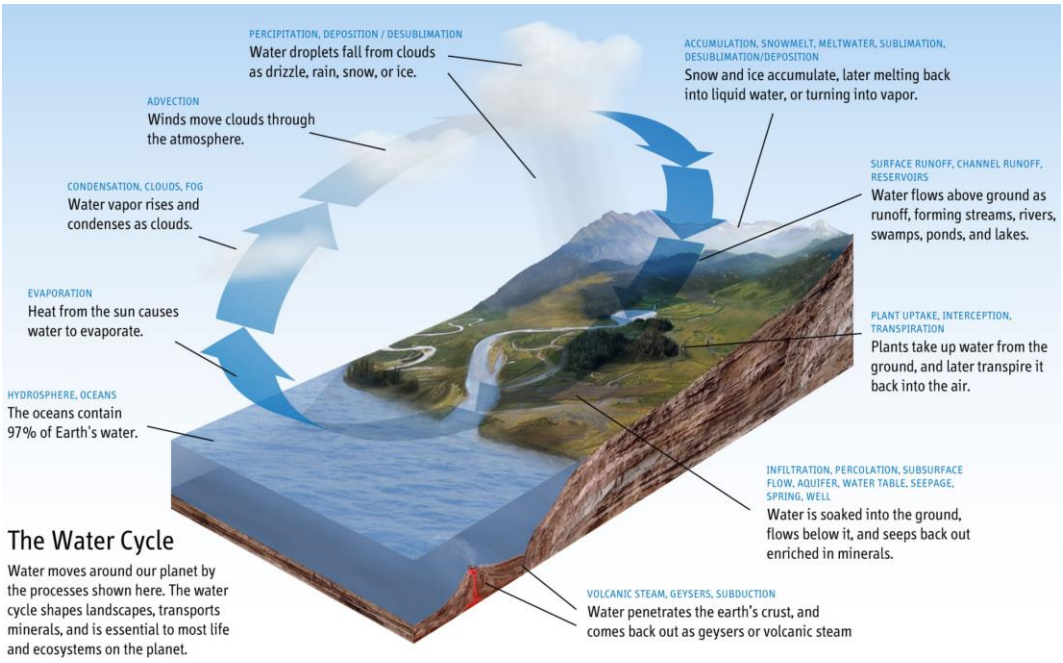

Figure 2-1: Hydrologic cycle between land, ocean, and atmosphere (Tal, 2016).

As a critical parameter in the hydrological cycle (Figure 2-1), soil moisture influences the precipitation partitioning into infiltration and runoff (Aubert et al., 2003). It also provides the water source for evapotranspiration, a process including mainly plant transpiration and bare soil evaporation that returns as much as 60% of the total land precipitation to the atmosphere (Oki and Kanae, 2006). Additionally, it partitions the land surface energy into latent and sensible heat fluxes through evapotranspiration (Trenberth et al., 2009, Seneviratne et al., 2010). Furthermore, soil moisture influences biogeochemical cycles since it is the ultimate solvent in the earth system.

Stocker et al. (2019) reported that neglecting soil moisture in photosynthesis estimation reduces global annual amounts by ~15%, increases interannual variability by more than 100% across 25% of the global vegetated land surface, and amplifies the impacts of extreme events on primary production. Moreover, soil moisture interacts with precipitation, temperature, ecosystems, and climate systems (Seneviratne et al., 2010). With increased climate change awareness, the measurement and analysis of soil moisture impacts at global scale remain an outstanding scientific problem with far-

reaching significance to humankind (Wei, 1995). Consequently, the Global Climate Observing System identified soil moisture as an Essential Climate Variable (Mason et al., 2010) to support the United Nations Framework Convention on Climate Change and the Intergovernmental Panel on Climate Change (Dorigo et al., 2015).

Soil moisture data have been widely used in fields such as global climate variability and change (Dorigo et al., 2017b), global carbon cycle (Scholze et al., 2016), weather prediction (Scipal et al., 2008, Hunt and Turner, 2017), flood forecasting (Parinussa et al., 2016, Chifflard et al., 2018), landslide forecasting (Brocca et al., 2012) and assessment (Zhao et al., 2021a), and drought detection (Cáceres et al., 2015, Yuan et al., 2015, Xu et al., 2020). In addition, accurate soil moisture status is critical to agriculture, specifically yield prediction (Zhang, 2020), water conservation (Bayer et al., 2013, Volo et al., 2014), and agriculture management (Schulte et al., 2012, Stevens et al., 2016). It is also worth noting that public health is also associated with soil moisture through links to vector-borne diseases (Shaman and Day, 2005).

2.2 Techniques for Soil Moisture Measurement

Measuring soil moisture is challenging because of the high variability across temporal and spatial scale (Owe et al., 2008). In-situ measurements can only be performed at limited locations and thereby cannot meet the requirement of hydrological studies that usually cover a basin of thousands of square kilometers. In recent decades, the advancement of remote sensing techniques has drawn the community's attention due to its capability of providing (near-) real-time soil moisture information at national or even global scale. However, remotely sensed soil moisture data still have some shortcomings. While the mismatch of the point-scale in-situ measurements and the footprint-scale remote sensing observations is challenging (Crow et al., 2012), the in-situ observations are regarded as the "ground truth" to assess the quality and accuracy of the remotely sensed estimates.

Parallel with the development of remote sensing techniques, in-situ measurement networks have been established worldwide for validating the remotely sensed soil

moisture data, i.e., the Global Soil Moisture Data Bank (GSMDB, Robock et al., 2000) and the International Soil Moisture Network (ISMN, Dorigo et al., 2011). In addition, the Quality Assurance for Soil Moisture (QA4SM, https://qa4sm.eodc.eu/) service has been established to provide a user-friendly interface for evaluating remotely sensed soil moisture data against the ISMN and land surface models. It has facilitated and standardized the validation of satellite soil moisture data by bringing together methodologies and protocols and providing users with traceable validation results.

2.2.1 *In-situ* techniques

The gravimetric method also called the thermostat-weight or thermogravimetric method, is the most direct technique and is thus taken as the benchmark for calibrating and validating other indirect measurements. This method physically extracts soil samples from the field, weighs the sample before and after drying in an oven for at least 24 hours at 105°C, and converts the mass difference to gravimetric soil moisture (Montzka et al., 2020). Afterward, the gravimetric soil moisture can be converted to volumetric soil moisture using the soil density, facilitated by collecting a known volume of soil. Regular gravimetric soil moisture measurements were started in the 1930s in the former Soviet Union through an agrometeorological station network (Robock et al., 2000). Nevertheless, this method is impractical for long-term monitoring since it is labor-intensive and destructive to its site.

Other methods are indirect and include measuring a proxy variable and relating it to the gravimetric soil moisture through physical or empirical relationships called calibration curves. These methods consist of the tensiometric method (Schmugge et al., 1980), Time-Domain Reflectometry (Davis and Chudobiak, 1975), Transmission Line Oscillators (Campbell and Anderson, 1998), Time Domain Transmissometry (Blonquist Jr et al., 2005), impedance sensors (Gaskin and Miller, 1996), heat pulse sensors (Campbell et al., 1991, Reece, 1996), and capacitance sensors (Nadler and Lapid, 1996). After proper installation, all these techniques can operate automatically for continuous point-scale observation at various depths. Please see Yu et al. (2021) for a detailed overview.

To bridge the scale gap between in-situ measurements and satellite remote sensing observations, some novel non-invasive techniques have emerged, allowing for continuous contactless and integrative soil moisture sampling at field- to basin-scale (Bogena et al., 2015).

- Cosmic-ray neutron probes (CRNP) count secondary fast neutrons beside the soil surface, created by primary cosmic-ray particles in the atmosphere and soil (Zreda et al., 2008, Zreda et al., 2012). These secondary fast neutrons collide with the hydrogen atoms in soil water. Consequently, CRNP will detect more neutrons in dry than wet soil.
- Global Navigation Satellite System (GNSS), initially used for positioning and navigation, has recently been applied to soil moisture retrieval (Larson et al., 2008a, Larson et al., 2008b). Ground-based GNSS antennas simultaneously receive the direct signal from the GNSS satellites and the signal reflected by the land surface. The two signals cause an interference pattern whose amplitude and phase are influenced by the soil moisture.
- Gamma-ray intensity can be measured and negatively correlated to soil moisture (Yoshioka, 1989) because all rocks and soil have radioactive isotopes whose decay emits gamma radiation. This radiation is more significantly attenuated by water than by air or soil particles.
- Ground penetrating radar (GPR) transmits electromagnetic waves and records the reflected signal. The reflection/transmission ratio is related to soil moisture. GPR can penetrate the soil down to ~2 m with an ~10-cm vertical resolution when operating at ~500 MHz (Koyama et al., 2017).

2.2.2 Remote sensing techniques

Remote sensing techniques measure the emitted and/or reflected and/or scattered EM radiation from the land surface to estimate soil moisture, categorized into several groups according to the wavelength (or frequency) in the EM spectrum (Figure 2-2). Over the past five decades, researchers have conducted extensive ground-, air- and space-based soil moisture remote sensing studies using visible, near- and thermal-

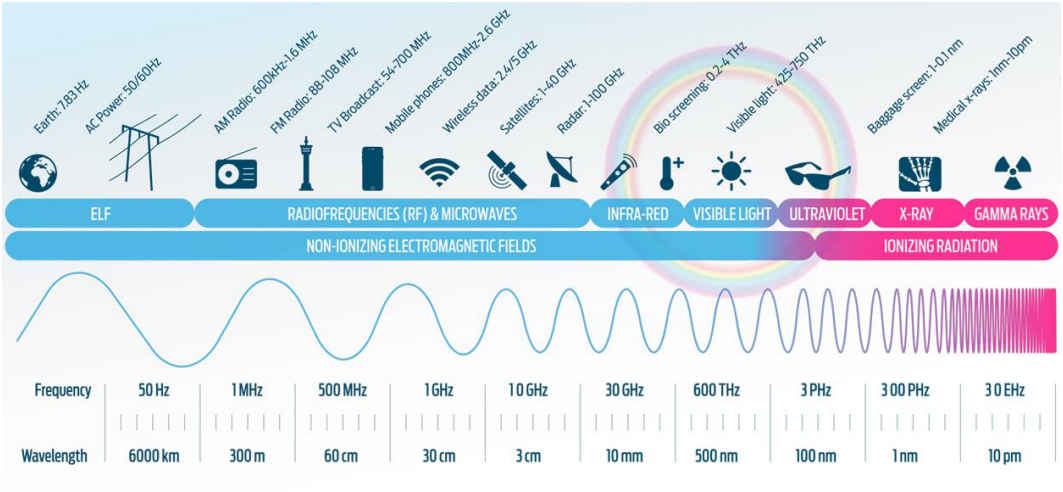

Figure 2-2: The electromagnetic spectrum (TelenorGroup).

infrared, as well as active and passive microwave techniques (Petropoulos et al., 2015). An overview of these techniques is provided in Table 2-1.

While visible and infrared data have a high spatial resolution, they cannot be applied to global soil moisture estimation due to the attenuation from clouds, vegetation and atmosphere, the requirement of solar illumination, and its limited moisture sensing depth. In recent decades, microwave remote sensing has proven to be the most promising approach for (near-) real-time global soil moisture estimation due to its advantages explained in Table 2-1.

Apart from the techniques listed in Table 2-1, gravity missions such as the Gravity Recovery and Climate Experiment (GRACE, Rodell et al., 2009) also exhibit potential in global soil moisture sensing (Abelen and Seitz, 2013). However, they cannot differentiate soil moisture from other water sources like snow, surface water and groundwater. In the following, visible, near- and thermal-infrared, as well as active and passive microwave techniques for soil moisture sensing are reviewed.

- Visible, near-infrared and thermal-infrared

Visible and near-infrared approaches generally link soil moisture to the reflectance via the water absorption bands. The negative correlation between reflectance and soil

Table 2-1: Prime remote sensing techniques for near-surface soil moisture estimation, adapted from Petropoulos et al. (2015) and Wang and Qu (2009).

Technique	Observed variable	Advantage	Disadvantage
Visible/near-infrared	Land surface reflectance	High spatial resolution, numerous satellites, hyperspectral sensors	Cloud attenuation, atmosphere attenuation, vegetation attenuation, unavailability at night, severely limited sensing depth
Thermal-infrared	Surface temperature	High spatial resolution, numerous satellites	Cloud attenuation, atmosphere attenuation, vegetation attenuation, unavailability at night, limited sensing depth
Active microwave (radar)	Backscattering coefficient	Fine spatial resolution, all-time/weather capability, moderate penetration through vegetation, moderate sensing depth, negligible atmosphere attenuation < 10 GHz	Coarse temporal resolution, sensitivity to vegetation geometry and structure, high sensitivity to surface roughness
Passive microwave (radiometer)	Brightness temperature	High temporal resolution, all-time/weather capability, moderate penetration through vegetation, moderate sensing depth, negligible atmosphere attenuation < 10 GHz	Coarse spatial resolution, vulnerable to RFI

moisture was first discovered by Ångström (1925). In the 1970s, optical remote sensing was investigated for soil moisture estimation by Johannsen (1970). Subsequently, Jackson et al. (1976) experimentally demonstrated that dry soil had a two-times-higher

albedo than wet soil. Since then, empirical relationships have been widely built to estimate surface soil moisture.

Liu et al. (2002) reported that, as the soil moisture increased, the soil reflectance decreased when the soil moisture was lower than the critical point but increased when the soil moisture was higher than the critical point. This so-called critical point is associated closely with the soil hydrodynamic characteristics. Through measuring the soil reflected shortwave radiation (400-2500 nm) in various moisture conditions, Lobell and Asner (2002) proposed a physical model and discovered an exponential relationship between soil reflectance and soil moisture. They also highlighted that the longer waveband (e.g., shortwave-infrared) is more suitable for estimating high soil moisture because reflectance quickly saturates at visible and near-infrared bands.

For vegetated soil surfaces, the well-known Normalized Difference Water Index (NDWI) was widely used to estimate surface soil moisture by exploiting near- and shortwave-infrared bands (Gao, 1996). Later, Ghulam et al. (2007) proposed a Modified Perpendicular Drought Index as an indicator of soil moisture by utilizing the sensitivity of vegetation to soil water variations. More recently, Gao et al. (2013) established an empirical relationship between vegetation canopy and the mixed pixel reflectance at red to near-infrared bands to calculate soil moisture.

In terms of thermal-infrared methods, thermal inertia, defined as the resistance to ambient temperature variations, highly correlates with soil moisture and can be used to quantitatively determine soil moisture (Jaeger, 1953, Pohn et al., 1974). Overall, promising results have been reported over bare (Leng et al., 2016, Matsushima et al., 2018) and sparsely vegetated soil (Maltese et al., 2013a, Maltese et al., 2013b).

A primary limitation of these techniques is the substantial deviation when employed outside local calibration conditions since soil spectral characteristics mutually depend on soil moisture, roughness, texture (i.e., clay, sand, and silt fractions), organic carbon, and observation geometry (Moran et al., 2004, Soriano-Disla et al., 2014). Despite the high spatial resolution, the relatively short wavelength means that these techniques can

only sense the very top layer of soil, which is a severe limitation of utilizing these data in hydrological and agricultural applications. Moreover, natural soil is rarely bare, and therefore what can be sensed from these techniques is usually properties of the vegetation rather than the soil beneath, let alone that atmosphere and cloud can further degrade the sensing capability of these methods (Griend et al., 1985, Zhao and Li, 2013).

- Active microwave

Microwave remote sensing is categorized into active and passive techniques according to the source of the EM radiation. Active microwave remote sensing instruments, i.e., radar, scatterometer, and altimeter, generate and transmit microwave energy towards the target and measure the reflected signal. Synthetic aperture radar (SAR) is the most commonly used radar system for soil moisture retrieval. It utilizes signal processing techniques and the movement of the platform to simulate a large antenna or aperture, resulting in a high spatial resolution.

A range of airborne SAR experiments have been carried out and have expanded the knowledge of soil moisture retrieval in the past few decades (see Karthikeyan et al. (2017a) and Liu et al. (2019) for comprehensive reviews). Among these, P-band SAR has been paid much more attention than those at higher frequencies due to the expected larger penetration through vegetation and soil, i.e., Jet Propulsion Laboratory (JPL) AIRborne SAR (AIRSAR, Freeman et al., 1990), German Aerospace Center E-SAR (Horn, 1996) and F-SAR (Horn et al., 2009), and French Aerospace Research Agency Radar Aéroporté Multi-spectral d'Etude des Signatures (RAMSES, Dubois-Fernandez et al., 2002).

More recently, a P-band SAR known as the Airborne Microwave Observatory of Subcanopy and Subsurface (AirMOSS), was selected as one of five NASA Earth Venture-1 investigations in May 2010 (Chapin et al., 2012). It sought to retrieve the root-zone soil moisture and moisture profiles over America (Tabatabaeenejad et al., 2014, Crow et al., 2018, Etminan et al., 2020, Tabatabaeenejad et al., 2020, Tobin et al.,

2021). Alemohammad et al. (2019) concurrently collected P- and L-band backscattering observations using AirMOSS and the NASA/JPL's Uninhabited Aerial Vehicle SAR (UAVSAR), respectively, and demonstrated reduced vegetation scattering at P-band. In addition, P-band satellite signals of opportunity has been proven to have a potential for sensing subsurface soil moisture (Yueh et al., 2020). These findings have motivated the first-ever spaceborne P-band-radar mission for mapping global forest biomass, i.e., Biomass (Le Toan et al., 2011) scheduled for launch in 2023, and the SigNals of Opportunity: P-band Investigation (SNoOPI) for soil moisture mapping scheduled for launch in early 2022 (Garrison et al., 2021).

So far, more than ten satellite SAR missions have been operating, and quite a few missions have been projected to launch in the next five years. All these SAR missions work at below 10 GHz, and most of them have a fine spatial resolution ranging from 1 to 100 m. Currently, the Advanced Land Observing Satellite 2 (ALOS-2, Kankaku et al., 2014) and Satélite Argentino de Observación COn Microondas-1A/B (SAOCOM-1A/B, Giraldez, 2003) are the only two operating L-band SAR missions. Despite the high spatial resolution of these SAR missions, only Sentinel-1 (Torres et al., 2012), SAOCOM-1A/B, and ALOS-2 provide regular global observations at revisits of 6-12, 8-16, and 14-46 days, respectively, being far from the 2- to 3-day requirement (Walker and Houser, 2004). Please refer to Liu et al. (2019) and Zhu (2019) for a detailed overview of current and scheduled SAR missions.

The observed variable of active microwave instruments is the backscattering coefficient, calculated as the ratio of the transmitted and reflected intensity and generally expressed in decibels (dB). It is dependent on observing wavelength/frequency, mono- or bi-static configurations, local incidence and scattering angles, peak power transmit, transmit/receive polarizations, and finally, soil properties, i.e., soil moisture and texture, etc. (Ulaby et al., 2014).

In practice, surface roughness and vegetation canopy make σ^0 less sensitive to soil moisture, with sensitivity from vegetation of 10 dB, surface roughness of 7 dB, to soil moisture of 4 dB (Kim et al., 2011, McNairn et al., 2014). As a result, accurately

characterizing roughness and vegetation impact is necessary for deriving precise soil moisture information using active microwave observations.

Surface roughness amplifies scattering and reduces the reflection in the specular direction, i.e., σ^0. Numerous scattering models have been developed to account for the soil roughness over bare soil, such that 1) the semi-empirical Dubios model (Dubois et al., 1995) and the Oh model (Oh et al., 1992); 2) the physical Integral Equation Model (IEM, Fung et al., 1992, Fung, 1994) and its descendants, i.e., the Improved IEM (IIEM or I2EM, Fung et al., 2002) and the Advanced IEM (AIEM, Chen et al., 2003); and 3) the Numerical Maxwell Model in 3-D Simulations (NMM3D, Huang et al., 2010, Huang and Tsang, 2012). Panciera et al. (2014) compared the IEM, Oh, and Dubois models over Australia using airborne L-band SAR data and found that their accuracy is comparable under HH polarization, whereas the Oh model is superior at VV polarization.

The vegetation impact has also been integrated into scattering models. The Water Cloud Model (Attema and Ulaby, 1978) is one of the most important and commonly used semi-physical models for retrieving the soil moisture under a vegetation canopy. It assumes the vegetation behaving as a homogeneous water cloud distributed above the soil. Other models are either based on the radiative transfer theory (e.g., Ulaby et al., 1990, Stiles and Sarabandi, 2000) or the distorted Born approximation (e.g., Lang and Sighu, 1983, Burgin et al., 2011).

Although abundant models have been established for soil moisture retrieval, an ill-posed retrieval issue has been raised, given that the number of the model parameters needed to be determined is usually larger than that of observations (Zhu et al., 2019b). The scientific community has seen a great opportunity of taking advantage of multiple SAR missions to address this issue and improve the temporal resolution of SAR data (Srivastava et al., 2006, Balenzano et al., 2010, Zhu et al., 2019a, Zhu et al., 2019c). Moreover, the concepts and methodologies from machine learning have been introduced to deal with the SAR soil moisture retrieval, often with an improved

performance compared to traditional methods (Ahmad et al., 2010, Ali et al., 2015, Liu et al., 2020, Zhu et al., 2020, Chen et al., 2021, Manninen et al., 2021).

- Passive microwave

Unlike radar, a passive microwave instrument, i.e., radiometer, does not generate any radiation of its own but rather measures the emitted energy from the target in the form of brightness temperature, which is a function of emissivity and physical temperature of the target. The emissivity of bare soil generally varies from 0.5 to close to 1 in different moisture and roughness conditions (Figure 2-3), corresponding to an approximately 150-K difference in TB if the soil temperature is assumed to be 300 K. This variation is much larger than the noise sensitivity threshold of radiometers (typically ~1 K), resulting in a large signal-to-noise ratio and thus an expected accuracy better than 0.01-0.02 m^3/m^3 (Njoku and Entekhabi, 1996). However, this accuracy is not practically achievable due to modeling uncertainties resulting from soil properties, soil heterogeneity, surface roughness, and vegetation, which will be discussed in Chapters 2.3 and 2.4.

Extensive ground- and air-based experiments since the late 1960s have significantly promoted passive microwave remote sensing in near-surface soil moisture retrieval. As

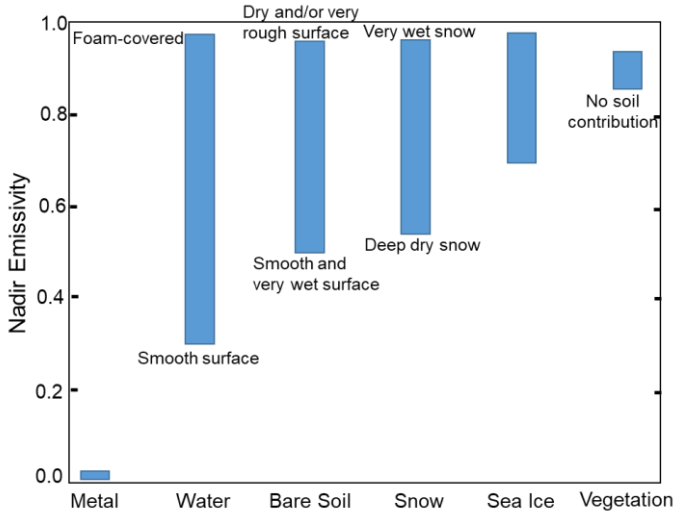

Figure 2-3: Range of values that microwave nadir emissivity may cover for various targets, adapted from Ulaby et al. (1982).

one of the earliest studies in passive microwave soil moisture sensing, Conel (1970) conducted a so-called plate experiment, with radiometers observing the response from plane layers of granulated silicate materials backed by a perfectly reflecting metal plate. He discovered that TB is highly dependent on soil moisture and that a longer waveband has a larger attenuation depth. Shortly after, airborne radiometric observations were collected by Blanchard (1972) over the Washita River basin to explore the soil moisture sensing capability of passive microwave instruments.

In 1978 and 1979 JPL undertook two pioneering field experiments to figure out whether P-(0.775 and 0.85 GHz), L-(1.42 GHz), or X-(10.69 GHz) band was the most effective in soil moisture sensing (Njoku and O'Neill, 1982). P- and L-band observations were found to be more sensitive to soil moisture variations than those at X-band. However, issues of moisture retrieval depth, roughness effects, and vegetation effects were not investigated in depth in this research.

Since the 1990s, passive microwave experiments have grown, including the Hydrologic Atmospheric Pilot Experiment (Nichols et al., 1993), the First International Satellite Land Surface Climatology Project Field Experiment (Wang et al., 1990), the PORTOS experiments (Wigneron et al., 1993a, Wigneron et al., 1993b, Wigneron et al., 1995), the Monsoon field experiments (Jackson et al., 1993, Kustas and Goodrich, 1994), the Washita experiments (Jackson et al., 1995, Shi et al., 1997, Wang et al., 1997), the Soil Moisture Experiment (Narayan et al., 2004, Bindlish et al., 2006), the Surface Monitoring of the Soil Reservoir Experiment (Rosnay et al., 2006), the National Airborne Field Experiments (Merlin et al., 2008, Panciera et al., 2008), the Watershed Allied Telemetry Experiment Research (Li et al., 2009), the Australian Airborne Calibration/validation Experiments for SMOS (Peischl et al., 2012a), the Soil Moisture Active and Passive Experiments 1-5 (Panciera et al., 2013, Ye et al., 2019, Ye et al., 2020a), the Heihe Watershed Allied Telemetry Experiment Research (Li et al., 2013), the SMAP validation experiment (McNairn et al., 2014, Colliander et al., 2017a), the Soil Moisture Experiment in the Luan River (Zhao et al., 2020b), etc. Moreover, several experiments have also been conducted in cold regions where frozen soil needs to be

considered, e.g., the Tibetan Plateau (Zheng et al., 2019, Zheng et al., 2021). Please refer to Wigneron et al. (2007) and Zhao et al. (2020b) for comprehensive reviews of these experiments and more.

- Synergistic active and passive microwave remote sensing

While both active and passive microwave instruments have the potential for soil moisture estimation, they have different sensitivities to different surface properties. Specifically, radars are more sensitive to surface roughness as well as vegetation biomass and structure, whereas radiometers are more sensitive to near-surface soil moisture (Njoku et al., 2000, Lee and Anagnostou, 2004). Overall, many operating SAR missions have routinely achieved a 0.06-m^3/m^3 unbiased root-mean-square error (ubRMSE) (Montzka et al., 2020), which has not yet attained the accuracy achieved by the passive microwave approach, i.e., a 0.04 m^3/m^3 ubRMSE (Colliander et al., 2017b).

Even though radars generally require larger antennas and more energy to work properly (Woodhouse, 2005), which is a significant disadvantage in terms of payloads onboard satellites, they have much finer spatial resolution than radiometers. Compared to radars, radiometers have a coarser spatial resolution but a wider swath and provide more frequent coverage, making them more suitable for observing (near-) real-time global soil moisture (Entekhabi et al., 2010).

The synergy of active and passive microwave remote sensing can benefit soil moisture estimation. Lee and Anagnostou (2004) combined the passive and active microwave observations from the Tropical Rainfall Measuring Mission (TRMM) to estimate soil moisture and vegetation properties. They found this synergy could increase the number of estimated geophysical variables, particularly over areas covered by low to moderate vegetation. Importantly, SMAP was designed to take advantage of the strengths of an L-band SAR and an L-band radiometer for enhanced soil moisture mapping (Entekhabi et al., 2010). It aimed to provide soil moisture data with higher accuracy and spatial resolution than those from using either of the individual instruments alone (Das et al., 2018). More recently, Gao (2016) incorporated the

active-retrieved roughness parameters into the passive microwave model to improve retrieval accuracy, making model calibration procedure unnecessary. Moreover, a discrete radiative transfer model, i.e., the Tor Vergata model (Bracaglia et al., 1995, Ferrazzoli and Guerriero, 1995, Ferrazzoli and Guerriero, 1996), driven by a single set of input parameters, has been applied to simulate and relate both emissivity and backscattering coefficient (Dente et al., 2014, Guerriero et al., 2016, Zheng et al., 2021).

Another challenge has been that individual satellites cannot provide soil moisture records that span the long periods (e.g., >30 years) required in climate research. To bridge this gap, the ESA Climate Change Initiative (CCI) soil moisture product was developed by harmonizing and merging multiple Level 2 soil moisture products from different active and passive microwave sensors (Liu et al., 2011, Liu et al., 2012b, Wagner et al., 2012, Dorigo et al., 2017a). This product presents global surface soil moisture from 1978 to 2020 with a spatial resolution of 0.25°, a temporal resolution of 1 day, and moisture sensing depth from 0.5 to 5 cm (Mittelbach et al., 2014). Extensive worldwide evaluations have demonstrated its satisfactory performance (Dorigo et al., 2015, Zeng et al., 2015, An et al., 2016, Shen et al., 2016, Dorigo et al., 2017a).

2.2.3 Passive microwave satellite missions

Given the discussion above, passive microwave is considered to be superior for rapidly providing global soil moisture datasets with reliable accuracy, which is the focus of this thesis. A number of satellite missions carrying passive microwave instruments have been launched and operated in the last four decades, including the Nimbus 7 satellite, the Defense Meteorological Satellite Program (DMSP), TRMM, the Aqua satellite, the Coriolis satellite, the FengYun-3B satellite, the Aquarius mission, the Global Change Observation Mission-Water "SHIZUKU" (GCOM-W), SMOS and SMAP. Please see Karthikeyan et al. (2017b) and Montzka et al. (2020) for a complete review of these missions.

Currently, SMOS and SMAP are the only two L-band missions dedicated to global soil moisture monitoring. SMOS was launched successfully on November 2, 2009 by ESA (Kerr et al., 2010). It is based on a sun-synchronous orbit (overpasses at 6 am/6 pm local time). The only payload is the Microwave Imaging Radiometer with Aperture Synthesis, a passive microwave 2-D interferometric radiometer operating at 1.413 GHz/ 21 cm. SMOS provides TB at different incidence angles (0 to 55º) and full polarizations. The mission objective was to provide (ESA, 2017): 1) global volumetric soil moisture observations having an accuracy of 0.04 m^3/m^3, a spatial resolution of 35-50 km^2 and a temporal resolution of 1-3 days; 2) global ocean salinity observations with an accuracy of 0.1 practical salinity scale units for a 10-30 day average at a spatial resolution of 200 km^2; and 3) daily sea ice thickness observations for the northern hemisphere at a spatial resolution of a 10 km^2 up to maximum values of 50 cm.

SMAP was launched on January 31, 2015 by NASA, having a SAR and a radiometer both at 1.41 GHz (Entekhabi et al., 2010). It operates in a near-polar and sun-synchronous Earth orbit (overpasses at 6 am/6 pm local time) with a constant incidence angle at around 40°. The SAR and the radiometer share a 6-m-aperture reflector antenna that conically scans a swath of 1000 km in width, with spatial resolutions of 3 km and 40 km, respectively. SMAP's scientific objectives were 1) to collect a global surface (top ~5 cm) soil moisture dataset with an ubRMSE of no greater than 0.04 m^3/m^3 at a 9-km spatial resolution and a 3-day temporal resolution; and 2) to capture freeze/thaw state transitions in the integrated vegetation-soil continuum with a 3-km spatial resolution and a 2-day revisit (Entekhabi et al., 2014). Unfortunately, the SAR ceased operations abruptly 11 weeks after launch on July 7, 2015, with the radiometer remaining operating till now. As a substitute, the Sentinel-1 C-band SAR has been employed to produce the active-passive high-resolution surface soil moisture product (Das et al., 2016, He et al., 2018, Das et al., 2019).

Evaluations of the SMOS and SMAP soil moisture products have been conducted worldwide. Jackson et al. (2011) reported that the SMOS soil moisture retrievals approached the anticipated performance (0.04 m^3/m^3) with an overall RMSE of 0.043

m^3/m^3. However, Al Bitar et al. (2012) found that SMOS met the required accuracy only over some specific nominal cases, with overall underestimated soil moisture compared to in-situ measurements. More recently, Kerr et al. (2016) consider that SMOS has performed satisfactorily with globally consistent results over different eco climate regions. They also noted that their neural network-based product known as SMOS Neural Network Soil Moisture Data Assimilation, often performed well in areas where other products are poor.

As for SMAP's performance, Chan et al. (2016) and Colliander et al. (2017b) agreed that SMAP meets its overall target accuracy of 0.04 m^3/m^3 in ubRMSE, yet with considerable variations across different validation sites. Al-Yaari et al. (2017) noted a better accuracy of the SMAP product over the SMOS product. Recently, Beck et al. (2021) used in-situ measurements from 826 sensors in the USA and Europe to evaluate 18 satellite- and model-based soil moisture datasets. SMAP performed best with a 0.65 correlation coefficient (R) among the six satellite-based products, while SMOS performed worst with an R of 0.47.

Some projected passive microwave satellite missions include the Copernicus Imaging Microwave Radiometer (CIMR) mission (Kilic et al., 2018) within the European Copernicus Expansion program, the Water Cycle Observation Mission (WCOM, Shi et al., 2014) and the Terrestrial Water Resources Satellite (TWRS, Zhao et al., 2020b) by China National Space Administration, and the SMOS-High Resolution (SMOS-HR) mission (Rodríguez-Fernández et al., 2019) by Centre National d'Etudes Spatiales.

2.3 Microwave Radiometry of Soil

Soil moisture retrieval consists of two phases: relating soil moisture to TB using the forward model and inverting the forward model of soil moisture by constraining some conditions.

The models predicting soil microwave radiation can be categorized as coherent and noncoherent in terms of how they treated soil radiation. Stogryn (1970) developed a

coherent radiative transfer formulation, which was later extended by Tsang and Kong (1975). Subsequently, Njoku and Kong (1977) applied it to simulate soil microwave emission. Wilheit (1978) followed by developing a similar model but with fewer computations.

Noncoherent radiative transfer models are usually approximated as zero- and higher-order models. In the first-order noncoherent model developed by Burke et al. (1979), the soil is horizontally stratified into N layers. The radiation emitted from the soil surface is the summation of the contributions from each layer, considering the absorption in all layers above an emitting layer and the reflection losses at all boundaries between all layers above the emitting layer, but ignoring second- and higher-order reflections.

Compared to the models mentioned above, the zero-order noncoherent radiative transfer model proposed by Schmugge and Choudhury (1981) is computationally simpler and has been the most widely used model in soil moisture retrieval. It approximates the Burke model by ignoring all reflections within the soil medium but considering the reflection only at the air-soil interface.

In principle, TB is a function of the observing configuration, i.e., incidence angle θ, frequency f or wavelength λ and polarization P (H-pol and V-pol), as well as the physical properties of the target, i.e., relative dielectric constant ε_r, physical temperature T, reflectivity Γ, and emissivity e. In the following sub-sections, a couple of primary factors that directly or indirectly affect TB are discussed.

2.3.1 Dielectric constant

The basic principle of using microwave techniques to estimate soil moisture is that soil water significantly determines soil dielectric constant (e.g., ~3.5 for very dry soil and ~40 for saturated soil) (Ulaby et al., 1986) due to the high dielectric constant of water (~80) (Wagner et al., 2011). A high dielectric constant leads to low emissivity and thus a low/cold TB for a given physical temperature. The dielectric constant is usually

expressed as a relative form which is the ratio of the dielectric constant of a given kind of material to that of free space, such that $\varepsilon_r = \varepsilon_r' - j\varepsilon_r''$ including real ($'$) and imaginary ($''$) parts. The real part determines the propagation characteristics of the energy as it passes upward through the soil, and the imaginary part characterizes the energy loss in the propagation.

A range of soil dielectric mixing models have been developed in the past years. Wang and Schmugge (1980) developed a simple empirical model at 1.4 and 5 GHz, with inputs of soil moisture plus clay and sand fractions. Subsequently, Hallikainen et al. (1985) introduced an empirical model over a broader frequency range between 1-18 GHz. Because of the failure of the Wang and Schmugge (1980) model in accurately predicting ε_r'' and conductivity losses, Dobson et al. (1985) proposed a semi-empirical model applicable between 1.4 and 18 GHz utilizing inputs of soil moisture, temperature, clay and sand fractions, bulk density, and the observation frequency. Later, this model was extended to P-band including from 0.3 to 1.4 GHz (Peplinski et al., 1995a, Peplinski et al., 1995b).

Based upon the Debye dielectric relaxation formula (Dobson et al., 1985), Mironov et al. (2004) proposed a model considering the different effects of bound and free soil water. It extended the Refractive Mixing Dielectric Model (Birchak et al., 1974) to enable a prediction of dielectric constants as a function of soil moisture and observation frequency. Afterward, Mironov et al. (2009) simplified the spectroscopic parameters of the original model (Mironov et al., 2004) into soil moisture, observation frequency, and clay fraction, making it a generic model with more convenience in practical applications. Later, they further upgraded this model by accounting for the interfacial (Maxwell-Wagner) relaxation of soil water (Mironov et al., 2013b, Mironov et al., 2014), which is significant at P-band (Chen and Or, 2006). Importantly, significant advances in models applicable to thawed and frozen soil have been achieved (Zhang et al., 2010, Mironov and Savin, 2015, Mironov et al., 2017a, Mironov et al., 2017b, Zheng et al., 2020).

Dielectric models are considered a significant uncertainty source in forward modeling of TB because of their empirical parameters. A comprehensive evaluation of nine commonly used dielectric models by Park et al. (2019) presented an average bias of around 0.03 m^3/m^3 compared to laboratory dielectric measurements. Mialon et al. (2015) compared the Dobson and Mironov model and found the retrieved soil moisture from the latter was higher at global scale, however, with no evidence to show either one was better. Moreover, a number of local-scale studies demonstrated a better performance of the Mironov model over the Dobson model (Wigneron et al., 2011, Montpetit et al., 2015, Srivastava et al., 2015), especially for very sandy soil (Bircher et al., 2012, Bircher et al., 2016) and organic-rich soil in the northern cold climate zone (Bircher et al., 2015).

2.3.2 Sensing depth

Sensing depth is an essential concept in microwave remote sensing, indicating the soil depth for which the measured microwave signal is representative. Various terminology has been used concerning microwave sensing depth, including penetration depth (Conel, 1970), temperature sampling depth (Wilheit, 1978), and moisture sensing depth (Njoku et al., 1980). The various terminology is somewhat confusing and thus needs clarification. Generally, the terminology can be categorized into two main classes: one from the aspect of thermal (radiation) and the other from the aspect of reflectivity (dielectric). These are introduced below.

The penetration depth was originally defined as the length over which the energy density associated with an advancing plane wave is reduced to 1/e of its initial value (Born and Wolf, 1964). In the early 1970s, penetration depth was estimated by plate experiments (Conel, 1970, Blinn and Quade, 1972). However, the term is somewhat ambiguous because "penetration" implies the wave is penetrating the soil, being the case for radar rather than radiometry.

Later, Wilheit (1978) and Njoku et al. (1980) proposed thermal sampling depth and temperature sensing depth, respectively, which have been used synonymously. The

definition in Njoku et al. (1980) is more specific, with temperature sensing depth expressed as the depth from above which (1 - 1/e) ≈ 63% of the emitted radiation originates. The temperature sensing depth can be expressed as (Ulaby et al., 1986)

$$\delta_t = \lambda/[4\pi|\mathrm{Im}(\sqrt{\varepsilon_r})|], \quad \text{Eq. 2-1}$$

where Im[ ] represents the imaginary part. Eq. 2-1 indicates that the temperature sensing depth increases as wavelength increases, being approximately 10 cm at L-band and 20 cm at P-band for a 0.3-m^3/m^3 moisture condition (Njoku and Entekhabi, 1996). Recently, Lv et al. (2019) redefined the temperature sensing depth as the depth whereby soil temperature equals the effective soil temperature.

In practice, the moisture sensing (sampling or observation) depth is of primary interest because it indicates the soil thickness whose moisture content can theoretically be retrieved. Njoku et al. (1980) defined it as the depth below the surface over which moisture (i.e., dielectric constant) determines the surface reflectivity and emissivity. Accordingly, a common approach for estimating the moisture sensing depth has been to empirically correlate the observed brightness temperature observations with soil moisture measurements averaged over different soil thicknesses (Wang and Choudhury, 1981, Paloscia et al., 1993, Escorihuela et al., 2010, Zheng et al., 2019). The moisture sensing depth was found to be much less than the thermal sensing depth, being no deeper than 5 cm at L-band (Escorihuela et al., 2010, Liu et al., 2012a, Zheng et al., 2019).

2.3.3 Effective soil temperature

The commonly used zero-order noncoherent radiative transfer model usually assumes an ideal soil medium with constant soil moisture and temperature with depth (Schmugge and Choudhury, 1981). However, natural soil is by no means uniform because soil moisture and temperature are vertically distributed due to gravity, solar radiation, precipitation, and infiltration. Accordingly, effective soil temperature T_{eff}^{s} was proposed to characterize this vertically varying temperature, defined as the equivalent temperature of ideal soil having the same microwave response to the natural soil (Schmugge and Choudhury, 1981).

Shortly after, Choudhury et al. (1982) proposed a simple parameterization of T_{eff}^{s}, expressed as

$$T_{\mathrm{eff}}^{s} = T_{\mathrm{depth}} + C_T\left(T_{\mathrm{surf}} - T_{\mathrm{depth}}\right), \quad \text{Eq. 2-2}$$

where T_{surf} and T_{depth} are the physical temperature of surface (0-5 cm) and deep (50-100 cm) soil; C_T determines the proportion of the surface and deep temperature contributions to T_{eff}^{s}.

Choudhury et al. (1982) initially calibrated C_T to be 0.084 at P-band and 0.246 at L-band (Choudhury's scheme). Later, Wigneron et al. (2001) proposed a soil moisture-dependent C_T (Wigneron's scheme), such that

$$C_T = (\mathrm{SM}/W_0)^{b_0}, \quad \text{Eq. 2-3}$$

where W_0 and b_0 are fitting parameters. This scheme was further refined by taking soil texture into account (Wigneron et al., 2008). Holmes et al. (2006) suggested C_T as a function of ε_r (Holmes's scheme)

$$C_T = ((\varepsilon_r''/\varepsilon_r')/\varepsilon_0)^{b_0}, \quad \text{Eq. 2-4}$$

where ε_0 and b_0 are fitting parameters.

More recently, Lv et al. (2014) developed a new two-layer effective temperature model by accounting for sensing depth (Lv's scheme). They also evaluated the four schemes mentioned above at the Maqu site in the Tibetan Plateau, discovering that the Lv's and Wigneron's schemes performed similarly (RMSE ~1.8-2.5 K) and better than the Holmes's (RMSE ~3.5 K) and Choudhury's (RMSE ~4.0 K) schemes.

2.3.4 Soil surface roughness

Soil roughness is well known to complicate the interpretation of microwave radiometer data and reduce the sensitivity of TB to soil moisture (Choudhury et al., 1979, Newton and Rouse, 1980, Newton et al., 1982, Njoku and O'Neill, 1982, Wang et al., 1983). The soil roughness effects are considered to result from a mixture of complex phenomena including 3-D soil spatial heterogeneities, volume scattering under dry soil

conditions, and soil anisotropy, making it impractical to model the effects physically (Panciera et al., 2009b, Wigneron et al., 2017).

A tractable semi-empirical roughness model (referred to as the HQN model) was initially proposed by Choudhury et al. (1979) and further developed by Wang and Choudhury (1981) and Prigent et al. (2000) to simulate the reflectivity (Γ_P) of flat soil surfaces exhibiting only random roughness

$$\Gamma_P = \left[(1 - Q_R)\Gamma_P^* + Q_R\Gamma_Q^*\right] \exp[-H_{RP}\cos^{N_{RP}}(\theta)], \quad \text{Eq. 2-5}$$

where the empirical parameters H_R, Q_R, and N_R characterize the intensity of the roughness effects, the difference between H- and V-pol reflectivity, and the polarization and angular dependence, respectively; Γ_P^* and Γ_Q^* (with P=H, Q=V or P=V, Q=H) are specular reflectivities.

The optimal values of H_R, Q_R, and N_R are still under discussion (Peng et al., 2017a). The H_R parameter is linked to a measurable parameter of the surface distribution, the root-mean-square (RMS) height (RMS height; also known as s) (Choudhury et al., 1979, Wang et al., 1983). Subsequently, a power-law relationship was found between H_R and the slope parameter $m = s/l$, where l is the correlation length of the soil surface (Mo and Schmugge, 1987, Wigneron et al., 2001). Later, Wigneron et al. (2011) established an equation, $H_R = (0.9437\,s\,/(0.8865\,s + 2.2913))^6$, and discovered that H_R saturated closing to 1.1-1.2 when s exceeded ~5-6 cm. Afterward, Lawrence et al. (2013) estimated H_R using a linear relationship to Z_S ($Z_S = s^2/l$) and computed Q_R and N_R from the estimated H_R. More recently, Montpetit et al. (2015) validated the equation by Wigneron et al. (2011) at various frequencies from 1.4 to 90 GHz and confirmed that H_R is rather insensitive to frequency, as noted earlier by Wang et al. (1983) and Pellarin et al. (2006).

While some studies have reported that H_R is insensitive to soil moisture (e.g., Wigneron et al., 2011, Lawrence et al., 2013), others showed contrary results with H_R increasing for dry soil conditions (Mo and Schmugge, 1987, Wigneron et al., 2001,

Escorihuela et al., 2007). Accordingly, soil moisture-dependent H_R has been investigated (Panciera et al., 2009a, Pardé et al., 2011, Peischl et al., 2012b). Wigneron et al. (2001) explained the soil moisture dependence of H_R as "dielectric roughness" due to the dielectric heterogeneity of drying-out soil. They also highlighted that the dielectric roughness is more important than the geometric roughness for dry soil and the converse for wet soil.

While Q_R is commonly believed to be zero at low frequencies (Wigneron et al., 2001, Wigneron et al., 2011, Lawrence et al., 2013), a few studies continued to assert a non-zero Q_R (Cano et al., 2010, Mialon et al., 2012, Peng et al., 2017a). Earlier, both N_{RH} and N_{RV} were usually set to 2 (Choudhury et al., 1979) or 0 (Wigneron et al., 2001, Njoku and Chan, 2006). However, Escorihuela et al. (2007) proposed that N_{RH} and N_{RV} are unnecessary to be the same, with 1 and -1 suggested, respectively. Lawrence et al. (2013) further suggested that the difference $\Delta N_R = N_{RH} - N_{RV}$ should be around 2 for smooth surfaces and 1-1.5 for rough surfaces.

Periodic (e.g., sinusoidal) row structures, a common type of soil tillage used for cultivation purposes, usually result in larger roughness impacts on radiometric observations compared to flat soil (Ulaby et al., 1986). The periodic soil surface consists of micro-scale random variations, i.e., random roughness, superimposed on a macro-scale one-dimensional surface undulation, i.e., periodic roughness (Ulaby et al., 1986, Gao, 2016). A common modeling approach is to simulate the micro-scale roughness and assume that the macro-scale roughness acts like topography by changing the local incidence angle of the micro-scale roughness (Wang et al., 1980, Ulaby et al., 2014, Neelam et al., 2020).

Wang et al. (1980) were the first to model the emissivity over a periodic surface at varying azimuth. However, the model was found to overestimate the influence of the row structure (Promes et al., 1988). While Promes et al. (1988) concluded that the periodic structures can be ignored in most cases without notable error at L-band, this has been challenged by Zheng et al. (2012), who showed that row structures can lead

to a retrieval error of up to 0.1 m^3/m^3. The results of Pham et al. (2005) also indicated that the azimuthal signal present in periodic row structures can lead to a retrieval error.

2.3.5 Vegetation canopy

Apart from roughness, the vegetation canopy attenuates (absorbs and scatters) the soil emission and adds its own contribution to the overall emission, resulting in a noticeable reduction in the sensitivity of TB to soil moisture (Jackson et al., 1982, Ulaby et al., 1983). Absorption occurs due to the non-zero imaginary part of the canopy's index of refraction, which is largely caused by the presence of liquid water within the vegetation tissue (Hornbuckle and England, 2004). Scattering occurs in some vegetation because the water's refractive index and the electrical size of the canopy constituents are large. The opacity of the canopy is usually characterized by the vegetation water content (VWC, in kg/m^2), defined as the mass of liquid water within the vegetation per unit area, and the canopy architecture.

The tau-omega (τ-ω) model proposed by Mo et al. (1982) models the TB response of vegetation-covered soil. It is essentially a zero-order solution of the radiative transfer equations where multiple scattering is neglected, with applicability and accuracy being widely evaluated at L- and C-band (Mo et al., 1982, Gao et al., 2018, Li et al., 2020). Optical depth τ and single scattering albedo ω characterize the vegetation extinction and scattering, defined as $\tau = \int_0^h \kappa_e dx$ and $\omega = \kappa_s/\kappa_e$, respectively, where extinction coefficient κ_e is the sum of absorption coefficient κ_a and scattering coefficient κ_s, and h is the canopy height. The τ is directly proportional to the VWC of the canopy, while the ω primarily depends on the type of vegetation (Mo et al., 1982).

The parameterization of τ and ω is crucial for soil moisture retrieval. Wigneron et al. (1995) proposed a tractable parameterization of τ to account for polarization dependence due to stem-dominated vegetation structures, further developed by Wigneron et al. (2007) such that

$$\tau_P = \tau_{\mathrm{NAD}}\left(\sin^2(\theta) \cdot tt_P + \cos^2(\theta)\right), \qquad \text{Eq. 2-6}$$

where τ_{NAD} is the optical depth at nadir, and the structural parameter tt_P accounts for the vegetation anisotropy effects concerning incidence angle and polarization. In an isotropic case where τ is independent of polarization and incidence angle, $tt_H = tt_V = 1$ can be assumed. At a vineyard, Schwank et al. (2012) observed a larger difference of tt_H and tt_V in winter (~0.80 and ~0.11, respectively) than in summer (~1.40 and ~1.10, respectively), as a result of the more isotropic leafy components dominating the vine structure in summer.

The τ_{NAD} was first found to be a function of the dry biomass and the moisture content of vegetation by Kirdiashev et al. (1979). Later, τ_{NAD} was estimated by linearly linking to VWC (Jackson et al., 1982, Jackson and O'Neill, 1990)

$$\tau_{\mathrm{NAD}} = b \cdot \mathrm{VWC}, \qquad \text{Eq. 2-7}$$

where empirical parameter b is a proportionality value depending on the vegetation type and structure and the observation frequency. Even though b is somewhat dependent on vegetation growth stages and polarizations (Wigneron et al., 2004), it is commonly assumed to be time- and polarization-invariant for simplicity (Wigneron et al., 2007).

Wigneron et al. (2007) proposed a linear function of τ_{NAD} and Leaf Area Index (LAI)

$$\tau_{\mathrm{NAD}} = b' \cdot \mathrm{LAI} + b'', \qquad \text{Eq. 2-8}$$

where b' and b'' are empirical parameters determined mainly by the vegetation structure. Wigneron et al. (2007) also calibrated b' and b'' using experimental datasets over soybean, wheat and corn. Afterward, Lawrence et al. (2014) investigated the SMOS optical depth product and the Moderate Resolution Imaging Spectroradiometer (MODIS) LAI product over the crop area of the USA and estimated average b' and b'' values to be 0.06 and 0.14, respectively.

According to a wealth of ground-based calibrations, ω is close to zero at L-band, except for grass (~0.05) and corn (~0.05-0.13) (Wigneron et al., 2004, Wigneron et al., 2007, Yan et al., 2015). Moreover, Kurum (2013) reported that the ω of a corn canopy varied between 0.05 and 0.10 at H-pol and between 0.10 and 0.15 at V-pol, indicating

the polarization dependence. While the temporal variations of ω were noted (Wigneron et al., 2004), in most cases ω was assumed to be time-invariant in the literature (Gao et al., 2017, Zheng et al., 2018, Zhao et al., 2021b). Two global maps of ω were produced by Entekhabi et al. (2014) with SMOS data, and by Konings et al. (2016) with Aquarius observations, to improve soil moisture retrieval. Nevertheless, Van der Schalie et al. (2016) observed no benefit from using spatially varying ω maps.

Some limitations of the tau-omega model have been highlighted by Wigneron et al. (2017): first, it does not account for multiple scattering effects; and second, it inherently assumes small dielectric gradients between the air and vegetation canopy, implying that both the reflection and refraction at the air-to-vegetation interface are neglected. These assumptions are reasonable for L-band over sparsely vegetated soil (Wigneron et al., 1993b) but not as adequate when forests or litter/snow cover exists. Branches of forests have different dielectric and scattering properties from herbaceous components, leading to substantial single and multiple scattering that cannot be neglected even at L-band. Nevertheless, the tau-omega model can reportedly still be used over forests provided τ and ω are regarded as effective parameters and calibrated (Ferrazzoli et al., 2002, Kurum et al., 2012).

Unlike the tau-omega model, a "two-stream" model (2S model) was developed to simulate multiple volume scattering and absorption in the context of the Microwave Emission Model for Layered Snowpack (MEMLS) (Mätzler, 1998, Wiesmann and Mätzler, 1999). As a first-order solution of the radiative transfer equation, this model could become a substitute for the tau-omega model over soil covered by dense vegetation, litter, or dry snow (Lemmetyinen et al., 2016). While Li et al. (2020) concluded that the retrieval results from using the tau-omega and the 2S models are similar at global scale, the latter holds a stronger physical background and can potentially unify various emission models in different applications.

2.4 Soil Moisture Retrieval Algorithms

Soil moisture can be estimated by iteratively running the forward model to minimize a cost function (CF) computed from the differences between observed ($\mathrm{TB}_P^{\mathrm{obs}}$) and simulated ($\mathrm{TB}_P$) TB, expressed as (Pulliainen et al., 1993)

$$\mathrm{CF} = \frac{\Sigma\left(\mathrm{TB}_P^{\mathrm{obs}} - \mathrm{TB}_P\right)^2}{\sigma(\mathrm{TB})^2} + \sum_i \frac{\left(\mathrm{P}_i^{\mathrm{ini}} - \mathrm{P}_i\right)^2}{\sigma(\mathrm{P}_i)^2}, \qquad \text{Eq. 2-9}$$

where $\mathrm{P}_i^{\mathrm{ini}}$ and P_i (i is the number of retrieved parameters) are the initial value and the value of the retrieved parameters, i.e., soil moisture, H_R, b, and/or any other parameters in the forward model to be determined; and $\sigma(\mathrm{TB})$ and $\sigma(\mathrm{P}_i)$ are the standard deviation related to these variables that are usually empirically tuned to constrain these variables and adjust the convergence of the inversion.

Mathematically, soil moisture retrieval is a process that seeks an optimized solution within an i-dimension space. The consideration of roughness and vegetation impacts brings more parameters (i.e., H_R, Q_R, N_{RP}, τ, b, ω, tt_P, etc.) and thus substantially increases the dimension and complexity of the solution. Moreover, these parameters and soil moisture tangle together, making soil moisture retrieval more challenging (Martens et al., 2015, Zwieback et al., 2019). In general, the number of TB observations should be no fewer than that of retrieved parameters to guarantee a robust result. Otherwise, it becomes an ill-posed retrieval with multiple solutions.

Efforts have been made from two aspects to address this ill-posed problem, i.e., 1) reducing the number of unknowns based on prior knowledge and assumptions (Jackson and O'Neill, 1990, Wigneron et al., 2011, Martens et al., 2015, Parrens et al., 2017) and 2) augmenting the observations by using multiple observing incidence angles, polarizations, times, and/or frequencies (Grant et al., 2010, Konings et al., 2016, Zhao et al., 2021b).

Due to the reasons mentioned above, some of these parameters (e.g., H_R, Q_R, b, and ω) are usually assumed to be independent of incidence angle, polarization, and time

(Wigneron et al., 2007, Neelam et al., 2020, Gao et al., 2021). Although some experiments have confirmed that this assumption is not always true (Wigneron et al., 2004, Grant et al., 2010, Jiang et al., 2019, Zhao et al., 2020a), it is reasonable at least at the scale of spaceborne observations where the dependence effects tend to be averaged out (Owe et al., 2001).

Konings et al. (2015) identified that a robust retrieval can only be guaranteed if some redundant TB observations are provided, given that even the observations at different angles, polarizations, and times still contain mutual information. Accordingly, they proposed the concept of degree of information (DoI) and suggested that the DoI of a set of observations should be larger than the number of the retrieved parameters. Based on this theory, Zhao et al. (2021b) presented that multi-frequency observations have a slightly larger DoI than multi-angular observations if maintaining the same number of channels.

Since the tau-omega model simplifies the complex calculation of the radiative transfer equation yet retains a similar accuracy, many retrieval algorithms have been developed based upon it and widely employed; e.g., the single channel algorithm (SCA, Jackson, 1993) for SMAP, the L-band microwave emission of the biosphere (L-MEB) model (Wigneron et al., 2007) for SMOS, the dual channel algorithm (DCA, Njoku and Li, 1999, Njoku et al., 2003), the land parameter retrieval model (LPRM, Owe et al., 2001), the multi-temporal dual channel algorithm (MT-DCA, Konings et al., 2016, Konings et al., 2017) and so on. One of the major differences is whether τ is concurrently retrieved with soil moisture or estimated based on ancillary data prior to the inversion process.

2.4.1 The SMOS algorithm

The L-MEB model was developed by Wigneron et al. (2007) to simultaneously retrieve soil moisture and τ (2-Parameter retrieval) by utilizing SMOS multi-angular and dual-polarized observations according to the following interests (Kerr et al., 2019): 1) there is no requirement for ancillary vegetation data; and 2) the retrieved τ is likely to

become a beneficial product by itself for monitoring vegetation dynamics. However, retrieving two or more parameters at the same time is challenging due to their mutual dependence, typically resulting in degraded soil moisture retrieval accuracy. In the SMOS algorithm, a given pixel is classified into different fractions according to a high-resolution (1 km) land cover map. Subsequently, all fraction contributions are aggregated into the TB for this given pixel.

Initially, the SMOS baseline algorithm used the Dobson model revised by Peplinski et al. (1995a, b). Since the Algorithm Theoretical Baseline Document (ATBD) version 3.f, the Mironov model (Mironov et al., 2013a), which was dedicatedly designed for the SMOS algorithm with simplified and specific equations at L-band, has been adopted as the default choice due to the following reasons (Wigneron et al., 2017, Kerr et al., 2019): 1) it is a more physical-based model that provides more robust results when soil moisture is close to zero; 2) it requires fewer input parameters, i.e., soil moisture, temperature, and clay fraction, reducing the uncertainties from auxiliary datasets especially soil density; and 3) it is valid for more extensive soil texture, whereas the Dobson model has some limitations for dry and sandy soil (Drusch et al., 2009). In the recent SMOS ATBD version 4.a, the Bircher empirical model (Bircher et al., 2017) was introduced for organic soil.

The SMOS baseline algorithm uses Eqs. 2-2 and 2-3 as the effective soil temperature model with the default values $W_0 = 0.3$ m^3/m^3 and $b_0 = 0.3$ (Wigneron et al., 2008). The T_{surf} and T_{depth} are derived from Layer 1 and 3, respectively, of the European Centre for Medium-Range Weather Forecasts (ECMWF) soil temperature forecasts. Currently, the SMOS algorithm adopts the HQN model for characterizing the soil surface roughness impact. Estimating H_R, Q_R, and N_{RP} using the in-situ roughness measurements is impractical due to the impossibility of regularly performing such labor-intensive measurements across the globe. As a compromise, SMOS relies on a look-up table to provide constant H_R values for the main land cover types, e.g., 0.1 for barren or sparsely vegetated soil and 0.3 for forests. Other parameters are assumed such that $Q_R = 0$, $N_{RH} = 2$, and $N_{RV} = 0$. Similar to H_R, ω is assumed to be polarization-

and angle-independent and determined based upon a look-up table, e.g., 0 for barren or sparsely vegetated soil and 0.06-0.08 for forests. The skin temperature of the ECMWF forecasts is used as the effective vegetation temperature.

2.4.2 The SMAP algorithm

Algorithms considered in the SMAP ATBD included the SCA with either H- or V-pol observations (referred to as SCA-H and SCA-V), the DCA, the LPRM, and the Extended Dual Channel Algorithm (E-DCA, Chan et al., 2016). However, the latter two algorithms have been discontinued since the R16.3 data release, and therefore SMAP now provides soil moisture datasets from the former three algorithms (O'Neill et al., 2021a). The SCA-V was the original post-launch baseline algorithm for SMAP from 2015 to 2021 due to its superior performance over the other algorithms (Chan et al., 2016).

According to the latest evaluation of the SMAP Level 2 Soil Moisture Passive (L2SMP) Version 8 using in-situ validation sites (O'Neill et al., 2021b), the SCA-V and the DCA had the same best overall performance of ~0.036 m^3/m^3 in ubRMSE, fulfilling the 0.04-m^3/m^3 target accuracy of SMAP. However, the DCA showed better ubRMSE than the SCA at two agricultural sites. Consequently, the DCA has been adopted as the SMAP baseline algorithm since October 2021 (O'Neill et al., 2021a).

The SCA is a 1-Parameter retrieval approach that requires ancillary information to parameterize roughness and vegetation impacts (Jackson, 1993). The SMAP SCA applies Eqs. 2-6 and 2-7 to estimate τ, with H_R, ω and b being determined globally using look-up tables itemized according to the International Geosphere-Biosphere Programme classification. The VWC in Eq. 2-7 is calculated by utilizing a set of land cover-based equations from the Normalized Difference Vegetation Index (NDVI) dataset. Other parameters are assumed such that $Q_R = 0$, $N_{RH} = N_{RV} = 2$, and $tt_H = tt_V = 1$.

Unlike the SCA, the DCA (Njoku and Li, 1999, Njoku et al., 2003) is a 2-Parameter algorithm that uses observations at dual polarizations to retrieve soil moisture and τ concurrently, and therefore Eqs. 2-6 and 2-7 are no longer needed. The SMAP DCA uses a global map of H_R with varying values from pixel to pixel. In addition, while N_{RP} is assumed to be 2 as in the SCA, Q_R is no longer assumed to be zero but linearly related to H_R by $Q_R = 0.1771 H_R$ (O'Neill et al., 2021a). The ω is also determined globally using look-up tables as in the SCA but with different values. An implicit assumption is that τ is identical at both polarizations in the SMAP DCA approach.

All of the three dielectric mixing models (Wang and Schmugge, 1980, Dobson et al., 1985, Mironov et al., 2009) are coded in the SMAP software, while the Mironov model (Mironov et al., 2009) is the baseline option in the Level 2 & 3 passive algorithms. The Choudhury's scheme (Eq. 2-2) is adopted with $C_T = 0.246$ for the descending product and $C_T = 1$ for the ascending product. The SMAP algorithm derives T_{surf} and T_{depth} from the NASA Goddard Earth Observing System-Forward Processing soil temperature forecasts. It is worth noting that the SMAP algorithms multiply the right-side term of Eq. 2-2 by a factor of 0.1007 to correct the bias between the temperature forecasts and in-situ measurements (O'Neill et al., 2021a). In addition, the 6:00 am (local time) descending overpass time minimizes the difference between soil and canopy temperature. Consequently, the effective temperature is assumed to be the same for soil and vegetation canopy.

2.4.3 Other algorithms

The LPRM is an index-based retrieval model that firstly computes τ based on the Microwave Polarization Difference Index (MPDI) and then retrieves soil moisture. The MPDI characterizes the polarization difference and was found to be a good proxy of τ, expressed as (Owe et al., 2001)

$$\text{MPDI} = (\text{TB}_V - \text{TB}_{H)}/(\text{TB}_V + \text{TB}_H). \qquad \text{Eq. 2-10}$$

The LPRM was initially implemented on a multi-frequency satellite (Owe et al., 2001, de Jeu et al., 2008, Owe et al., 2008), the Advanced Microwave Scanning Radiometer

- Earth Observing System sensor (AMSR-E) flown onboard the Aqua satellite, where the effective temperature can be derived from the Ka-band V-pol observations. Afterward, it was also applied to L-band airborne (De Jeu et al., 2009) and spaceborne observations (van der Schalie et al., 2015, Gao et al., 2021). Please refer to the literature (Owe et al., 2001, Meesters et al., 2005, De Jeu et al., 2009) for the detailed equations of this model.

The MT-DCA retrieves τ and soil moisture from time series of L-band observations at dual polarizations (Konings et al., 2016, Konings et al., 2017). A single τ is estimated from a range of consecutive observations by assuming that the early morning VWC is constant across a few days. Along with τ and soil moisture, a time-invariant scattering albedo is also retrieved by this algorithm. Other algorithms that may not be covered in this chapter include the constrained multi-channel algorithm (Ebtehaj and Bras, 2019), the spatially constrained multi-channel algorithm (Gao et al., 2020), and machine learning-based algorithms (Ali et al., 2015, Yuan et al., 2020).

2.5 Knowledge Gap and Objective

The widely accepted L-band technology can only provide soil moisture information for no more than the top 5-cm layer of soil due to the limited moisture sensing depth (Escorihuela et al., 2010, Liu et al., 2012a, Zheng et al., 2019). In principle, moisture sensing depth depends on the soil moisture condition and the observation frequency, ranging from approximately one-tenth to one-fourth of the wavelength (Wilheit, 1978, Schmugge and Choudhury, 1981, Newton et al., 1982, Newton et al., 1983, Waite et al., 1984, Ulaby et al., 1986, Raju et al., 1995). While the temperature sensing depth was calculated to be approximately 10 cm at L-band and 20 cm at P-band for a 0.3-m^3/m^3 moisture condition (Njoku and Entekhabi, 1996), such a demonstration for moisture sensing depth is still lacking.

According to the Fraunhofer criterion (Ulaby et al., 1982), a surface may be considered electromagnetically smooth in the microwave range if the RMS height s is less than $\lambda/(32\cos(\theta))$. This criterion asserts that observations at longer wavelengths should be

less affected by soil roughness than those at shorter wavelengths, which has also been demonstrated by a few experiments at L-band and higher frequencies (Blinn and Quade, 1972, Wang et al., 1983). Apart from roughness, the vegetation impact has also been demonstrated to be more significant at 2.8-cm wavelength than at 21.4-cm wavelength (Newton and Rouse, 1980).

The above-hypothesized benefits of longer wavebands are promising but have not yet been experimentally demonstrated at P-band. Accordingly, this thesis aimed at verifying the potential of P-band for greater moisture sensing depth and reduced sensitivity to soil roughness and vegetation compared to the widely used L-band.

2.6 Challenges of a Successful P-band Radiometer Mission

While P-band is a promising proposition to replace or enhance the current L-band SMOS and SMAP missions in the forthcoming years, so as to obtain deeper and more accurate soil moisture information, there remain four challenges: aperture size, RFI, receiver design and calibration, and ionospheric and celestial emission effects (Johnson et al., 2021).

With the spatial resolution of a radiometer determined by the aperture size relative to the observing wavelength for a given orbit altitude, the aperture of a 0.75-GHz radiometer needs to be enlarged by 1.87 times to retain the same 40-km spatial resolution of the 1.4-GHz radiometer of SMAP, i.e., increasing from the 6-m diameter antenna of SMAP to an 11.22-m diameter antenna. This principle also holds true for a synthetic aperture radiometer, which allows use of a thinned array antenna to have simultaneous multi-angular observations (Johnson et al., 2021).

Unlike L-band (1.400-1.427 GHz) that is exclusively allocated for radio astronomy use, P-band (0.3-1 GHz) is heavily occupied by television broadcast, communications, and other applications (National Research Council, 2010), easily causing RFI and corrupting radiometric measurements from the target. Although strong RFI is easy to detect, its cancellation is challenging due to that it relies on the geo-localization

accuracy of the RFI source (Camps et al., 2014). Compared to strong RFI, weak RFI is more difficult to detect and thus harder to mitigate properly. Additionally, at 0.75 GHz, the amount of Faraday rotation and ionosphere-specific attenuation is approximately 3.5 times as large as at 1.4 GHz, which needs to be corrected for satellite operations.

Nowadays, large deployable antennas (e.g., Meguro et al., 2009) and highly developed downscaling techniques (Peng et al., 2017b, Sabaghy et al., 2018) make higher spatial resolution at P-band possible. Moreover, RFI mitigation techniques are becoming increasingly mature (Skou et al., 2009, Huang et al., 2018, Jin et al., 2019). The ultra-wideband software defined microwave radiometer (UWBRAD) is a successful example in this regard, demonstrating how a future P-band radiometer-based mission might address the RFI issue (Johnson et al., 2016, Yardim et al., 2021). The UWBRAD detects and filters RFI by segmenting the observed bandwidth (from 0.5 to 2 GHz) into 12 channels, each of which is further resolved into 512 subchannels. Despite a cost of data loss, the RFI-free portions of the spectrum can be identified and integrated. These advancements in aerospace and remote sensing technologies pave the way for a successful P-band radiometer-based mission in the near future.

2.7 Chapter Summary

The first investigation on P-band radiometers dates back to the late 1970s (Njoku and O'Neill, 1982). However, this technology was not pursued because of severe RFI in their instrument degrading the interpretation of the data, and the coarse spatial resolution at P-band compared to higher frequencies for the same antenna size. Since then, this technique has been largely forgotten in soil moisture sensing until now, where the situation has changed considerably. Remote sensing technologies have grown rapidly in the past half century. In this context, a P-band mission is more likely to be launched now than ever in the past, motivating this PhD research to experimentally demonstrate the postulated benefits of using P-band radiometric observations for soil moisture sensing.

This page is intentionally left blank.

3 Data

To bridge the knowledge gaps identified in Chapter 2, a comprehensive field experiment has been conducted, i.e., the P-band Radiometer Inferred Soil Moisture (PRISM, see https://www.prism.monash.edu) project. It comprises a long-term tower experiment (2017-2021) and four airborne campaigns (2017, 2018, 2019, and 2021). This thesis employed the PRISM tower-based data from 2019 to 2021 to investigate the soil moisture sensing capability of the P-band radiometer from three aspects of moisture retrieval depth, roughness, and vegetation impact. Collaborating with other colleagues, I was responsible for making experiment plans and logs, maintaining equipment, and collecting, processing and archiving data.

3.1 Field Configuration

The PRISM tower site was established at Cora Lynn, Victoria, Australia (Figure 3-1a) from October 2017 to May 2021. The field was 160 m by 160 m in size and divided

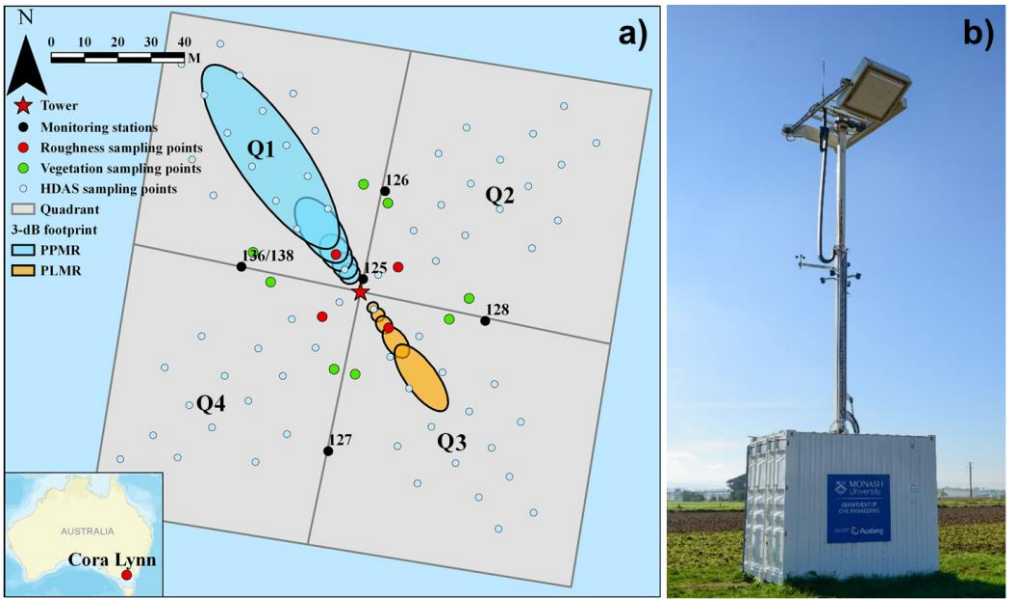

Figure 3-1: Illustrations of the PRISM tower site, including a) location map with the PPMR and PLMR footprints for incidence angles of 30°, 40°, 50°, 60°, and 70° from the center outwards, respectively; and b) the tower carrying the PPMR and PLMR.

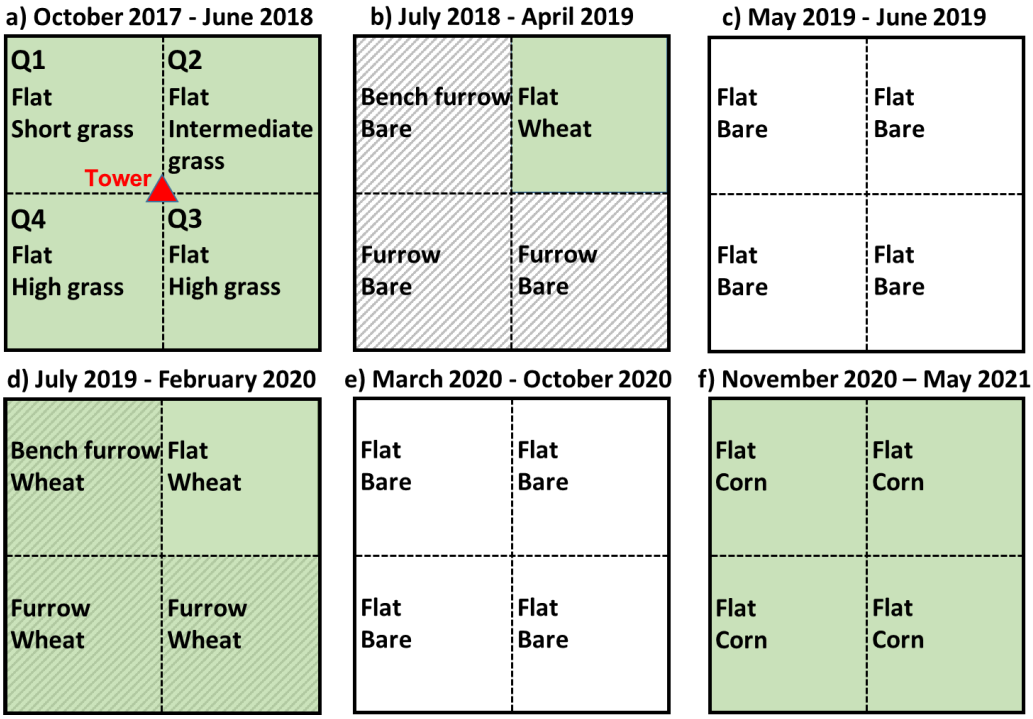

Figure 3-2: Field conditions for each subperiod during the tower experiment.

into four quadrants (numbered as Q1-Q4 from the northwest clockwise) with different soil surface roughness and/or vegetation conditions for comparison. A ten-meter-high tower was installed at the center of the field (Figure 3-1b).

From time to time, the field was managed with different configurations. Figure 3-2 depicts the different conditions of the field in each subperiod during the experiment. A range of roughness conditions were configured by ploughing the soil with different tillage. The RMS height ranged from ~0.5 cm for flat soil to ~8 cm for furrowed soil. Three types of vegetation, i.e., grass, wheat, and corn, were planted in the field to cover

Table 3-1: A summary of data used in each analysis chapter.

Chapter	Period	Quadrant	Station
5	May 9 - June 12, 2019	4	125
6	July 17 - 31, 2019	1-4	126, 127
7	November 13 - December 21, 2019	1-4	126, 127
8	November 24, 2020 - May 4, 2021	2	126

a large range of VWC, being up to ~2, ~4, and ~20 kg/m^2, respectively. Table 3-1 summarizes the period and quadrant of the data used in the following analysis chapters.

3.2 Tower-based Observations

The tower carried two different radiometers, the Polarimetric P-band Multi-beam Radiometer (PPMR, Figure 3-3a) and the Polarimetric L-band Multi-beam Radiometer (PLMR, Figure 3-3b). It automatically rotated the mast (changed azimuth) on a schedule such that PPMR and PLMR alternately observed the same four quadrants (Figure 3-4). Each position in Figure 3-4 lasted 30-45 minutes (totaling ~2-3 hours for a cycle), during which the instruments were tilted (changed zenith) every 5-10 minutes to produce a range of incidence angles from 30° to 70°, with the footprints as shown in Figure 3-1a. The P- and L-band observations for the same quadrant and incidence angle were separated by around 30 minutes, making them comparable when assuming constant soil moisture and temperature over this period. The continuous TB observations for each quadrant and each incidence angle were averaged before analysis.

The specifications of the PPMR and PLMR are provided in Table 3-2. The PPMR and PLMR operate at 0.742-0.752 GHz and 1.401-1.425 GHz, respectively. The PPMR has four antenna beams with 30° beamwidth, while the PLMR has six antenna beams

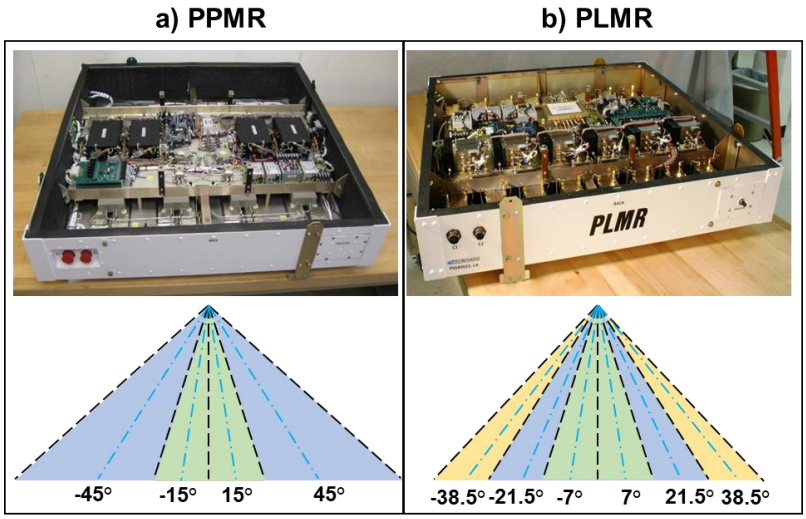

Figure 3-3: Photos and beam positions of a) the PPMR and b) the PLMR.

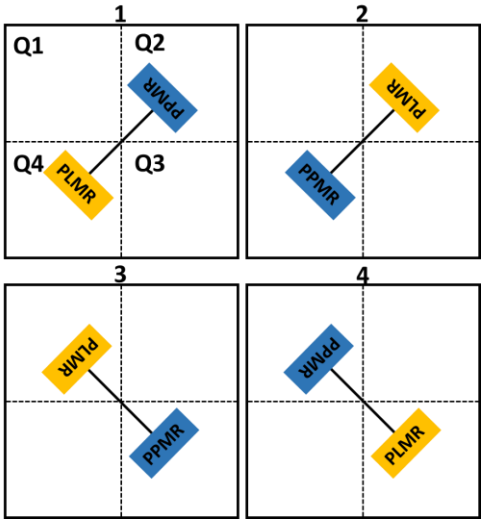

Figure 3-4: The four-step tower rotation cycle.

incidence angle, the spatial resolution of the 3-dB footprints of the PPMR and PLMR were approximately 8.2 m × 7.0 m and 4.0 m × 4.0 m, respectively. Radiometer footprints were approximated to be an ellipse (Figure 3-1a) and estimated using geometric information including tower height, pointing angles of beams, and beamwidth.

Warm and cold calibration of PPMR and PLMR were performed regularly: the former was undertaken by positioning the PPMR and PLMR over a blackbody chamber constructed from microwave absorber having 16 temperature sensors to provide the reference TB; the latter was performed every midnight according to the tower schedule

Table 3-2: Specifications of the PPMR and PLMR.

Specification	PPMR	PLMR
Frequency	0.742-0.752 GHz	1.401-1.425 GHz
Polarization	H & V	H & V
Observation mode	Four beams at each polarization with pointing angles of ±15° and ±45° from nadir.	Six beams at each polarization with pointing angles of ±7°, ±21.5° and ±38.5° from nadir.
Beamwidth	30°×30°	17°×15°

by pointing the PPMR and PLMR towards the sky for 2 hours. The reference TB of the sky was taken to be constant and calculated to be 13.9 K at P-band and 5.3 K at L-band (ITU, 2015). The RMSE between the measurements of the calibration target and the reference, i.e., the calibration accuracy, was determined to be better than 1.5 K for both the PPMR and PLMR (Ye et al., 2020b). Note that the use of "P-band" and "L-band" hereafter specifically refers to the frequencies at which PPMR and PLMR operate unless otherwise specified.

3.3 Ground-based Observations

The temporal evolution of soil moisture and temperature was monitored by the five stations (126, 127, 128, 136, and 138) installed at the four edges of the four quadrants to avoid any perturbation to the footprints of the radiometers (Figure 3-1a). Stations 136 and 138 were installed side by side at the edge shared by Q1 and Q4 (Figure 3-1a). Temporary station 125 was installed only when cultivation activities required the removal of all other stations. Stations 126, 127, 128, and 136 had 12 hydra-probes with

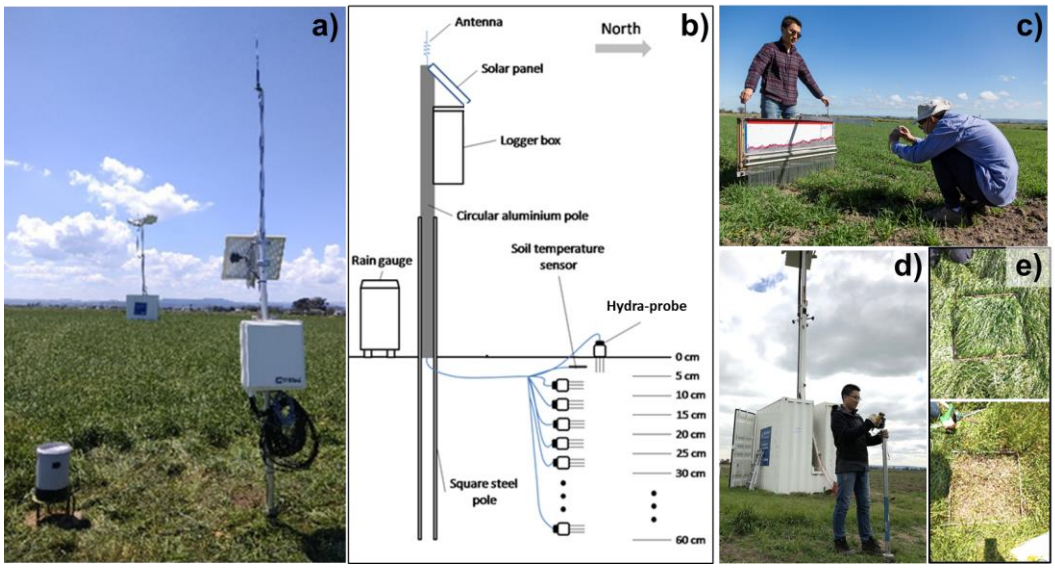

Figure 3-5: Illustrations of the ground measurements, including a) a station monitoring soil moisture, temperature, and rainfall evolution; b) a diagram showing the station installation; c) soil surface roughness measurement with the pin-profiler; d) surface soil moisture measurement using HDAS; and e) an example of destructive vegetation sampling.

5-cm-long pins inserted into the soil at 5-cm increments down to 60 cm, while station 125 had five hydra-probes and station 138 had six hydra-probes at 5-cm increments, with measurements covering each 5-cm increment (Figure 3-5a and b). The top probe was installed vertically from the surface while the others were installed horizontally (Figure 3-b). These probes continuously measured soil temperature and moisture and logged the average readings at a 20-minute sampling step.

To validate that the stations can represent the soil moisture over the instrument footprints, the spatial homogeneity of the soil moisture at this site was assessed by weekly surface soil moisture (~5 cm) measurements using the Monash University Hydra-probe Data Acquisition System (HDAS, Merlin et al., 2007). Demonstrating the homogeneous soil moisture distribution in this field can also support the neglect of the difference across PPMR and PLMR footprints (Figure 3-1a). The HDAS consists of a hydra-probe soil moisture sensor and a microcomputer integrated with a Geographic Information System (GIS) and Global Position System (GPS). Three measurements were performed within a 1-m radius at each sampling location shown in Figure 3-1a. A sampling photo is provided in Figure 3-5d. The hydra-probes used in this study were calibrated according to Merlin et al. (2007) and checked on-site using gravimetric samples, showing a satisfactory performance with a 0.96 R and a 0.04-

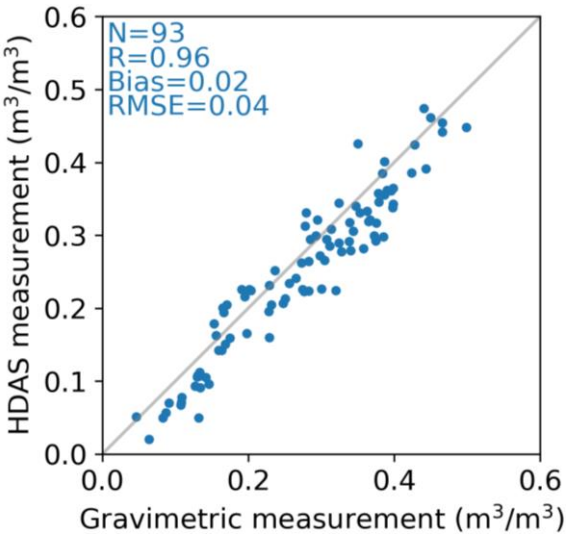

Figure 3-6: HDAS against gravimetric soil moisture measurement in the 0-5-cm soil layer.

m^3/m^3 RMSE (Figure 3-6). Note that these HDAS measurements were not used in the formal analysis throughout this thesis but were only used for checking the homogeneity of the soil moisture across the field and the representativeness of the stations.

Soil roughness measurements were conducted at the locations in Figure 3-1a using a pin-profiler with an ~0.5-cm pin interval (Figure 3-5c). Three consecutive 1-m measurements (i.e., 3-m in total) in two perpendicular directions were performed at every sampling location on every sampling day. Photographs of the pin-profiler were taken during measurements, and the heights of the red pin tops in the photographs were derived from image processing for calculating the roughness statistics, e.g., RMS height and correlation length. Although it has been suggested that a roughness profile longer than 10 m is required to guarantee a good precision (Oh and Kay, 1998, Baghdadi et al., 2000), such a long profile is not practical to measure in field experiments, and so a 3-m profile has been widely taken as a compromise (McNairn et al., 2014, Neelam et al., 2020, Ye et al., 2020a, Zhao et al., 2020b).

VWC was calculated from weekly destructive vegetation sampling (Figure 3-5e) at the locations as shown in Figure 3-1a. In addition, soil properties of the 0-5-cm soil layer at this site were investigated by laboratory experiments, including soil texture, bulk density, saturated soil moisture, field capacity, permanent wilting point, air-dry soil

Table 3-3: Soil properties of the 0-5-cm soil layer.

Property	Unit	Value
Soil texture	-	Silty loam
Clay	%	18.0
Silt	%	71.1
Sand	%	10.9
Bulk density	g/cm^3	0.87
Saturated soil moisture	m^3/m^3	67.32
Field capacity	m^3/m^3	33.25
Permanent wilting point	m^3/m^3	19.42
Air-dry soil moisture	m^3/m^3	5.19
Conductivity	S/m	0.0193

moisture, and conductivity (Table 3-3), which were used in the dielectric model throughout this thesis.

Throughout this thesis, the radiometer and station observations in the 6 am rotation cycle were used because the soil temperature and dielectric profiles are likely to be more uniform at 6 am than other times of the day (Basharinov and Shutko, 1975). n addition, the difference between soil and canopy temperature is also minimized (Entekhabi et al., 2014). The current study used the daily TB observations at around 40° incidence angle for both P- and L-band to approximate the configuration of SMAP (Entekhabi et al., 2014). Moreover, Zhao et al. (2020a) provide support by showing that 40° to 45° provided the best retrieval accuracy. Consistent with the TB observations, the soil moisture and temperature in the 6 am rotation cycle were averaged for each station to be analyzed.

3.4 Chapter Summary

This chapter presents an overview of the PRISM tower-based experiment, the field configuration, and the data used in this research, mainly including the tower-based TB observations along with the soil moisture and temperature measurements from stations. Ancillary data are also introduced from the aspects of spatial soil moisture, soil roughness, vegetation, and soil property measurements. In addition, the datasets adopted in each of the analysis chapters (Chapters 5 to 8) are identified. Please also refer to those chapters for more details of the dataset.

4 Model

This chapter presents in detail the models for TB/emissivity simulation used in this thesis, i.e., the tau-omega model, the Njoku model, and the I^{2}EM. The former two are based on the radiative transfer equation: the tau-omega model is a zero-order noncoherent model that implicitly assumes uniform soil moisture and temperature with depth, while the Njoku model is a stratified coherent model that is able to account for non-uniform soil moisture and temperature with depth. The emissivity of a soil surface can also be computed by integrating the total bistatic scattering over the upper hemisphere, with the I^{2}EM bistatic scattering model enabling such a computation. Each of these three models relies on a dielectric mixing model to link to the soil moisture. Accordingly, the Mironov model used throughout this thesis is also introduced in this chapter.

4.1 Tau-Omega Model

The well-known tau-omega model (Mo et al., 1982) characterizes the brightness temperature of the thermal emission (TB_P, where subscript P denotes either H or V polarization) from a vegetated soil surface with four terms (Figure 4-1), i.e., 1) the direct upward emission from vegetation ($\mathrm{TB}_P^{\mathrm{v\_up}}$); 2) the downward vegetation emission reflected by the soil and attenuated by the canopy layer ($\mathrm{TB}_P^{\mathrm{v\_down}}$); 3) the upward soil emission attenuated by the canopy layer ($\mathrm{TB}_P^{\mathrm{s}}$), and 4) the downwelling sky emission ($\mathrm{TB}^{\mathrm{sky\_down}}$) reflected by the soil and attenuated twice by the canopy layer ($\mathrm{TB}_P^{\mathrm{sky}}$), formulated as (Ulaby et al., 2014)

$$\mathrm{TB}_P = \mathrm{TB}_P^{\mathrm{v\_up}} + \mathrm{TB}_P^{\mathrm{v\_down}} + \mathrm{TB}_P^{\mathrm{s}} + \mathrm{TB}_P^{\mathrm{sky}} = (1-\omega)(1-\gamma_P)T_{\mathrm{eff}}^{\mathrm{v}} + (1-\omega)(1-\gamma_P)\gamma_P\Gamma_P T_{\mathrm{eff}}^{\mathrm{v}} + (1-\Gamma_P)\gamma_P T_{\mathrm{eff}}^{\mathrm{s}} + \mathrm{TB}^{\mathrm{sky\_down}}\Gamma_P\gamma_P^2, \quad \text{Eq. 4-1}$$

where γ_P and $T_{\mathrm{eff}}^{\mathrm{v}}$ are the transmissivity and effective temperature of the vegetation canopy, and Γ_P and $T_{\mathrm{eff}}^{\mathrm{s}}$ are the reflectivity and effective temperature of the soil. The $T_{\mathrm{eff}}^{\mathrm{v}}$ was assumed to be equal to the physical soil temperature in the 0-5-cm layer

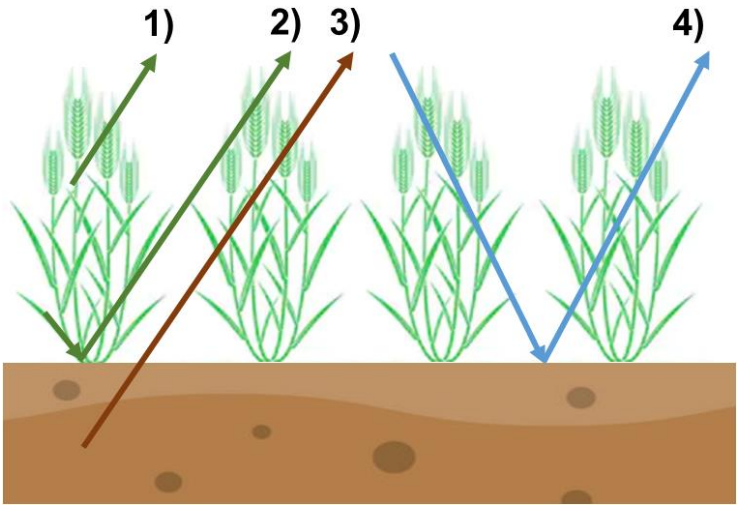

Figure 4-1: Schematic of the tau-omega model, including 1) the direct upward emission from vegetation, 2) the downward vegetation emission reflected by the soil and attenuated by the canopy layer, 3) the upward soil emission attenuated by the canopy layer, and 4) the downwelling sky emission reflected by the soil and attenuated twice by the canopy layer.

because the difference between canopy and soil temperature is minimal at 6 am (Fagerlund et al., 1970). Moreover, $\mathrm{TB}^{\mathrm{sky\_down}}$ was assumed to be constant and calculated to be 13.9 K at P-band and 5.3 K at L-band (ITU, 2015). Kirchhoff's reciprocity theorem relates emissivity (e_P) to Γ_P through

$$e_P = 1 - \Gamma_P. \qquad \text{Eq. 4-2}$$

The vegetation transmissivity (γ_P) was computed from the optical depth τ_P using Beer's law such that

$$\gamma_P = \exp\left(-\frac{\tau_P}{\cos(\theta)}\right), \qquad \text{Eq. 4-3}$$

with τ_P being a function of VWC and an empirical parameter b (Eq. 2-7).

For bare soil, Eq. 4-1 can be simplified to

$$\mathrm{TB}_P = \mathrm{TB}_P^{\mathrm{s}} + \mathrm{TB}_P^{\mathrm{sky}} = (1 - \Gamma_P)T_{\mathrm{eff}}^{\mathrm{s}} + \mathrm{TB}^{\mathrm{sky\_down}}\Gamma_P, \qquad \text{Eq. 4-4}$$

where Γ_P can be computed using the HQN model (Eq. 2-5). The specular reflectivity Γ_P^* and Γ_Q^* in Eq. 2-5 can be calculated from the Fresnel equations as a function of ε_r, such that

$$\Gamma_H^* = \left|\frac{\cos(\theta)-\sqrt{\varepsilon_r-\sin^2(\theta)}}{\cos(\theta)+\sqrt{\varepsilon_r-\sin^2(\theta)}}\right|^2 \quad \text{Eq. 4-5}$$

$$\Gamma_V^* = \left|\frac{\varepsilon_r\cos(\theta)-\sqrt{\varepsilon_r-\sin^2(\theta)}}{\varepsilon_r\cos(\theta)+\sqrt{\varepsilon_r-\sin^2(\theta)}}\right|^2. \quad \text{Eq. 4-6}$$

While many models empirically estimate T_{eff}^s using only soil surface and deep temperature (Chapter 2.3.3), the physical model (Choudhury et al., 1982) was adopted throughout this thesis to avoid errors induced by empirical parameters, such that

$$T_{\text{eff}}^s = \int_0^\infty T(z)\alpha(z)\exp\left[-\int_0^z \alpha(z')dz'\right]dz, \quad \text{Eq. 4-7}$$

where $T(z)$ is the soil temperature at depth z, and $\alpha(z)$ is the power absorption coefficient depending on the soil dielectric constant ε_r and the observation wavelength λ written as (Ulaby et al., 1986)

$$\alpha(z) = 2\cdot(2\pi/\lambda)\cdot\left|\text{Im}\left(\sqrt{\varepsilon_r(z)}\right)\right|, \quad \text{Eq. 4-8}$$

where Im ( ) represents the imaginary part. When estimating the effective soil temperature, the soil was modeled as a semi-infinite medium using the soil moisture and temperature observations from the hydra-probes of the station, with the soil moisture and temperature below the last observing layer assumed to be the same as those observed in the last observing layer.

4.2 Njoku Model

The Njoku model is a coherent model that is able to simulate the TB for a nonuniform soil, expressed as (Njoku and Kong, 1977, Schmugge and Choudhury, 1981)

$$\text{TB}_P = \int_0^\infty T(z)f_P(z)dz, \quad \text{Eq. 4-9}$$

where $T(z)$ is the soil temperature at depth z, and $f_P(z)$ is the fractional absorption which is calculated from the solution of a differential equation with a flux conservation boundary condition at the air/soil interface, such that

$$f_H(z) = \frac{k}{\cos(\theta)} \varepsilon_r''(z) |\psi(z)|^2 \quad \text{Eq. 4-10}$$

$$f_V(z) = \frac{1}{k\cos(\theta)} \varepsilon_r''(z) \left(\left| \frac{1}{\varepsilon_r(z)} \frac{d\phi(z)}{dz} \right|^2 + \left| \frac{k_x \phi(z)}{\varepsilon_r(z)} \right|^2 \right), \quad \text{Eq. 4-11}$$

where k is the free space wavenumber ($2\pi/\lambda$), $k_x = k\sin(\theta)$, and the functions $\psi(z)$ and $\phi(z)$ are determined from

$$\frac{d^2\psi(z)}{dz^2} + \left[\varepsilon_r(z)k^2 - {k_x}^2\right]\psi(z) = 0 \quad \text{Eq. 4-12}$$

$$\varepsilon_r(z) \frac{d}{dz} \left(\frac{1}{\varepsilon_r(z)} \frac{d\phi(z)}{dz} \right) + \left[\varepsilon_r(z)k^2 - {k_x}^2\right]\phi(z) = 0. \quad \text{Eq. 4-13}$$

The boundary conditions for a plane surface are

$$\frac{d\psi(z)}{dz} + ik\cos(\theta)\,[2 - \psi(z)] = 0 \quad \text{Eq. 4-14}$$

$$\frac{d\phi(z)}{dz} + i\,\varepsilon_r(z)\,k\cos(\theta)\,[2 - \phi(z)] = 0 \quad \text{Eq. 4-15}$$

for z= 0. Refer to Njoku (1976) and Njoku and Kong (1977) for more details on the mathematical derivation of the Njoku model.

4.3 I²EM

The emissivity of a soil surface can be calculated based on Kirchhoff's reciprocity theorem such that (Ulaby et al., 1982, Fung, 1994)

$$e_P = 1 - \Gamma_P = 1 - \Gamma_P^{\text{non}} - \Gamma_P^{\text{coh}}, \quad \text{Eq. 4-16}$$

where Γ_P^{non} and Γ_P^{coh} are the noncoherent and coherent soil surface reflectivity. Γ_P^{coh} can be calculated as

$$\Gamma_P^{\text{coh}} = \Gamma_P^* \exp\{-[2ks \cdot \cos(\theta)]^2\}, \quad \text{Eq. 4-17}$$

where k is the wave number, s is the RMS height of the soil surface, and Γ_P^* is the specular reflectivity calculated from the Fresnel equation (Eqs. 4-5 and 4-6).

The Γ_P^{non} can be obtained by integrating the bistatic scattering coefficient σ^s over the upper hemisphere

$$\Gamma_H^{\text{non}} = \frac{\int_0^{2\pi} \int_0^{\pi/2} [\sigma_{HH}^s(\theta,\phi,\theta_s,\phi_s) + \sigma_{HV}^s(\theta,\phi,\theta_s,\phi_s)] \sin(\theta_s) d\theta_s d\phi_s}{4\pi\cos(\theta)} \quad \text{Eq. 4-18}$$

$$\Gamma_V^{\text{non}} = \frac{\int_0^{2\pi}\int_0^{\pi/2}[\sigma_{VV}^S(\theta,\phi,\theta_s,\phi_s)+\sigma_{VH}^S(\theta,\phi,\theta_s,\phi_s)]\sin(\theta_s)d\theta_s d\phi_s}{4\pi\cos(\theta)}, \quad \text{Eq. 4-19}$$

where θ and ϕ are the zenith and azimuth of the incident direction, respectively, while θ_s and ϕ_s are the zenith and azimuth of the scattering direction, respectively. Moreover, σ_{PQ}^S (with P =H, Q =V or P =V, Q =H) was modeled by the I^{2}EM (Improved Integral Equation Model, Fung et al., 2002) in this thesis. It is a mathematically sophisticated computational algorithm for computing the bistatic scattering coefficient of a random surface, accounting for multiple scattering and shadowing effects. The I^{2}EM was compared with another descendant of the IEM (Fung et al., 1992, Fung, 1994), i.e., the Advanced IEM (AIEM, Chen et al., 2003), by Wu et al. (2008), showing that the I^{2}EM performed equally to or even better than the AIEM for low frequencies and small roughness, which is the case in this research. In addition, the I^{2}EM has been used in similar simulations of the emissivity of soil surfaces (e.g., Ulaby et al. 2014).

The main equation of the I^{2}EM used in this thesis is

$$\sigma_{PQ}^S = S(\theta,\theta_s)\frac{k^2}{2}$$
$$\cdot \exp[-s^2(k_z^2 + k_{sz}^2)]\sum_{n=1}^{\infty} s^{2n}\left|I_{PQ}^n\right|^2 \frac{W^{(n)}(k_{sx}-k_x,\ k_{sy}-k_y)}{n!}, \quad \text{Eq. 4-20}$$

where $S(\theta,\theta_s)$ is the bistatic shadowing function, $k_x = k\sin(\theta)\cos(\phi)$, $k_y = k\sin(\theta)\sin(\phi)$, $k_z = k\cos(\theta)$, with k_{sx}, k_{sy}, and k_{sz} similarly defined in terms of the scattering angles θ_s and ϕ_s, and $W^{(n)}$ is the Fourier transform of the n^{th} power of the surface correlation coefficient. Refer to Fung et al. (2002) for the full mathematical derivation of the I^{2}EM.

The inputs to the I^{2}EM are dielectric constant, observation frequency, and surface properties, including the type of correlation function, RMS height, and correlation length. An exponential correlation function was assumed in this thesis since soil surfaces are mostly considered exponential-like (Fung and Kuo, 2006, Schwank et al., 2009, Zhu et al., 2020).

The I²EM has also been employed to simulate the emissivity of furrowed sinusoidal soil surfaces. A one-dimensional sinusoidal surface with height $Z(y)$ can be described by

$$Z(y) = \mathrm{A}\left[1 + \cos\left(\frac{2\pi y}{\Lambda}\right)\right], \qquad \text{Eq. 4-21}$$

with amplitude A and spatial period Λ. Assuming that there are many spatial periods Λ within the antenna footprint, the emissivity of this sinusoidal surface ($e_P^{\sin}$) can be integrated across a single period such that (Ulaby et al., 2014)

$$e_P^{\sin}(\phi) = \frac{1}{\Lambda\cos(\theta)}\int_0^{\Lambda} e_P \sec(\alpha)\cos(\theta')\,dy, \qquad \text{Eq. 4-22}$$

where e_P is the emissivity of the local small-scale surface with local incidence angle θ' calculated using Eq. 4-16, and α is the angle whose tangent is equal to the slope of the surface $Z(y)$. Please refer to Ulaby et al. (2014) for more details on this model. Apart from the regular inputs of the I²EM model, additional input requirements include azimuth, amplitude, and period of the sinusoidal surface.

4.4 Mironov Model

Throughout this thesis, the dielectric constant was related to soil moisture using the model of Mironov et al. (2013b) because it accounts for the interfacial (Maxwell-Wagner) relaxation of water in the soil, which is essential at P-band (Chen and Or, 2006). While the Peplinski model is also applicable at P-band (Peplinski et al., 1995b), Mironov et al. (2013b) reported that the Peplinski model had a much larger standard deviation from dielectric measurements (~0.3 compared to 0.014 using the Mironov model) and was thus not adopted in this thesis.

The real (ε'_m) and imaginary (ε''_m) parts of the complex dielectric constant of moist soils can be represented in the form of the refractive mixing dielectric model as (Mironov et al., 2004)

$$\varepsilon'_m = n_m^2 - \kappa_m^2 \qquad \text{Eq. 4-23}$$

$$\varepsilon''_m = 2n_m\kappa_m \qquad \text{Eq. 4-24}$$

$$n_m = \begin{cases} n_d + (n_b - 1)\mathrm{SM}, \mathrm{SM} \le \mathrm{SM}_t \\ n_d + (n_b - 1)\mathrm{SM}_t + (n_u - 1)(\mathrm{SM} - \mathrm{SM}_t), \mathrm{SM} \ge \mathrm{SM}_t \end{cases} \quad \text{Eq. 4-25}$$

$$\kappa_m = \begin{cases} \kappa_d + \kappa_b \mathrm{SM}, \mathrm{SM} \le \mathrm{SM}_t \\ \kappa_d + \kappa_b \mathrm{SM}_t + \kappa_u(\mathrm{SM} - \mathrm{SM}_t), \mathrm{SM} \ge \mathrm{SM}_t \end{cases} \quad \text{Eq. 4-26}$$

where SM and SM_t are the volumetric soil moisture and the maximum bound water fraction of the soil, respectively, and n_i and κ_i are the refractive index and normalized attenuation coefficient, respectively, with the subscript i being m (moist soil), d (dry soil), b (bound soil water), or u (unbound or free water in the soil).

According to Mironov et al. (2013b), the n_i and κ_i can be expressed as

$$n_i\sqrt{2} = \sqrt{\sqrt{(\varepsilon_i')^2 + (\varepsilon_i'')^2} + \varepsilon_i'} \quad \text{Eq. 4-27}$$

$$\kappa_i\sqrt{2} = \sqrt{\sqrt{(\varepsilon_i')^2 + (\varepsilon_i'')^2} - \varepsilon_i'}. \quad \text{Eq. 4-28}$$

The two-relaxation Debye equations define the dielectric constant of the bound soil water as

$$\varepsilon_b' = \frac{\varepsilon_{0bI} - \varepsilon_{0bD}}{1 + (2\pi f \tau_{bI})^2} + \frac{\varepsilon_{0bD} - \varepsilon_{\infty bD}}{1 + (2\pi f \tau_{bD})^2} + \varepsilon_{\infty bD} \quad \text{Eq. 4-29}$$

$$\varepsilon_b'' = \frac{\varepsilon_{0bI} - \varepsilon_{0bD}}{1 + (2\pi f \tau_{bI})^2} 2\pi f \tau_{bI} + \frac{\varepsilon_{0bD} - \varepsilon_{\infty bD}}{1 + (2\pi f \tau_{bD})^2} 2\pi f \tau_{bD} + \frac{\sigma_b}{2\pi \varepsilon_v f}, \quad \text{Eq. 4-30}$$

where ε_{0ij} and $\varepsilon_{\infty ij}$ are the dielectric constants in the low- and high-frequency limits, respectively, with the subscript j being either I (ionic relaxation) or D (dipole relaxation), τ_{ij} denotes the relaxation time, σ_i denotes the ohmic conductivity, and ε_v is the dielectric constant of vacuum, being $8.854 \cdot 10^{-12}$ F/m. For the free soil water that possesses only dipole relaxation, $\varepsilon_{0iI} = \varepsilon_{0iD}$ can be obtained, and thus Eqs. 4-29 and 4-30 can be simplified to

$$\varepsilon_u' = \frac{\varepsilon_{0uD} - \varepsilon_{\infty uD}}{1 + (2\pi f \tau_{uD})^2} + \varepsilon_{\infty uD} \quad \text{Eq. 4-31}$$

$$\varepsilon_u'' = \frac{\varepsilon_{0uD} - \varepsilon_{\infty uD}}{1 + (2\pi f \tau_{uD})^2} 2\pi f \tau_{uD} + \frac{\sigma_u}{2\pi \varepsilon_v f}. \quad \text{Eq. 4-32}$$

Based upon the model in Mironov et al. (2013b) and the dielectric measurements of a range of soil samples in the frequency range 0.04 to 26.5 GHz, Mironov et al. (2014) developed a relationship between soil properties (i.e., clay content and bulk density)

Table 4-1: Parameters used in the Mironov model (Eqs. 4-23-4-32) according to Mironov et al. (2014).

Parameter	Value
n_d	$1+(0.432-0.065C)\rho_b$
κ_d	$(0.008+0.011C)\rho_b$
ε_{0bI}	$761-840C$
ε_{0bD}	$27.18+61\cdot\exp(-C/0.287)$
$\varepsilon_{\infty bD}$	4.9
ε_{0uD}	100
$\varepsilon_{\infty uD}$	4.9
τ_{bI}	2.5×10^{-9} s
τ_{bD}	1.25×10^{-11} s
τ_{uD}	1.06×10^{-11} s
σ_b	0.001 S/m
σ_u	$0.097+0.69C$ S/m
SM_t	$0.024+0.339C$ m^3/m^3

The C is clay content in percentage, and ρ_b is soil bulk density in g/cm^3.

and the spectroscopic parameters in the model. Table 4-1 shows the parameter values used to compute the dielectric constant throughout this thesis. These parameters were calibrated at 20 ℃, indicating that this model implicitly assumes a constant temperature of 20 ℃. As a result, the impact of temperature variations on dielectric constant was neglected in this thesis. The clay content (C =18%) and bulk density (ρ_b=0.87 g/cm^3) measured in the field (Table 3-3) were used in the Mironov model.

4.5 Chapter Summary

This chapter introduced the models used in the following chapters. Chapter 5 uses the Njoku model to estimate the moisture retrieval depth at P- and L-band. Chapter 6 adopts the I^{2}EM for simulating the emissivity of flat and periodic soil surfaces. Since only the tau-omega model can account for the vegetation effects, it was applied to the analysis in Chapters 7 and 8 that dealt with vegetation-covered soil. The Mironov model was used throughout this thesis to link dielectric constant to soil moisture.

5 Soil Moisture Retrieval Depth

Chapters 3 and 4 have introduced the data and models used throughout this thesis, respectively, and so the analysis starts from this chapter onward. As discussed in Chapter 2.3.2, the moisture retrieval depth is of more relevance than the thermal sensing depth because it indicates the representative soil thickness of the soil moisture data. Accordingly, this chapter developed a theoretical model for moisture retrieval depth based upon the Njoku and Fresnel models introduced in Chapter 4 and empirically correlated the radiometer and soil moisture measurements presented in Chapter 3. The estimated moisture retrieval depth at P- and L-band was used in the following chapters for simulating TB and evaluating retrieved soil moisture. The work in this chapter has been published in Shen et al. (2021).

5.1 Background

Moisture retrieval depth can be determined only by model estimation rather than by direct measurement, and so it is subject to the retrieval model used. Therefore, the use of the term "moisture sensing depth" is considered inappropriate as it can be easily misinterpreted as an indicator of the sensing capability of the instrument. The fact is that it can only be determined by model estimation and not by direct measurement. More correctly, "moisture retrieval depth" is used instead hereafter in this thesis.

The SMOS and SMAP missions can only provide moisture information within the top 5-cm layer of soil or less (Entekhabi et al., 2010, Kerr et al., 2010) due to the limited moisture retrieval depth of L-band, hindering the widespread application of soil moisture products in hydrology, agriculture, and climate research. While moisture retrieval depth ranges from approximately one-tenth to one-fourth of the wavelength (Wilheit, 1978, Schmugge and Choudhury, 1981, Newton et al., 1982, Newton et al., 1983, Ulaby et al., 1986, Raju et al., 1995), until now it has not been demonstrated to be actually greater at P- than L-band due to the lack of coincident radiometer

observations at these wavelengths. Moreover, there is no accepted model for predicting the moisture retrieval depth at different wavelengths.

This chapter developed a theoretical model for moisture retrieval depth based upon the Njoku and Fresnel models introduced in Chapter 4 and compared the moisture retrieval depth from P- and L-band radiometry to understand the potential increase at P-band under a range of moisture profiles. Furthermore, the radiometer and soil moisture measurements collected over the bare soil at the PRISM tower site (Chapter 3) were empirically correlated to estimate the moisture retrieval depth from an observation perspective.

5.2 Data

Figure 5-1 shows the ground-based measurements from the PRISM tower experiment (see Chapter 3) that were used for the empirical correlation analysis. During the study period shown in Figure 5-1, the field with four quadrants was maintained as flat bare ground (Figure 3-2c) with dynamic moisture conditions. To minimize the presence of

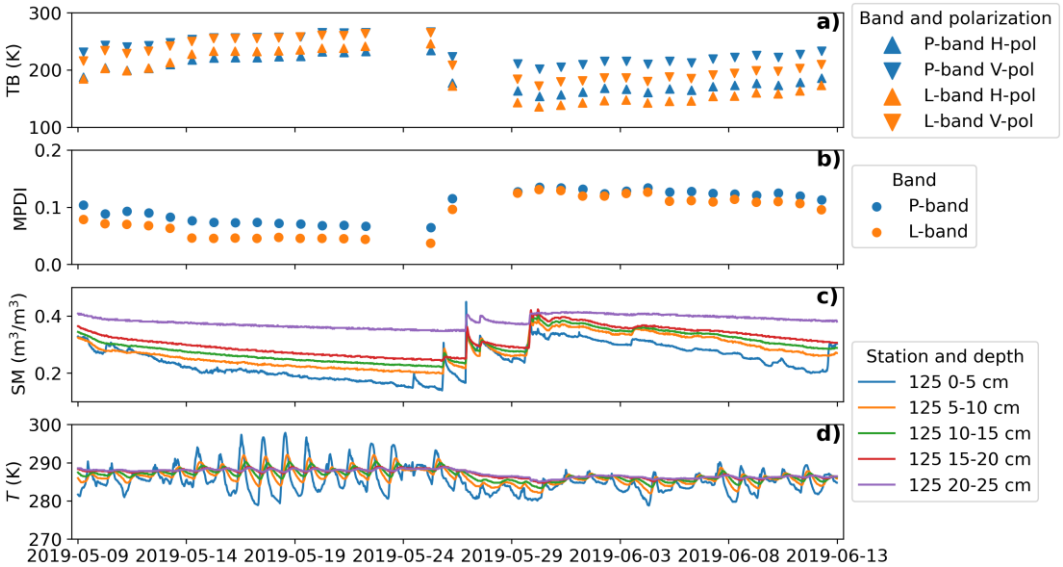

Figure 5-1: Collected data include a) TB observations at 30° incidence angle, b) calculated MPDI from TB, c) time-series soil moisture and d) temperature from station 125. The data gaps in a) and b) resulted from the tower being lowered due to high wind on those days.

weeds, the experiment site was freshly plowed on May 7, 2019. Since the four quadrants had the same field conditions, only the TB observations collected in Q4 were analyzed in this chapter. Although the TB observations at around 40° incidence angle are preferable to be analyzed, as discussed in Chapter 3.3, those at 30° were used instead due to the unavailability of the 40° data during the study period of this chapter. The MPDI was calculated from the TB measurements using Eq. 2-10 (Figure 5-1b). During the study period, all stations were removed due to cultivation activities, with only the temporary station 125 operating. Accordingly, the soil moisture and temperature measured by the five hydra-probes of station 125 are plotted in Figure 5-1c and d, respectively.

5.3 Method

5.3.1 Radiative transfer theory

For an ideal soil with uniform moisture and temperature profiles, the well-known radiative transfer approximation can be used to estimate the emissivity from TB measurements (Ulaby et al., 1986)

$$\mathrm{TB}_P = e_P T. \qquad \text{Eq. 5-1}$$

For real soils, moisture and temperature vary vertically due to solar radiation, precipitation, infiltration, and gravity, so are by no means uniform. In this case, the coherent model (e.g., the Njoku model introduced in Chapter 4.2) is able to simulate the TB of a nonuniform soil. In order to apply the radiative transfer approximation to soils with nonuniform temperature, the so-called effective soil temperature was proposed to substitute the physical temperature in Eq. 5-1. The theoretical form of effective soil temperature can be expressed as (Schmugge and Choudhury, 1981)

$$T_{\mathrm{eff}}^{s} = \frac{\int_0^\infty T(z) f(z) dz}{\int_0^\infty f(z) dz}, \qquad \text{Eq. 5-2}$$

where $f(z)$ is the fractional absorption calculated from the coherent model. Thus, with known TB_P and $T{=}T_{\mathrm{eff}}^{s}$, e_P can be obtained from Eq. 5-1. However, the question

of what representative depth of soil over which the emissivity (i.e., dielectric constant and thus moisture) is estimated remains.

5.3.2 Moisture retrieval depth model

To quantify the above-mentioned representative depth, the moisture retrieval depth (δ_m) is defined as the equivalent soil thickness [0, z] for obtaining the average soil moisture that equates the emissivity through the Fresnel equations (hereafter referred to as the Fresnel emissivity) to the theoretical emissivity from the coherent model (hereafter referred to as the coherent emissivity). The mathematical explanations are as follows.

Equating the Njoku model (Eq. 4-9) and the radiative transfer approximation (Eq. 5-1) and substituting the theoretical form of effective soil temperature (Eq. 5-2), one obtains

$$e^*[\mathrm{SM}(0-\delta_m)] = \int_0^\infty f(z)dz, \qquad \text{Eq. 5-3}$$

where $\mathrm{SM}(0-\delta_m)$ is the soil moisture averaged over the 0-δ_m layer, $e^*[\mathrm{SM}(0-\delta_m)]$ denotes the Fresnel emissivity determined by $\mathrm{SM}(0-\delta_m)$ that is calculated from Eqs. 4-2, 4-5, and 4-6, and $\int_0^\infty f(z)dz$ is the coherent emissivity computed from Eqs. 4-10 and 4-11. Eq. 5-3 can therefore be used to determine the soil thickness whose averaged soil moisture produces a Fresnel emissivity that equals the coherent emissivity.

To account for the roughness of natural soil surfaces, the widely used HQN model (Eq. 2-5) was adopted, such that

$$e = 1-(1-e^*)\exp[-H_R\cos^{N_{RP}}(\theta)] \qquad \text{Eq. 5-4}$$

for low frequencies, i.e., P- and L-band, with Q_R assumed to be 0. Substituting the Fresnel and coherent emissivity in Eq. 5-3 with e demonstrates that roughness has no impact on moisture retrieval depth according to this model, and thus roughness effects were not considered in this model. Accordingly, the required inputs of this moisture

retrieval depth model are therefore the soil moisture profile, soil properties (clay content and bulk density), observation frequency, and incidence angle.

5.3.3 Moisture retrieval depth prediction

Eq. 5-3 was used to predict the moisture retrieval depth using the Njoku model (see Chapter 4.2) for six typical soil moisture profiles $\mathrm{SM}(z)$ (Figure 5-2). Profile depth and layer thickness of all six profiles were assumed to be 10 m (i.e., $z < 10$ m) and 0.1 mm, respectively, to avoid any possible boundary or numerical approximation artefacts.

Profiles 1-5 were simulated using the functions from Njoku and Kong (1977) being

$$\mathrm{SM}(z) = \mathrm{SM}_s + \Delta\mathrm{SM}\frac{e^{-\beta z}-1}{e^{-\beta d}-1} \quad 0 \le z \le d \qquad \text{Eq. 5-5}$$

$$\mathrm{SM}(z) = \mathrm{SM}(d) \quad z \ge d, \qquad \text{Eq. 5-6}$$

and the parameters listed in Table 5-1, where SM_s is the moisture content at the soil surface, $\Delta\mathrm{SM}$ is the increment of moisture between the surface and depth d below the surface, beyond which the moisture content was assumed to be constant, and β determines the moisture gradient of the profile.

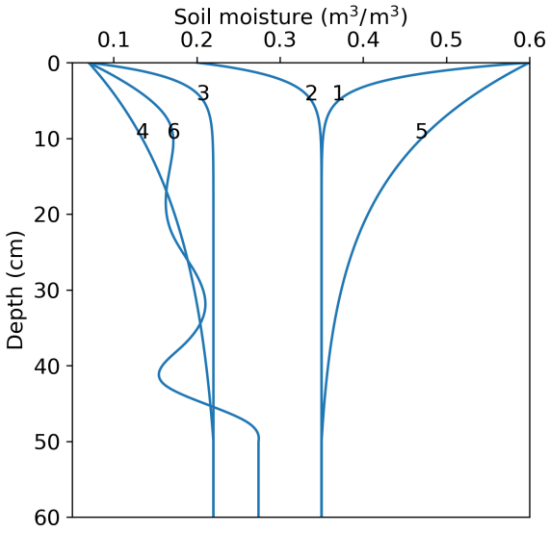

Figure 5-2: Simulated typical soil moisture profiles with constant moisture assumed below 50 cm.

Table 5-1: Parameters characterizing the moisture profiles plotted in Figure 5-2.

Profile	SM_s (m^3/m^3)	ΔSM (m^3/m^3)	β (cm^{-1})	d (cm)	Moisture gradient over 0-10-cm layer (cm^{-1})	Moisture gradient over 10-20-cm layer (cm^{-1})
1	60	-25	0.5	50	0.025	0
2	20	15	0.5	50	0.015	0
3	7	15	0.5	50	0.015	0
4	7	15	0.05	50	0.006	0.004
5	60	-25	0.07	50	0.013	0.006
6	–	–	–	–	0.010	0.001

Profiles 1 and 5 may both occur during rain but with different rainfall amounts, duration, and intensity. Profiles 2-4 simulated drying profiles. Profiles 2 and 3 had the same moisture gradient near the surface but different profile moisture, while profile 4 had a smaller surface moisture gradient. Differing from profiles 1-5, profile 6 represented the actual moisture profile observed at the experiment site, generated by interpolating the soil moisture measurements at different depths from the station.

5.4 Results and Discussion

5.4.1 Predicted moisture retrieval depth

Prior to the estimation of the moisture retrieval depth, the complex relative dielectric constant and emissivity were compared for P- and L-band in Figure 5-3. It can be seen that the real components of the dielectric constant were basically the same across soil moisture at P- and L-band whereas P-band had a slightly larger imaginary component than L-band, in line with the literature (Hoekstra and Delaney, 1974, Wagner et al., 2011). The slight difference in dielectric constant resulted in a small unapparent offset in emissivity at P- and L-band, particularly when soil moisture was less than 0.3 m^3/m^3.

Figure 5-4 depicts the estimated coherent and Fresnel emissivity across soil thickness corresponding to the moisture profiles 1-6 of Figure 5-2 at 30° incidence angle and H

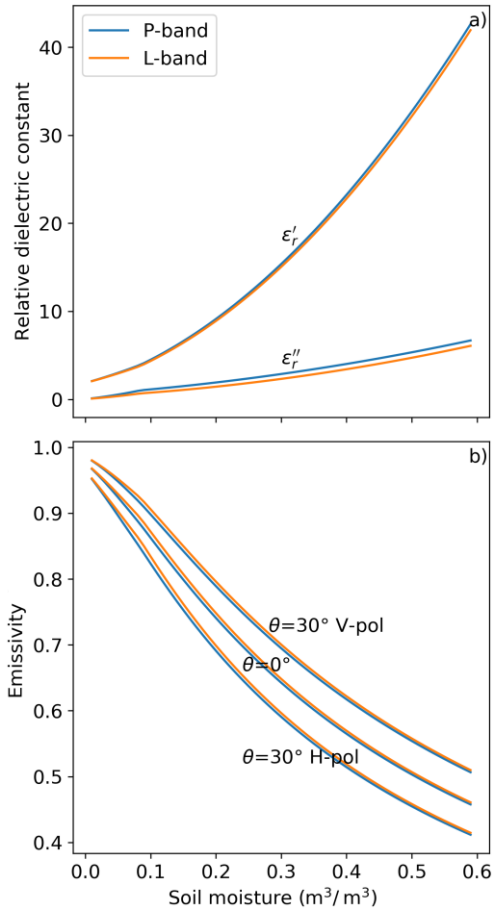

Figure 5-3: Comparison of P- and L-band a) relative dielectric constant and b) emissivity across soil moisture. The emissivity was predicted by both the Fresnel and coherent model and found to be the same for this scenario of an assumed uniform moisture profile.

polarization. The 30° incidence angle was adopted herein for consistency with the TB observations used for calculating the observed moisture retrieval depth. The impact of soil texture on moisture retrieval depth was also tested by assuming a clay content of 50% instead of 18% with a difference of not more than 1 cm between the two results.

By definition, the simulated coherent emissivity for each profile is a single value and thus plotted in Figure 5-4 as the solid horizontal line. The Fresnel emissivity was calculated using the averaged soil moisture over an increasing soil thickness, shown as the dashed curve. The moisture retrieval depth for P- and L-band is thus indicated by

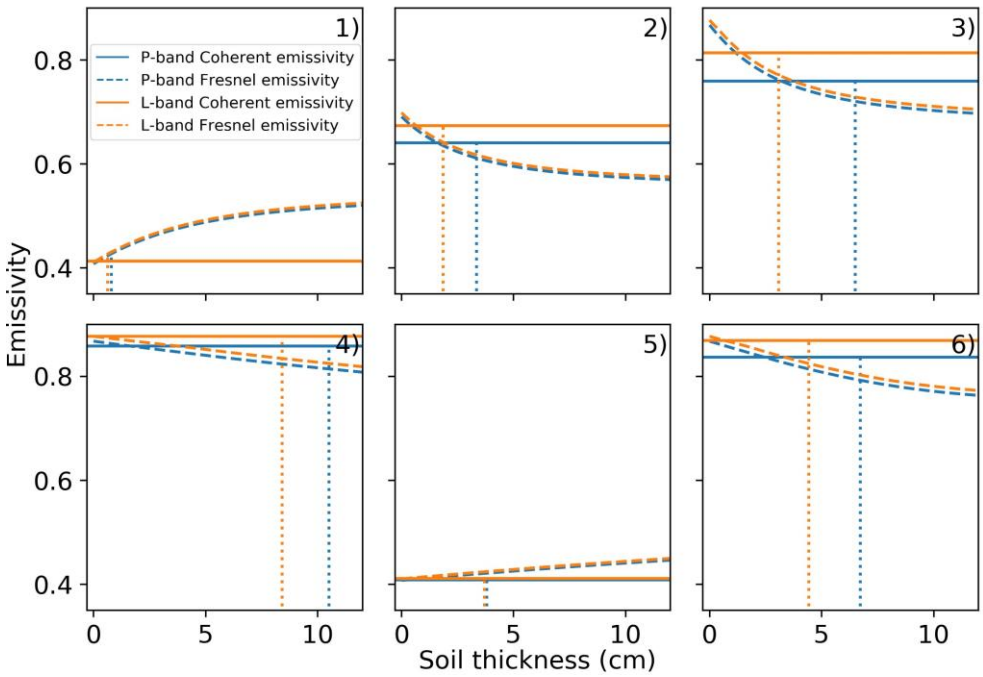

Figure 5-4: Coherent and Fresnel emissivity at 30° incidence angle and H-pol across soil thickness and moisture retrieval depth indicated by vertical dotted lines. Subplots 1-6 correspond to soil moisture profiles 1-6. In subplots 1 and 5, P- and L-band are very close to being overlapped.

the intersection of the two models. However, this theoretical retrieval depth is subject to uncertainties.

To account for uncertainties, the moisture retrieval depth was calculated as the vertical dotted lines shown in Figure 5-4. One major uncertainty source is considered to be the dielectric model because most dielectric models are semiempirical. A comprehensive evaluation of nine commonly used dielectric models by Park et al. (2019) found an average median absolute bias of around 0.03 m^3/m^3 when compared with measurements. Accordingly, the potential bias in emissivity can be estimated depending on the soil moisture and frequency. Moreover, in a practical sense, soil is a continuous medium, and thus high correlation exists between the soil moisture of neighboring layers, potentially enlarging the moisture retrieval depth further. Therefore, the moisture retrieval depth was increased to the point where the difference between

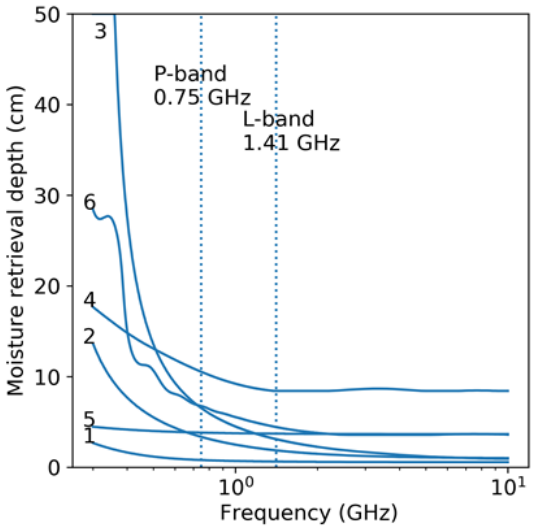

Figure 5-5: Moisture retrieval depth at 30° incidence angle and H-pol against frequency from 0.3 to 10 GHz, corresponding to soil moisture profiles 1-6.

the Fresnel and coherent emissivity was equal to the above-mentioned bias in emissivity.

The calculated moisture retrieval depths in Figure 5-4 ranged within 0.8-10.5 and 0.6-8.4 cm for P- and L-band at 30° incidence angle, respectively. Overall, a larger moisture retrieval depth at P-band than L-band can be observed for all profiles, especially profiles 2, 3, 4, and 6. However, P- and L-band did not substantially differ for profiles 1 and 5 due to the extremely high surface soil moisture.

Figure 5-5 demonstrates that, overall, the moisture retrieval depth increased with wavelength, notably when the frequency dropped below 1 GHz, though minimally for profiles 1 and 5 due to the extremely high surface soil moisture. The moisture retrieval depth of profile 6 had some "waves" across frequency due to the irregular fluctuation of soil moisture with depth.

Figure 5-5 also shows that the soil moisture, especially the surface soil moisture relative to the profile soil moisture, had the primary impact on determining the moisture retrieval depth, e.g., a sequence of moisture retrieval depth from large to small was profiles 3, 2 and 1, corresponding to the surface soil moisture from low to high.

Previous empirical studies have also observed this frequency and moisture dependence of moisture retrieval depth at L-band (Wilheit, 1978, Escorihuela et al., 2010). However, this cannot explain why profile 5 achieved a larger moisture retrieval depth than profile 1, even though it had higher surface and subsurface moisture. It is therefore reasonable to infer that the moisture gradient was another primary factor that dominated moisture retrieval depth.

It is hypothesized that the lower surface moisture gradient in the 0-10-cm layer of 0.013 cm^{-1} contributed to the deeper moisture retrieval depth of profile 5, compared to profile 1 whose surface moisture gradient was 0.025 cm^{-1} (Table 5-1), because a lower gradient usually means a higher correlation between the moisture of neighboring soil layers. Moreover, it was observed that the moisture gradient in the 10-20-cm layer affected the moisture retrieval depth. Profiles 2 and 3 had a large surface moisture gradient of 0.015 cm^{-1} but were then uniform below 10 cm, which explains why in Figure 5-5 for decreasing frequency the moisture retrieval depth increased slowly at first and then quickly below 0.5 GHz for these profiles. For the continuously changing profiles 4 and 5, the moisture retrieval depth did not change much over frequency. Therefore, P-band tended to have a substantially larger moisture retrieval depth than L-band only if the moisture profile was steep at the surface and then uniform for deeper depths, with dry-to-intermediate soil moisture (e.g., profile 3). Otherwise, P- and L-band had a similar moisture retrieval depth (e.g., profiles 4 and 5).

5.4.2 Observed moisture retrieval depth

Figure 5-6 shows the correlation of MPDI against the soil moisture measurements averaged over different soil thicknesses for P- and L-band. MPDI was used instead of TB to exclude the impact of diurnal or day-to-day variations in soil temperature on TB, and thus be more highly related to the dielectric properties (i.e., moisture) of the soil (Owe et al., 2001). It can be observed that the correlation was highest for the 0-5-cm thickness and decreased with increasing soil thickness. This result can be interpreted in one of two ways: 1) for the same moisture retrieval depth (~5 cm) a greater correlation (accuracy of retrieval) can be achieved at P-band than at L-band or 2) a

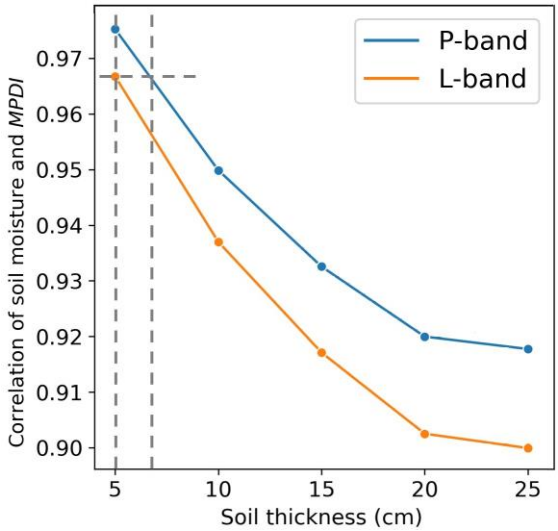

Figure 5-6: Correlation of MPDI against soil moisture averaged over different soil thicknesses for bare soil observations from May 9 to June 12, 2019.

larger moisture retrieval depth can be achieved at P-band (~7 cm) than at L-band (~5 cm) for the same correlation (accuracy of retrieval), confirming the prediction result for profile 6 in Figure 5-4. Importantly, these empirical results were limited to the specific moisture conditions, soil properties, and incidence angle used at the Cora Lynn site.

5.5 Chapter Summary

This chapter compared the moisture retrieval depth of P- and L-band radiometry from prediction and observation perspectives. For the same moisture retrieval depth, a higher correlation between soil moisture and MPDI was found at P-band than L-band, implying that P-band can either retrieve soil moisture over the same moisture retrieval depth as L-band (~5 cm) but with greater accuracy, or that a larger moisture retrieval depth (~7 cm) can be achieved while maintaining the same accuracy. These empirical results agreed with model predictions. Moreover, model predictions showed that the moisture retrieval depth increased with wavelength such that P-band can potentially provide soil moisture retrievals for a depth greater than 10 cm when using a frequency lower than 0.5 GHz. However, it was found that the moisture retrieval depth achieved depended on the moisture gradient of the profile in addition to the soil moisture

content and observation frequency. Although the moisture retrieval model proposed in this chapter has the potential to be applied to the time-series observations from the station, it will introduce many uncertainties to the results when interpolating soil moisture measurements at a 5-cm interval into continuous profiles, particularly for the top 2.5-cm layer which lacks direct observation.

Although P-band has been demonstrated to have a larger moisture retrieval depth (~7 cm) than L-band (~5 cm), the 0-5-cm soil moisture observations were used in the following chapters due to the lack of a soil moisture observation in the 0-7-cm layer and that the soil moisture was highly correlated between the 0-5-cm and 5-10-cm layers. Moreover, the moisture retrieval depth at P-band reduced to approximately 5 cm when the wheat (Chapter 7) and corn (Chapter 8) were present.

6 Roughness Impact of Random and Periodic Surfaces

Chapter 5 demonstrated the greater moisture retrieval depth at P- than L-band. This chapter investigates the impact of random and periodic surface roughness on P- and L-band radiometry. The I^2EM introduced in Chapter 4.3 was adopted to physically simulate the emission of bare random and periodic soil surfaces at P- and L-band. In addition, the semi-empirical model for bare soil (Eq. 4-4) was applied to calibrate roughness parameters and retrieve soil moisture. The calibrated roughness parameters were used in the following chapters. The work in this chapter has been published partly in Shen et al. (2022a) and Shen et al. (2022b).

6.1 Background

As discussed in Chapter 2.3.4, soil roughness is well known to complicate the interpretation of microwave radiometer data and reduce the sensitivity of TB to soil moisture (Choudhury et al., 1979, Newton and Rouse, 1980). In addition, roughness has been found to impact microwave radiometry by reducing polarization difference, i.e., the depolarization effect (Shi et al., 2002, Mialon et al., 2012). As a result, Wang and Choudhury (1981) developed the HQN model to simulate the random roughness impact, which is currently being used in the SMOS (Kerr et al., 2019) and SMAP (O'Neill et al., 2021a) algorithms.

The Fraunhofer criterion claims that a surface may be considered electromagnetically smooth in the microwave range if the RMS height s is less than $\lambda/(32\cos(\theta))$ (Ulaby et al., 1982), asserting that observations at longer wavelength should be less affected by soil roughness than those at shorter wavelength. However, observational evidence at P-band is lacking.

Compared to flat soil, periodic (e.g., sinusoidal) row structures, a common type of soil tillage used for cultivation purposes, often affect soil emission to a substantial degree (Ulaby et al., 1986). A common modeling approach is to simulate the micro-scale roughness and assume that the macro-scale roughness acts like topography by changing the local incidence angle of the micro-scale roughness (Wang et al., 1980, Ulaby et al., 2014, Neelam et al., 2020).

The current SMOS and SMAP SCA algorithms assume constant roughness parameters of the HQN model for different land cover types (Entekhabi et al., 2014, Kerr et al., 2017). Additionally, the impact of periodic soil surfaces has not been considered due to difficulties such as the lack of a global map for row structure, row height, and orientation. Moreover, there is currently no basis for how to upscale such field information to satellite footprint scales. Since these assumptions and simplifications impose errors on the soil moisture datasets (Peng et al., 2017a), retrieval accuracy can be improved if a P-band radiometer is used on the satellite platform even if ignoring periodic structures, if it can be proven that the roughness effects are reduced from those at L-band. Furthermore, the calibration results could be taken advantage of to improve retrieval accuracy over periodic soil surfaces over an aircraft-based radiometer platform. Consequently, this chapter investigated whether P-band has a reduced roughness impact compared to L-band using the PRISM tower-based dataset for the bare soil surfaces with different roughness configurations (Chapter 3).

6.2 Data

The data collected in all four quadrants from July 17, 2019 to July 31, 2019 were used in this chapter (see Chapter 3). Because the field was plowed and sown with wheat in late July, only a limited period of data could be used for the study of bare soil. During this period, quadrants 1-4 were all bare soil and managed with different roughness conditions (Figure 6-1). Quadrant 2 was smooth flat soil while quadrants 1, 3, and 4 had periodic row structures with different shapes and/or azimuth. Azimuth is defined here as the angle between the radiometer look direction and the row direction. The

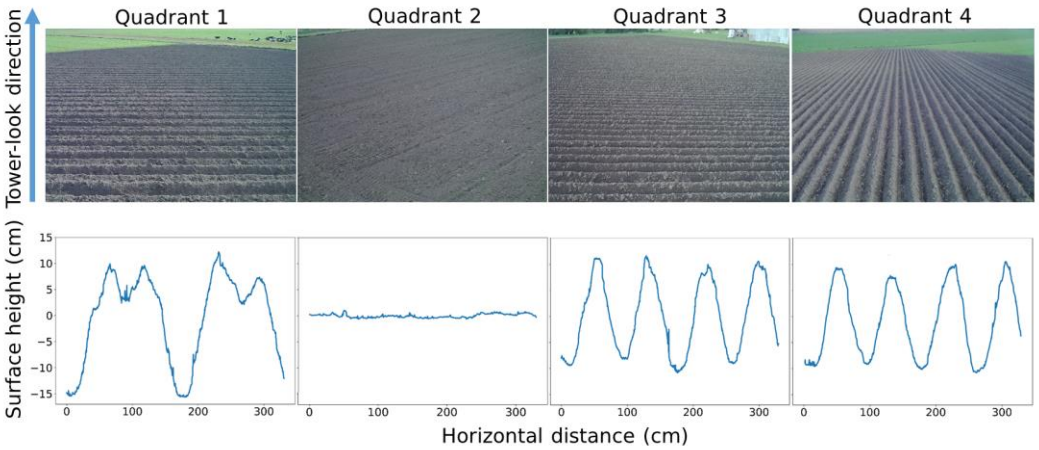

Figure 6-1: Photos of the roughness conditions (top row) and soil profiles (bottom row) of the four quadrants. Quadrants 3 and 4 were plowed in one pass and had the same roughness structures but with different orientations (perpendicular and parallel, respectively) relative to the tower look direction.

period of the row structure is defined as the row spacing, while the amplitude is half of the vertical distance between the bottom and the top of the row.

The roughness measurements in Table 6-1 were performed on July 17 and 31, 2019 for quadrants 1-4. In total, four profiles were measured for each of the quadrants. The

Table 6-1: Characterization of the roughness structures in the four quadrants.

Quadrant	Row structure	Periodic roughness			Random roughness	
		Azimuth (°)	Period (cm)	Amplitude (cm)	RMS height (cm)	Correlation length (cm)
1	Sinusoidal bench	90	165	12	1.3 ± 0.2	5.4 ± 1.9
2	Flat	–	–	–	0.8 ± 0.3	11.1 ± 4.4
3	Sinusoidal	90	80	10	1.1 ± 0.3	5.5 ± 1.3
4	Sinusoidal	0				

The measurements in Q1, Q3, and Q4 were decomposed into periodic and random components for calculating the periodic and random roughness statistics, respectively. Quadrants 3 and 4 were plowed in one pass and had the same roughness structure (just different orientations relative to the tower look direction), and therefore the measurements in these two quadrants were averaged.

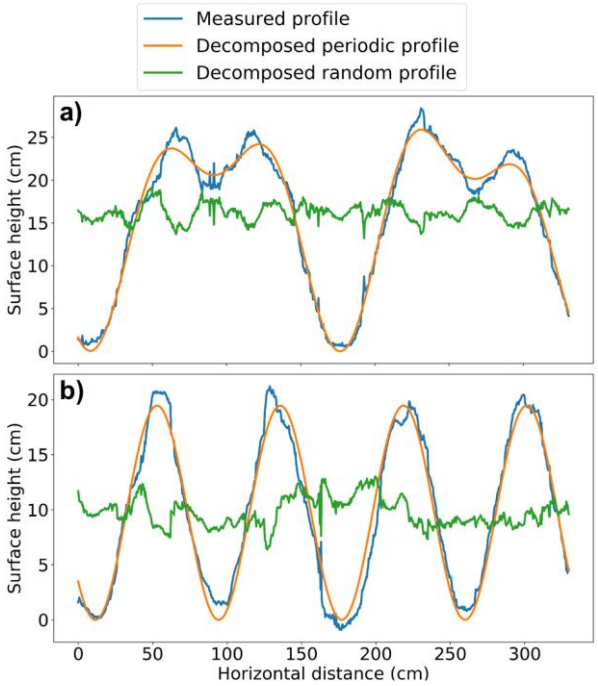

Figure 6-2: Decomposition of measured roughness profile into periodic and random profiles, for a) the sinusoidal bench profile of quadrant 1 and b) the sinusoidal profile of quadrants 3 and 4.

measurements were performed across and along the rows for the periodic surfaces. The profiles measured across the rows were decomposed into random (micro-scale) and periodic (macro-scale) components (Figure 6-2). The periodic components (in orange in Figure 6-2) of the profiles in quadrant 1 as well as quadrants 3 and 4 were approximated using two-term and one-term sinusoidal functions, respectively. The fitting residuals (in green in Figure 6-2) were taken as the random roughness component across the rows. The RMS height and correlation length in all four quadrants were calculated and averaged (with standard deviation) from using the random roughness components in the two perpendicular directions (Table 6-1). The roughness properties did not change much during the observing period, as indicated by the small standard deviation in Table 6-1, making it fair to assume a constant roughness condition over the analysis period. Consequently, the time-average of the RMS height and correlation length measurements was used in this chapter.

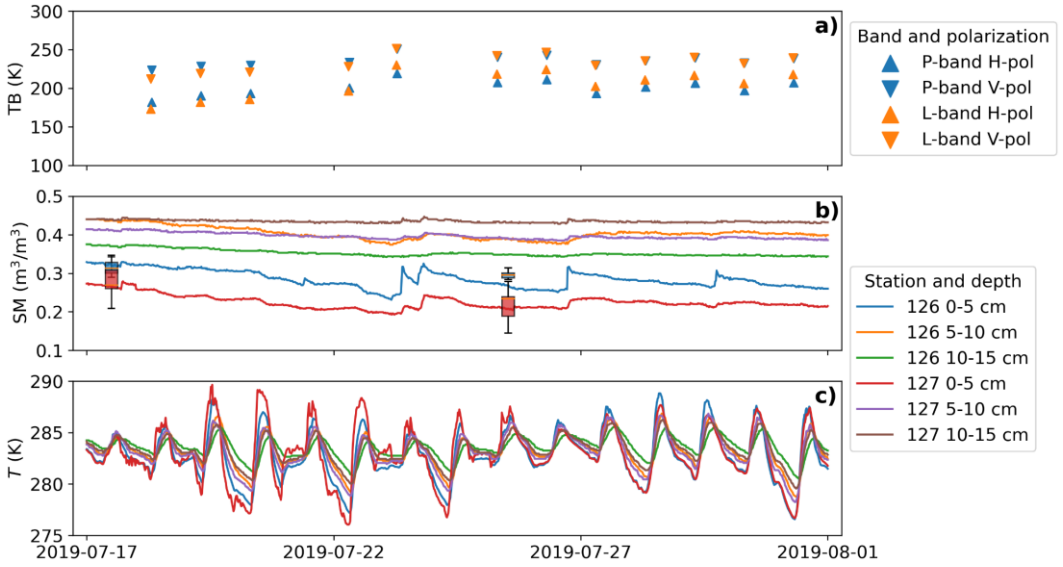

Figure 6-3: Collected data including a) TB observations at 6 am in quadrant 1 as an example; b) station time-series soil moisture with weekly HDAS measurements (boxplots) on two occasions; and c) station time-series soil temperature. The data gaps in a) resulted from the tower being lowered due to high wind on those days. Only the data collected from the top 3 of the 12 sensors are plotted in b) and c). Corresponding to the soil moisture evolutions of station 126 (in blue) for quadrant 2 and station 127 (in red) for quadrants 1, 3, and 4, the HDAS measurements in quadrant 2, and quadrants 1, 3, and 4, are plotted as the blue and red boxplots in b), respectively, showing the maximum, 75% percentile, median, 25% percentile, and minimum.

Figure 6-3 presents the collected data during the study period. The TB data at 38° for L-band and 40° for P-band collected at around 6 am were plotted and used in this chapter (Fig. 4a). The time series of soil moisture and temperature collected from stations 126 and 127 is plotted in Figure 6-3b and c. Stations 126 and 127 showed similar soil moisture evolution over time, but with higher near-surface soil moisture values at station 126. The reason for this offset is that station 126 was in the flat quadrant, while station 127 was in the furrowed quadrant (Figure 3-1a, Figure 3-2d, and Figure 6-1); the drier moisture condition in the furrowed quadrants was also supported by the HDAS measurements shown in Figure 6-3b. Considering the HDAS measurement agreement with the station soil moisture in the flat and periodic quadrants, in this chapter station 126 was used as the soil moisture reference for

quadrant 2 and station 127 was used as the soil moisture reference for quadrants 1, 3, and 4. As stated in Chapter 5.5, the time-averaged soil moisture at around 6 am in the 0-5-cm layer was used to evaluate the retrieved soil moisture at P- and L-band.

6.3 Method

Theoretical models were first applied to compare the roughness impact at P- and L-band, including the Fraunhofer criterion (Ulaby et al., 1982) and the I^{2}EM for random and sinusoidal surfaces (see Chapter 4.3). Moreover, the magnitude of the depolarization effect was calculated as

$$\Delta\Gamma = (\Gamma_H - \Gamma_V) - (\Gamma_H^* - \Gamma_V^*), \qquad \text{Eq. 6-1}$$

where Γ_H^* and Γ_V^* were computed using the Fresnel equations (Eqs. 4-5 and 4-6), and Γ_H and Γ_V were calculated using the HQN model (Eq. 2-5).

Subsequently, the semi-empirical model for bare soil (Eq. 4-4) was employed as the forward model to calibrate the roughness parameter and retrieve soil moisture. Given that the same mono-angular configuration as SMAP (~40°) was adopted in this thesis, the SMAP SCA approach (see Chapter 2.4.2) was implemented to retrieve the soil moisture in flat and periodic soil at P- and L-band, assuming $Q_R = 0$ and $N_{RH} = N_{RV} = 2$. The roughness parameter H_R were locally calibrated in Q1-Q4 by feeding the forward model (Eq. 4-4) with coincident TB and soil moisture measurements. Afterward, the calibrated parameters over the flat soil (Q2) were applied to the soil moisture retrieval over the periodic soil surfaces (Q1, Q3 and Q4), taking Q2 as calibration data and Q1, Q3 and Q4 as validation data. Finally, the retrieval performance for Q1, Q3 and Q4 was compared to Q2 as a benchmark.

Inversion of the forward model used the SLSQP (Sequential Least SQuares Programming, Kraft, 1988) algorithm to iteratively minimize a cost function (CF) computed from the differences between the observed TB ($\mathrm{TB}_P^{\mathrm{obs}}$) and the simulated TB ($\mathrm{TB}_P$) at either H- or V-pol, expressed as

$$\mathrm{CF} = \left(\mathrm{TB}_P^{\mathrm{obs}} - \mathrm{TB}_P\right)^2. \qquad \text{Eq. 6-2}$$

The initial value of soil moisture was set to zero to avoid any potentially misleading prior knowledge in the retrieval. A bound of 0-0.7 m^3/m^3 was imposed on the retrieved soil moisture to ensure reasonable values were obtained, since the saturated soil moisture at this site is around 0.7 m^3/m^3 (Table 3-3).

6.4 Results and Discussion

6.4.1 Physical modeling of random roughness

Figure 6-4 shows the smooth surface roughness limit for different wavelengths and incidence angles according to the Fraunhofer criterion (Ulaby et al., 1982). Accordingly, it can be seen that at 40° incidence angle, the roughness effects can notionally be ignored at both P- and L-band providing the RMS roughness height is lower than 0.8 cm. However, for a surface with RMS height ranging from 0.8 to 1.6 cm it can only be considered electromagnetically smooth at P-band. Moreover, if the RMS height increases beyond 1.6 cm, it suggests that the roughness cannot be neglected even at P-band.

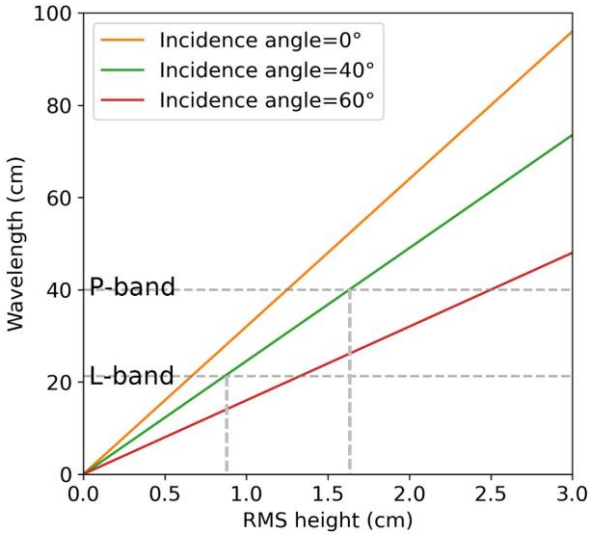

Figure 6-4: The maximum RMS height to consider a surface electromagnetically smooth for a given observation wavelength in the microwave range, calculated using the Fraunhofer criterion (Ulaby et al., 1982).

Figure 6-5 presents the simulated emissivity using the I^{2}EM (Eqs. 4-16-4-20) for a specular, a smooth, and a relatively rough surface, encompassing the roughness range of typical flat soil surfaces, being mostly located within the range of 0.5-2 cm and 4-15 cm for RMS height and correlation length, respectively (Mialon et al., 2012, Lawrence et al., 2013, Fernandez-Moran et al., 2015). The RMS heights of the smooth (0.8 cm) and rough (1.6 cm) surface were the breakpoints for L- and P-band, respectively, according to the Fraunhofer criterion (Figure 6-4).

In Figure 6-5, the offset from the specular surface curve can characterize the impact of the random roughness, being reduced at longer wavelengths. Accordingly, a surface with 0.8-cm RMS height and 11.1-cm correlation length could be considered smooth at 0.3 GHz/100-cm wavelength and 0.75 GHz/40-cm wavelength, evidenced by the overlapped blue and orange curves. This also was true at 1.4 GHz/21-cm wavelength for incidence angles close to 40°. For the rough surface, the roughness effects could be ignored at 0.3 GHz/100-cm wavelength but not at 0.75 GHz/40-cm wavelength or 1.4 GHz/21-cm wavelength. However, it can still be seen that the impact at 1.4 GHz/21-cm wavelength was more pronounced than that at 0.75 GHz/40-cm wavelength.

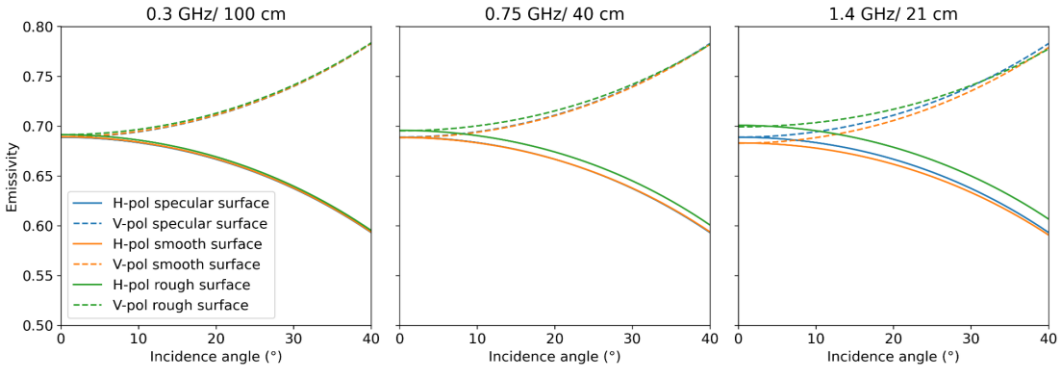

Figure 6-5: Emissivity simulated using the physical model over different soil surfaces and at three frequencies, i.e., 0.3 GHz, 0.75 GHz, and 1.4 GHz. The dielectric constant was assumed to be 12 - j2.4 (~0.25 m^3/m^3 in soil moisture). The specular, smooth, and rough surfaces were assumed to have zero RMS height and 50-cm correlation length, 0.8-cm RMS height and 11.1-cm correlation length as observed in quadrant 2, and 1.6-cm RMS height and 6.8-cm correlation length as observed at this tower site in a different period, respectively.

6.4.2 Physical modeling of multi-scale roughness

Figure 6-6 shows the comparison of simulated and observed emissivity over different periodic surfaces. Only sinusoidal surfaces (quadrants 3 and 4) were considered herein to explore the multi-scale roughness and azimuth issue. First, only the random roughness was modeled using the I^{2}EM model (Eqs. 4-16-4-20) by ignoring periodic roughness. Next, the model for sinusoidal surfaces (Eqs. 4-21 and 4-22) was used to simulate the multi-scale roughness with random roughness on top of periodic roughness. The roughness measurements in Table 6-1 were used in simulations accordingly.

It can be seen in Figure 6-6 that P-band had a better performance than L-band in all scenarios. Although the ubRMSE in quadrant 3 was the same at P- and L-band, P-band had higher R values compared to L-band. From the comparison of top and bottom rows, the performance in quadrant 4 was improved substantially after accounting for the periodic roughness, while the statistics were degraded in quadrant 3. In line with Figure 6-6, Promes et al. (1988) observed that another similar model (Wang et al., 1980) had a better agreement with observations for parallel- than

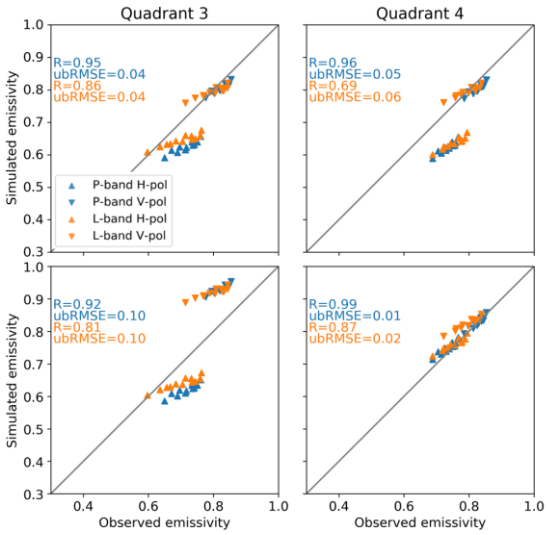

Figure 6-6: Emissivity simulations compared against observations at P- and L-band using the I^{2}EM over sinusoidal surfaces with perpendicular (left column) and parallel (right column) row structures. Top row: only random roughness was simulated; and bottom row: both periodic and random roughness was simulated.

perpendicular-look direction. Therefore, it is suggested that this type of model should be used with caution over periodic surfaces with a perpendicular-look direction.

Although there have been a few models for simulating surfaces with multi-scale roughness (Wang et al., 1980, Ulaby et al., 2014), it is still impractical to use them in global soil moisture retrieval. Reasons include, 1) these models rely heavily on accurate roughness measurements including period, amplitude, and azimuth of the row structures which are difficult to obtain globally; and 2) the model accuracy was not always satisfactory (e.g., Figure 6-6) even though the roughness measurements were carefully sampled in the field. This finding is supported by Promes et al. (1988) who evaluated the model from Wang et al. (1980) using ground-based observations and found this model tended to overestimate the influence of the row structure. A potential reason to explain this is that these models were developed based on some assumptions, e.g., the radiometer footprint contains many spatial periods, which may not be fulfilled when the footprint extends across only a few meters in ground-based experiments.

6.4.3 Depolarization effects

Figure 6-7 shows the magnitude of the depolarization effect of roughness ($\Delta\Gamma$) using Eq. 6-1 and different N_{RP} values. It can be seen from the figure that both the SMOS ($N_{RH} = 2$ and $N_{RV} = 0$) and SMAP ($N_{RH} = N_{RV} = 2$) parameterization did not imply a substantial depolarization effect, being close to 0. The depolarization is due to the fact that roughness impacts amplify H-pol emissivity to a greater degree compared to V-pol emissivity (Shi et al., 2002, Mialon et al., 2012), in line with Figure 6-5 particularly for L-band. This results in a reduced difference between H- and V-pol observations.

Depolarization could adversely impact soil moisture retrieval. Konings et al. (2015) pointed out that a robust retrieval can only be guaranteed if the DoI of a set of observations is larger than the number of the retrieved parameters. Accordingly, this depolarization reduces the independence of the observations at H- and V-pol and thus the DoI.

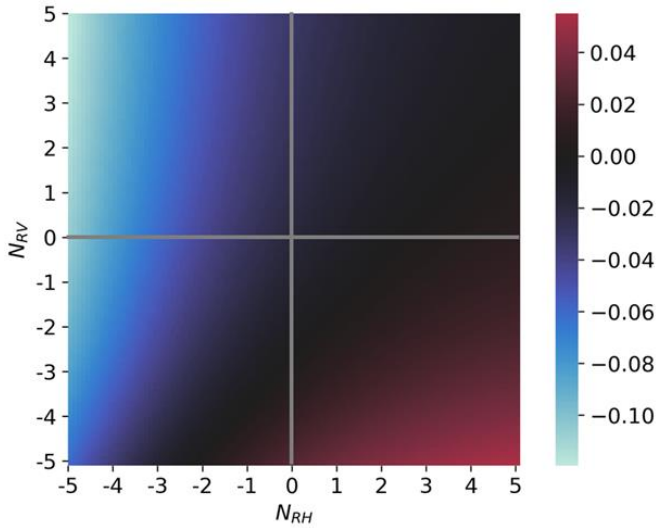

Figure 6-7: Magnitude of the depolarization effect ($\Delta\Gamma$) calculated using Eq. 6-1 with different N_{RH} and N_{RV} values. The dielectric constant, H_R, Q_R, and incidence angle were assumed to be 12 - j2.4 (~0.25 m^3/m^3 in soil moisture), 0.1, 0, and 40°, respectively.

In a mono-angular retrieval, N_{RP} can be seen as a coefficient of H_R that characterizes the intensity of roughness. A larger N_{RP} value makes the roughness coefficient, i.e., $\exp[-H_R\cos^{N_{RP}}(\theta)]$ in the HQN model (Eq. 2-5), closer to one, indicating a reduced roughness impact. Accordingly, ΔN_R, i.e., $\Delta N_R = N_{RH} - N_{RV}$, is also able to characterize the depolarization effect apart from $\Delta\Gamma$. In addition, a negative relation of ΔN_R and roughness was established by Mialon et al. (2012) and Lawrence et al. (2013).

It can be noticed from Figure 6-7 that $\Delta\Gamma$ is more likely to be non-positive, in line with literature observations that roughness-induced depolarization was often seen (Newton and Rouse, 1980, Wang et al., 1983, Mialon et al., 2012). A positive $\Delta\Gamma$ value is scarce to observe over bare soil because it indicates that roughness enlarges the difference between the reflectivity at both polarizations. This phenomenon can only be observed at low incidence angles (e.g., lower than 20°) over periodic soil surfaces (Wang et al., 1980, Zheng et al., 2012). Consequently, N_{RP} values should be used with caution when ΔN_R is larger than 5, as indicated by the red area in Figure 6-7.

6.4.4 Parameter calibration and soil moisture retrieval

In Figure 6-8, a range of H_R values were used to simulate the TB for P- and L-band and H- and V-pol respectively using the semi-empirical model for bare soil (Eq. 4-4). The H_R values that produced the minimum RMSE between the simulated and observed TB were considered the optimum, marked as the dots with annotated values.

Compared to L-band, the HQN model performed better at P-band based on its lower RMSE. For example, the minimum RMSE in Q1 and Q3 was no higher than 6 K at P-band, while that at L-band was higher than 10 K. Moreover, at L-band V-pol, the RMSE in Q3 and Q4 was a minimum at $H_R = 0$ and will further decrease if negative H_R is allowed. These phenomena can be attributed to the substantial impact of periodic row structures and the inapplicability of the SMAP SCA configuration (i.e., $Q_R = 0$ and $N_{RV} = 2$) for periodic roughness at L-band. For both P- and L-band and both H- and V-pol, Q2 had the lowest calibration residual across the four quadrants

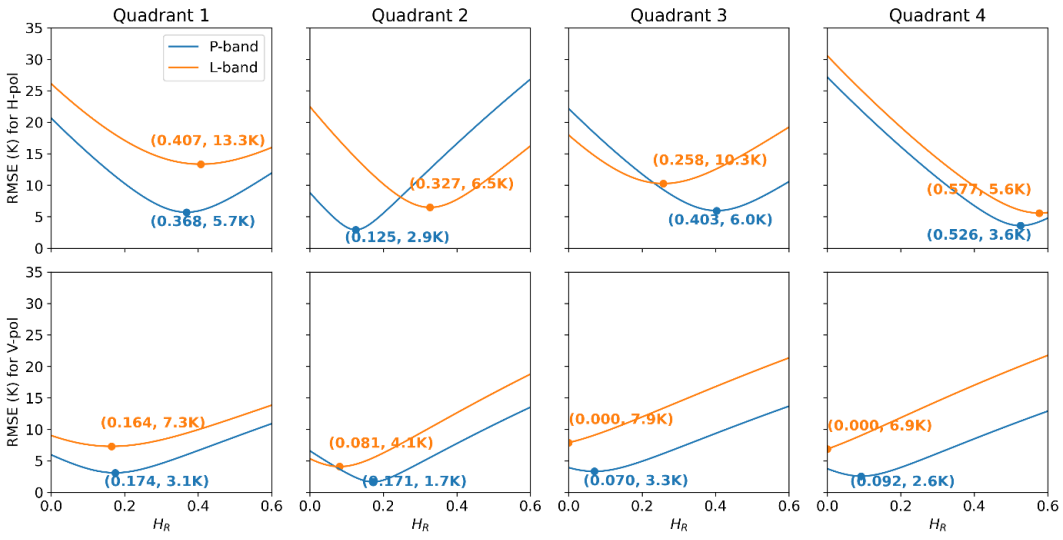

Figure 6-8: RMSE (K) between the observed and simulated TB using a range of H_R values at H-pol (top row) and V-pol (bottom row) over the bare soil in each quadrant. The semi-empirical model for bare soil (Eq. 4-4) was adopted as the forward model. The dots with values indicate the minimum RMSE and the corresponding H_R values for P-band (in blue) and L-band (in orange). The parameters Q_R and N_{RP} were assumed to be the same as in the SMAP SCA at both P- and L-band, being 0 and 2, respectively.

with only one exception (L-band H-pol in Q4), indicating the more considerable roughness impact of periodic surfaces than from the flat surface in Q2. Importantly, the H_R in the four quadrants was more comparable at P- than L-band at V-pol, with the standard deviation being 0.046 and 0.068, respectively.

To evaluate the induced retrieval error from applying the calibrated H_R in flat soil to periodic soil, the optimal parameters calibrated in Q2 (Figure 6-8) were used to retrieve the soil moisture in all four quadrants for both bands and both polarizations, with the comparison of the retrieved and observed soil moisture plotted in Figure 6-9. As expected, Q2 was seen to have the best retrieval performance across all four quadrants because the H_R had been calibrated in Q2. P-band was found to perform better than L-band in RMSE in all quadrants except Q4 for H-pol. In Figure 6-9, V-pol had better retrieval accuracy than H-pol at both P- and L-band. Focusing on V-pol (Figure 6-9 bottom row), P-band had similar RMSEs across all four quadrants, whereas L-band

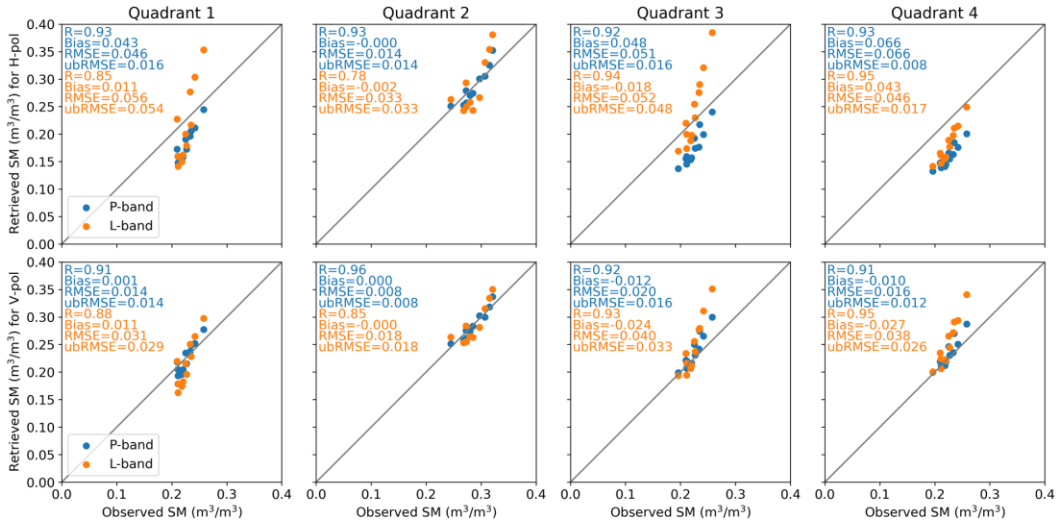

Figure 6-9: Retrieved versus observed soil moisture for H-pol (top row) and V-pol (bottom row) over the bare soil in each quadrant, using the SCA (Eq. 6-2) with the bare soil forward model (Eq. 4-4). Calibrated H_R values from the period of bare flat soil in Q2 were used for all quadrants here, i.e., 0.125 and 0.171 for P-band H- and V-pol, respectively, and 0.327 and 0.081 for L-band H- and V-pol, respectively. The parameters Q_R and N_{RP} were assumed to be the same as those from the SMAP SCA at both P- and L-band, being 0 and 2, respectively.

showed higher RMSE over periodic soil (0.031-0.040 m^3/m^3) than that over flat soil (0.018 m^3/m^3), indicating the reduced roughness impact at P-band.

Importantly, the orientation of the row structure mattered; while the retrieval performance was not substantially different between Q3 and Q4 (Figure 6-9), the parallel row structure in Q4 led to a larger H_R value, particularly at H-pol (Figure 6-8), in spite of the same row spacing and height. It should be noted that, although it fits with intuition that parallel row structures impose less roughness impact than perpendicular row structures, this is not the case according to either this research or the literature (Wang et al., 1980, Ulaby et al., 2014).

6.5 Chapter Summary

This chapter compared P- with L-band over bare flat and periodic soil surfaces to determine if there is an improvement in TB simulation and soil moisture retrieval accuracy, due to reduced roughness impact when using a longer wavelength. Results from the Fraunhofer criterion, semi-empirical and physical modeling indicated that P-band was less impacted by random and periodic roughness than L-band. Moreover, the parallel row structure led to a larger H_R value than the perpendicular row structure in spite of the same row spacing and height, particularly at H-pol. Importantly, this chapter has demonstrated that P-band did not need to have the periodic surfaces discriminated, while L-band needed differently calibrated parameters for bare periodic surfaces compared to bare flat surfaces due to the more considerable roughness impact, evidenced by the more comparable RMSE at P-band (variation of up to 0.012 m^3/m^3) than L-band (variation of up to 0.022 m^3/m^3) across different roughness configurations. The calibrated roughness parameters in this chapter were used in the next chapter for the wheat-covered flat and periodic soil surfaces.

7 Vegetation Impact of Wheat

Chapter 6 has demonstrated the reduced roughness impact from random and periodic soil surfaces at P-band compared to L-band. This chapter evaluated the tau-omega model (see Chapter 4.1) at P- and L-band over the same soil surfaces as in Chapter 6 but covered by matured wheat (see Chapter 3). The calibrated roughness parameters from Chapter 6 were used in this chapter. The work in this chapter has been published in Shen et al. (2022b).

7.1 Background

The vegetation canopy attenuates (absorbs and scatters) the soil emission and adds its own contribution to the overall emission, resulting in a noticeable reduction in the sensitivity of TB to soil moisture (Jackson et al., 1982). Accordingly, Mo et al. (1982) proposed the tau-omega model to relate the TB to soil moisture of vegetation-covered soil (Chapter 4.1). The τ is directly proportional to the VWC of the canopy, while the ω primarily depends on the type of vegetation (Mo et al., 1982). The tau-omega model is essentially a zero-order solution of the radiative transfer equations where multiple scattering is neglected, with applicability and accuracy being widely evaluated (Gao et al., 2018, Li et al., 2020). Many retrieval algorithms have been developed based upon this practical model, e.g., the SCA (Jackson, 1993) and the DCA (Njoku and Li, 1999, Njoku et al., 2003) for SMAP. It is worth noting that the DCA has replaced the SCA-V as the SMAP baseline algorithm since October 2021 due to its improved retrieval performance in some agricultural areas (O'Neill et al., 2021a).

Although the SMAP radiometer-based soil moisture data meets its overall target accuracy, errors for croplands are considerably larger (Chan et al., 2016, Colliander et al., 2017b, Walker et al., 2019). Moreover, current SMAP and SMOS algorithms do not specifically consider any correction of the periodic row structure. Use of P-band is a promising approach to conquering these difficulties due to its reduced impact from

vegetation (Ulaby et al., 1986). Chapter 6 has demonstrated that this simplification is more acceptable at P- compared to L-band in terms of the retrieval error. However, when covered by wheat with low to intermediate VWC it remains unclear if these periodic soil surfaces need to be discriminated from flat soil surfaces at P- and L-band.

In this chapter, the tau-omega model was implemented at P-band for the first time to evaluate the vegetation effects at P- and L-band by comparing the retrieval errors before and after accounting for the wheat canopy in the forward model. Furthermore, the possibility of retrieving soil moisture over wheat-covered soil without discriminating periodic and flat surfaces was investigated, by applying the roughness and vegetation parameters calibrated in flat soil to retrieve the soil moisture of periodic soil with the SMAP SCA and DCA. This demonstration suggests that an improved global soil moisture dataset may be possible using the longer wavelength P-band observations, even if the same algorithms as those of SMAP are used.

7.2 Data

Quadrants 1-4 were plowed with varied roughness structures for the wheat-growing cycle from July to December 2019 (see Chapter 3) to compare the random roughness

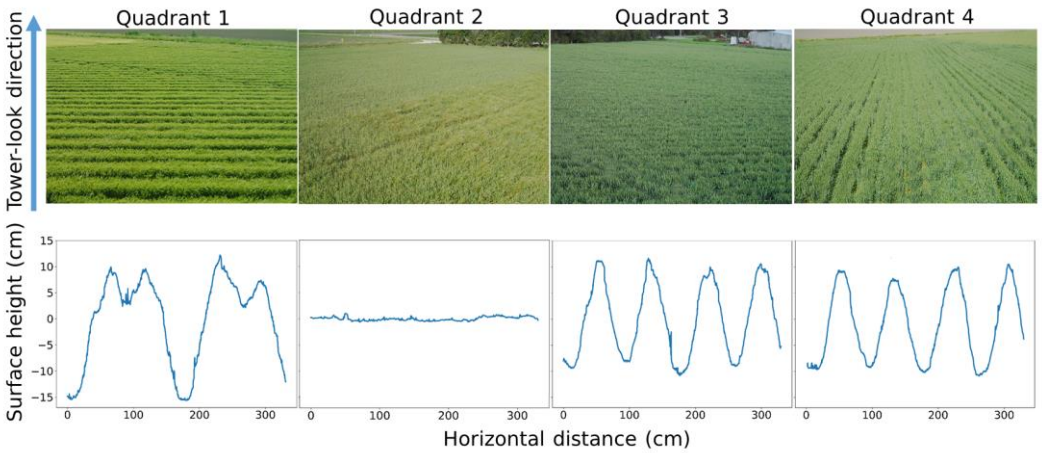

Figure 7-1: Photos at the maturity of wheat (top row) and diagrams of soil surface profiles (bottom row) of the four quadrants. Quadrants 3 and 4 were plowed in one pass and had the same roughness structures but with different orientations (perpendicular and parallel, respectively) relative to the tower look direction.

of flat soil and the periodic roughness of furrowed soil (Figure 6-1 and Figure 7-1). Table 7-1 shows the roughness measurements taken during the whole wheat-growing period. Note that these roughness measurements were not used in the formal analysis but to support that the roughness parameters can be assumed constant over the entire study period.

In this chapter, two periods in the entire wheat-growing cycle were used: 1) the bare soil period from July 17 to 31, 2019, before wheat germination (see Chapter 6); and 2) the wheat-covered soil period (Figure 7-1) from November 13 to December 21, 2019, when matured wheat was senescing (a data example is plotted in Figure 7-2). The current study used the daily TB observations at 40° incidence angle for P-band and at 38° incidence angle for L-band (Figure 7-2a), in order to approximate the fixed 40° incidence angle of SMAP (Entekhabi et al., 2014).

Table 7-1: Characterization of the roughness in the four quadrants.

Q	Row structure	Periodic roughness				Random roughness		
		No. of profiles	Azimuth (°)	Period (cm)	Amplitude (cm)	No. of profiles	RMS height (cm)	Correlation length (cm)
1	Sinusoidal bench	6	90	165	10.5 ± 1.3	6	1.1 ± 0.5	9.2 ± 4.3
2	Flat	–	–	–	–	16	0.9 ± 0.2	9.5 ± 2.7
3	Sinusoidal	7	90	80	9.8 ± 1.2	7	0.8 ± 0.3	9.0 ± 4.2
4	Sinusoidal	7	0			7		

Azimuth is the angle between the radiometer look direction and the row direction; period is the row spacing; and amplitude is half of the vertical distance between the bottom and the top of the row. For the periodic soil in Q1, Q3, and Q4, the roughness measurements across the rows were used to calculate the "periodic roughness" in the table, while those along the rows were used to calculate the "random roughness" in the table. For Q2, the measurements in two perpendicular directions were averaged to calculate the roughness statistics. Q3 and Q4 were plowed in one pass and had the same roughness structure (just different orientations relative to the tower look direction), and therefore the measurements in these two quadrants were averaged.

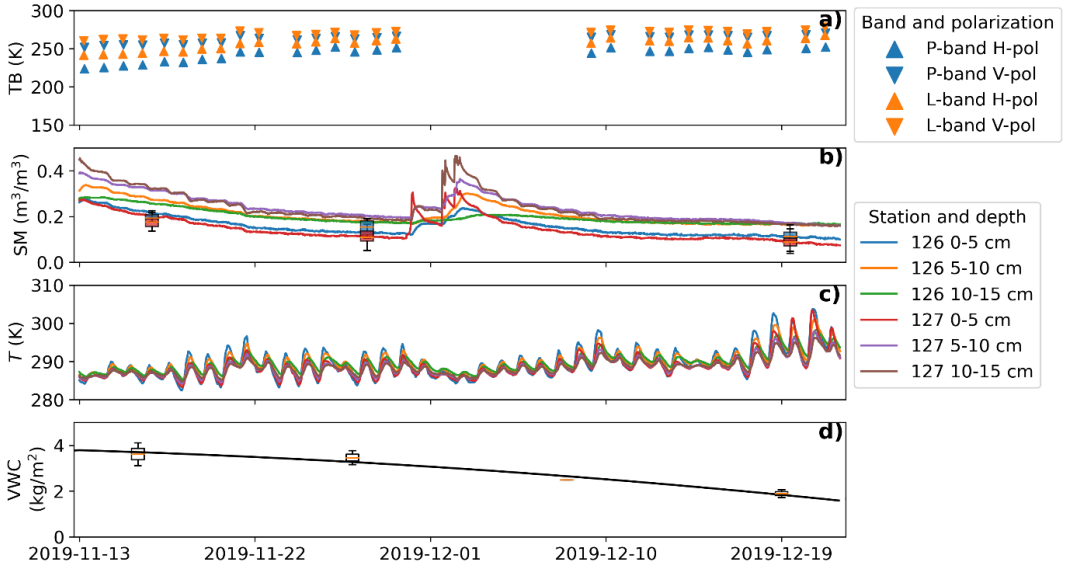

Figure 7-2: Collected data including a) TB observations at 6 am in Q1 as an example, with the data gaps resulting from the tower being lowered due to high wind on those days; b) station time-series soil moisture with HDAS measurements (boxplots); c) station time-series soil temperature; and d) observed (boxplots) with fitted (black line) vegetation water content in Q1 as an example. For clarity only the data collected from the top 3 sensors are plotted in b) and c). Corresponding to the soil moisture evolutions of station 126 (in blue) in Q2 and station 127 (in red) in Q1, Q3 and Q4, the blue and red boxplots in b) show the maximum, 75% percentile, median, 25% percentile, and minimum of the spatial HDAS measurements in Q2 as well as Q1, Q3 and Q4, respectively.

Figure 7-2b and c show the time series of soil moisture and temperature, respectively, collected from stations 126 and 127 (Figure 3-1a and Figure 3-5a and b). This investigation follows Chapter 6 by using station 126 as the reference in Q2 and station 127 as the reference for Q1, Q3, and Q4 based on the agreement between HDAS measurements and the station soil moisture in flat and periodic quadrants, respectively (Figure 7-2b). The station observations were considered representative of the radiometer footprints because the HDAS measurements were relatively uniform across each quadrant and agreed with the corresponding station measurements (Figure 7-2b). The destructive vegetation samples were taken weekly (Figure 3-5e) at the locations shown in Figure 3-1a. Accordingly, Figure 7-2d presents the VWC

measurements as boxplots and a fitted quadratic polynomial function to represent the VWC evolution.

While P-band was found to have a greater moisture retrieval depth (~7 cm) than L-band (~5 cm) over bare soil (Chapter 5), the presence of wheat could reduce the moisture retrieval depth to close to 5 cm at P-band and shallower at L-band. Given the difficulty in continuously measuring soil moisture at shallower depths, and the highly correlated soil moisture between neighboring layers, the daily mean soil moisture at around 6 am in the 0-5-cm layer from the station (Figure 7-2b) was used for both P- and L-band evaluation in this chapter.

7.3 Method

Given that the same mono-angular configuration as SMAP (~40°) was adopted in this research, the SMAP SCA and DCA approaches were implemented to evaluate the tau-omega model over wheat-covered flat and periodic soil surfaces at P- and L-band. Similar to Chapter 6, the calibrated parameters over the flat soil (Q2) were applied to the soil moisture retrieval over the periodic soil surfaces (Q1, Q3 and Q4), taking Q2 as calibration data and Q1, Q3 and Q4 as validation data. Finally, the retrieval performance for Q1, Q3 and Q4 was compared to Q2 as a benchmark.

Roughness and vegetation parameters can compensate for each other and thus cannot be calibrated together to achieve a robust result (Njoku and Chan, 2006, Patton and Hornbuckle, 2012, Martens et al., 2015). To disentangle roughness and vegetation effects, Wigneron et al. (1995) separately calibrated roughness and vegetation parameters by using the data before and after the vegetation canopy development, respectively. A similar methodology was also employed in this research because the surface roughness was found to have little change throughout the entire period, as indicated by the small standard deviation in Table 7-1.

7.3.1 Single channel algorithm

The SCA (Jackson, 1993) retrieves soil moisture using the TB observation at either H- or V-pol with all roughness and vegetation parameters known (Table 7-2). The b in Table 7-2 is an empirical parameter that builds a linear relationship between τ and VWC (Jackson and Schmugge, 1991), and thus τ can be estimated from Eq. 2-7. As in the SMAP SCA (O'Neill et al., 2021a), this research assumed the parameters in Table 7-2 were invariant throughout the study period.

Additional to applying the default SMAP parameters to the soil moisture retrieval, vegetation parameters were locally calibrated in Q1-Q4 by feeding the forward model with coincident TB and soil moisture measurements using the roughness parameters calibrated over the bare soil period in Chapter 6. The same SCA inversion algorithm as in Chapter 6 was conducted in this chapter. Please refer to Chapter 6.3 and Eq. 6-2.

7.3.2 Dual channel algorithm

The DCA (Njoku and Li, 1999, Njoku et al., 2003) uses dual-pol TB observations to retrieve two parameters. Unlike the SCA, the SMAP DCA uses a global map of H_R to concurrently retrieve soil moisture and τ. The H_R values vary from pixel to pixel, so no specific H_R value can be referred to in this chapter. In addition, while N_{RP} is assumed to be 2 as in the SCA, Q_R is no longer assumed to be a constant value. Accordingly, H_R and Q_R were calibrated locally in Q1-Q4 using the bare soil data prior to undertaking retrieval in this chapter. Afterward, soil moisture and τ were

Table 7-2: The default SMAP SCA parameters for croplands (O'Neill et al., 2021a).

Parameter	Value
H_R	0.108
Q_R	0
N_{RP}	2
b	0.11
ω	0.05

concurrently retrieved using the dataset for the wheat-covered period and the calibrated H_R and Q_R in Q2. The ω was assumed to be the same as in the SMAP DCA for both P- and L-band, being 0.6.

The CF minimized by the SLSQP algorithm using dual-pol TB at ~40° incidence angle during the retrieval period was

$$\mathrm{CF} = \left(\mathrm{TB}_H^{\mathrm{obs}} - \mathrm{TB}_H\right)^2 + \left(\mathrm{TB}_V^{\mathrm{obs}} - \mathrm{TB}_V\right)^2 + \frac{\left(\tau^{\mathrm{ini}} - \tau\right)^2}{\sigma(\tau)^2}, \qquad \text{Eq. 7-1}$$

where τ^{ini} and τ are the initial and retrieved values of the optical depth, and $\sigma(\tau)$ is the parameter to balance the weight of the retrieved parameters for the optimization process to converge. The initial values of soil moisture and τ were set to zero. The same $\sigma(\tau)$ value as in the SMAP DCA was adopted, i.e., 0.05 (O'Neill et al., 2021a).

7.4 Results and Discussion

7.4.1 Single channel algorithm

The default SMAP SCA parameters for croplands (Table 7-2) were evaluated at P- and L-band and H- and V-pol over the wheat-covered soil with different roughness structures using the tau-omega model (Eq. 4-1), with the simulated and observed TB compared in Figure 7-3. L-band was found to substantially outperform P-band in all cases, indicating the inapplicability of the default SMAP SCA parameters at P-band. Consistent with the results in Chapter 6, Figure 7-3 also shows a superior performance at V- over H-pol. More specifically, the RMSE at L-band was no higher than 3 K at V-pol, demonstrating that the default SMAP SCA parameters were applicable to a wide range of roughness and vegetation conditions with satisfactory accuracy. In the following, only V-pol was analyzed due to its superiority over H-pol.

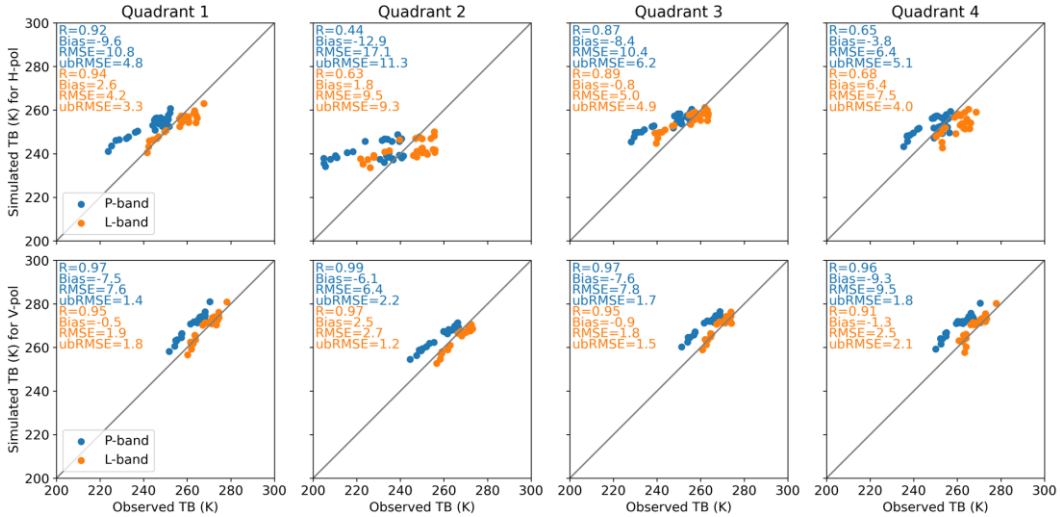

Figure 7-3: Comparison of TB simulations against observations for H-pol (top row) and V-pol (bottom row) over the wheat-covered soil in each quadrant, using the SCA with the tau-omega model. The default SMAP SCA parameters in Table 7-2 were used for all quadrants, both bands, and both polarizations.

The SMAP SCA parameters were demonstrated to work very well at L-band with low RMSE shown in Figure 7-3, and therefore only the vegetation parameters (b and ω)

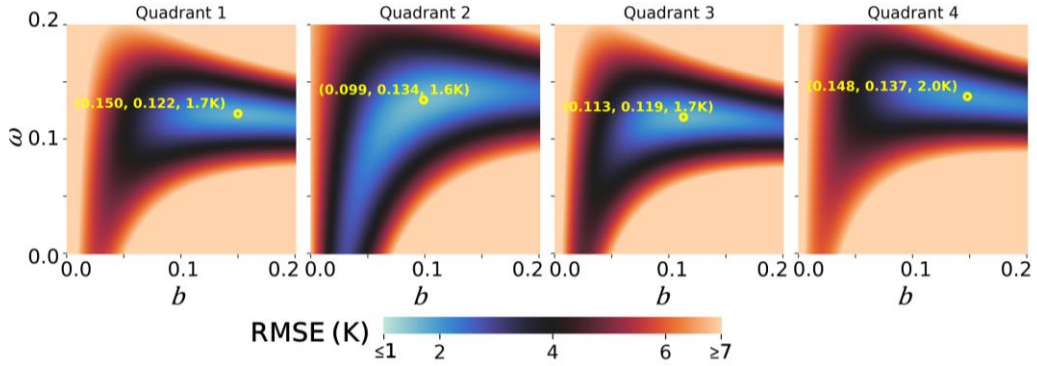

Figure 7-4: RMSE (K) between the observed and simulated TB using a range of b and ω values for P-band V-pol over the wheat-covered soil in each quadrant. The tau-omega model was adopted as the forward model. The yellow circles indicate where the minimum RMSE was reached, with the three values showing b, ω, and the minimum RMSE, respectively. The calibrated H_R values at P-band V-pol from the period of bare soil, i.e., 0.174, 0.171, 0.070, and 0.092, were used for Q1-Q4, respectively. The parameters Q_R and N_{RP} were assumed to be the same as in the SMAP SCA, being 0 and 2, respectively.

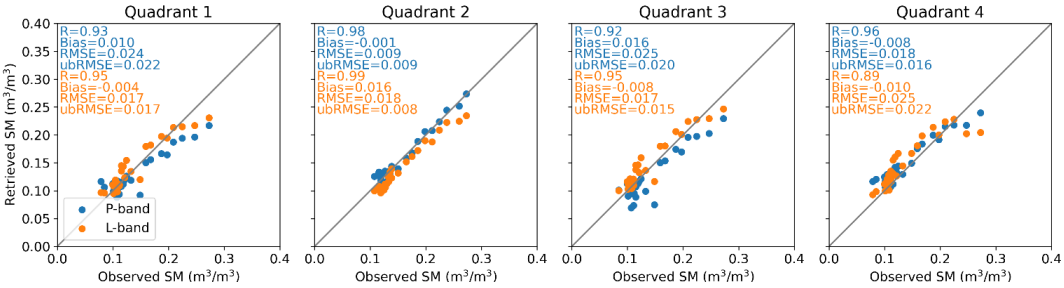

Figure 7-5: Observed versus retrieved soil moisture over the wheat-covered soil in each quadrant, using the SCA-V with the tau-omega model. The default SMAP SCA Q_R and N_{RP} and the calibrated H_R, b, and ω parameters in Q2 (flat soil) were used for P-band in all quadrants here, i.e., Q_R = 0, N_{RP} = 2, H_R = 0.171, b = 0.099, and ω = 0.134. The default SMAP SCA parameters in Table 7-2 were used for L-band in all quadrants.

at P-band were calibrated in Figure 7-4. The soil moisture measurements collected over the wheat-covered soil were adopted to simulate TB, using the tau-omega model with calibrated H_R (Figure 6-8) and varying b and ω. Overall, the b and ω values differed slightly across quadrants, ranging from 0.099 to 0.150 and from 0.119 to 0.137, respectively (Figure 7-4). The varied b and ω can be partially attributed to the different residuals of the roughness calibration that were left to be compensated by b and ω. Comparing the default and calibrated parameters, ω differed more considerably than other parameters, being 0.05 in the default configuration (Table 7-2) and ~0.12-0.13 after calibration (Figure 7-4).

Soil moisture was subsequently retrieved at P- and L-band V-pol using the tau-omega model (Figure 7-5). While the roughness (Figure 6-8) and vegetation (Figure 7-4) parameters were calibrated at P-band in all four quadrants, only the parameters calibrated in Q2 (H_R= 0.171, b= 0.099, and ω= 0.134) were used for the soil moisture retrieval at P-band (Figure 7-5). At L-band, the SMAP SCA parameters (Table 7-2) were applied to the soil moisture retrieval (Figure 7-5). It can be seen from Figure 7-5 that the RMSEs/ubRMSEs were similar across all four quadrants either at P- or L-band (variations no more than 0.016 m^3/m^3), suggesting the possibility to ignore the different roughness structures underneath vegetation when retrieving soil moisture.

7.4.2 Dual channel algorithm

Before applying the DCA soil moisture retrieval to the vegetated period, the full-time-series TB and soil moisture during the bare soil period were used to calibrate the roughness parameters, i.e., H_R and Q_R at P- and L-band in each quadrant, shown in Figure 7-6. The H_R and Q_R values that produced the minimum RMSE were considered as the calibrated values, marked as the yellow circles with annotated values in Figure 7-6.

Figure 7-6 shows a lower RMSE at P- than L-band in the four quadrants, being 2.6-4.8 K and 5.4-10.8 K, respectively. This indicates that the HQN model performs better at P-band due to the reduced roughness impact. Q2 had the lowest calibration residual across the four quadrants for both P- and L-band because of its relatively smooth surface compared to the periodic soil surfaces in Q1, Q3 and Q4. While Q_R is usually

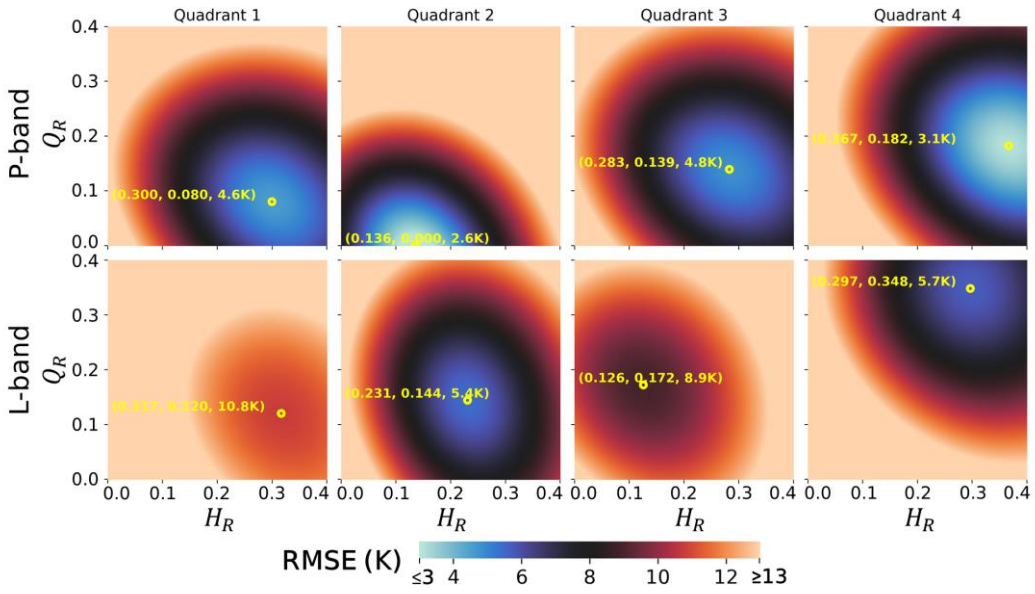

Figure 7-6: RMSE (K) between the observed and simulated dual-pol TB using a range of H_R and Q_R values for P-band (top row) and L-band (bottom row) over the bare soil in each quadrant. The model for bare soil (Eq. 4-4) was adopted as the forward model. The yellow circles indicate where the minimum RMSE was reached, with the three values showing H_R, Q_R, and the minimum RMSE, respectively. The N_{RP} was assumed to be 2, the same as in the SMAP DCA, at both P- and L-band.

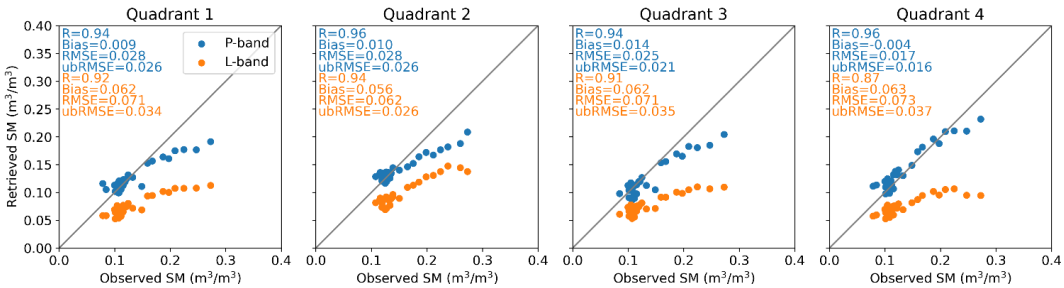

Figure 7-7: Observed versus retrieved soil moisture over the wheat-covered soil in each quadrant, using the DCA (Eq. 7-1) with the tau-omega model. The default SMAP DCA N_{RP} and ω were used for both P- and L-band, i.e., $N_{RP} = 2$ and $\omega = 0.06$. The calibrated H_R and Q_R from the period of bare flat soil in Q2 were used for all quadrants, i.e., $H_R = 0.136$ and $Q_R = 0$ for P-band and $H_R = 0.231$ and $Q_R = 0.144$ for L-band.

assumed to be zero (e.g., Wigneron et al., 2001, Martens et al., 2015), this assumption was only valid at P-band and not necessarily valid at L-band in Q2 when using dual-pol TB. Moreover, Figure 7-6 supports that non-zero Q_R should apply for periodic surfaces when performing a DCA retrieval. It is also worth noting that H_R and Q_R were larger in Q4 than Q3, particularly at L-band, indicating that the periodic surface with parallel structures might have a larger impact than that with perpendicular structures at ~40° incidence angle, in spite of the same row spacing and height.

Figure 7-7 presents the comparison of the observed and retrieved soil moisture when applying the H_R and Q_R calibrated in Q2 (Figure 7-6) to all four quadrants. P-band was found to perform better than L-band in all metrics. Similar to the SCA result in Figure 7-5, the RMSEs and ubRMSEs shown in Figure 7-7 at either P- or L-band were comparable across the four quadrants, with variations of no more than 0.011 m^3/m^3.

While the SMAP baseline algorithm has recently changed to the DCA from the SCA-V due to the improved performance in some agricultural areas (O'Neill et al., 2021b), based on Figure 7-5 and Figure 7-7 in this research, the DCA showed higher RMSE (e.g., 0.028 m^3/m^3 at P-band and 0.062 m^3/m^3 at L-band in Q2) than the SCA-V (e.g., 0.009 m^3/m^3 at P-band and 0.018 m^3/m^3 at L-band in Q2). These results are consistent with the earlier validation results of SMAP (Chan et al., 2016).

7.4.3 Estimation of vegetation impact

To investigate whether P-band had a reduced vegetation impact at P-band, the soil moisture was retrieved over the wheat-covered soil in Q2 without considering the vegetation impact in the model, i.e., using the bare soil model with the calibrated H_R parameters in Chapter 6, being 0.171 for P-band and 0.081 for L-band. P-band was found to outperform L-band substantially in RMSE, being 0.029 and 0.063 m^3/m^3 for P- and L-band, respectively (Figure 7-8). The default SMAP H_R values for the SCA (0.15 for bare soil and 0.108 for croplands) were also investigated for both P- and L-band (not shown), and no discernable difference in RMSE was found compared to that in Figure 7-8.

When using one TB observation to retrieve one soil moisture using the tau-omega model (i.e., the SCA), prior vegetation information (e.g., VWC, NDVI, LAI, etc.) is required to estimate τ using Eq. 2-7. When such information is not available, the use of P-band observations can still achieve an acceptable performance (0.029 m^3/m^3 in RMSE) when completely ignoring the vegetation impact by using the bare soil model (Figure 7-8). In contrast, the corresponding RMSE at L-band was as high as 0.063

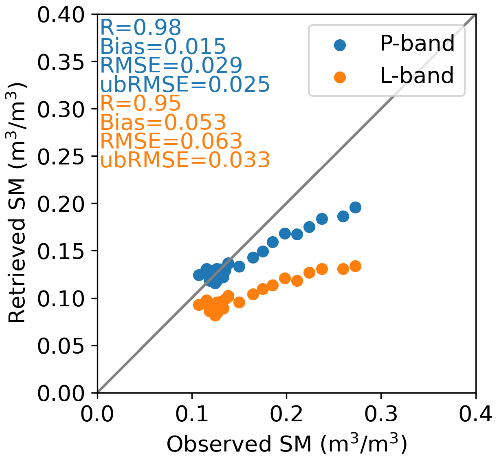

Figure 7-8: Observed versus retrieved soil moisture over the wheat-covered soil in Q2, using the SCA-V with the bare soil forward model (Eq. 4-4). Calibrated H_R values from the period of bare flat soil in Q2 were used here, i.e., 0.171 for P-band and 0.081 for L-band, while Q_R and N_{RV} were assumed to be the same as those from the SMAP SCA at both P- and L-band, being 0 and 2, respectively.

m^3/m^3, demonstrating that the impact of low-to-intermediate vegetation (under 4 kg/m^2) can be neglected at P-band but not at L-band.

7.5 Chapter Summary

This chapter evaluated the tau-omega model over wheat-covered flat and periodic soil surfaces at P- and L-band using the SMAP SCA and DCA approaches. From the aspect of soil moisture retrieval, no substantial variation across different quadrants was observed at both P- and L-band whether using the SCA (Figure 7-5) or the DCA (Figure 7-7), indicating that the same parameters can be used for wheat-covered soil with different roughness structures.

A lower RMSE at P-band (0.029 m^3/m^3) than L-band (0.063 m^3/m^3) was observed when omitting vegetation effects in the forward model, confirming that P-band observations were relatively unaffected by the wheat canopy. However, when using the SCA-V approach with the vegetation impact considered by the tau-omega model, the RMSE was similar (~0.02 m^3/m^3) at P- and L-band (Figure 7-5). Neglecting the vegetation resulted in underestimating the soil moisture observations (Figure 7-8) because the vegetation contribution was mistakenly considered as a soil contribution, increasing the soil emissivity and thus decreasing the soil moisture. This phenomenon was particularly prominent for high soil moisture (Figure 7-8) when the VWC was also high (Figure 7-2). Consequently, it can be postulated that the advantage of P- over L-band in reducing the vegetation impact will become more considerable when the VWC achieves a higher range, e.g., corn (Hornbuckle and England, 2004), which was investigated in the next chapter.

This page is intentionally left blank.

8 Vegetation Impact of Dense Corn

While Chapter 7 has demonstrated a reduced vegetation impact of wheat on soil moisture retrieval at P-band according to its lower RMSE (0.029 m^3/m^3) than L-band (0.063 m^3/m^3) when omitting vegetation effects in the forward model, the performance was similar when using the SCA-V approach with the tau-omega model. Therefore, this chapter has extended the investigation of vegetation impact to conditions with much higher VWC to better understand the retrieval performance at P- as compared to L-band. Similar to Chapter 7, the tau-omega model was employed at P- and L-band but only over a flat soil surface covered by corn with up to 20-kg/m^2 VWC. The SMAP SCA-V and DCA approaches were also applied in this chapter.

8.1 Background

As discussed in Chapter 2.3.5 and Chapter 7.1, vegetation degrades the soil moisture signal by absorbing and scattering radiation emitted from the soil, which becomes more significant as the VWC increases. Ulaby et al. (1983) identified that the radiometric sensitivity to soil moisture at 1.4 GHz and nadir was 3.1 K per 0.01 m^3/m^3 for bare soil and 1.1 K per 0.01 m^3/m^3 for a corn canopy with 5-kg/m^2 VWC. However, when the VWC increased to 6.3 kg/m^2 for corn, the radiometric sensitivity to soil moisture was observed to reduce to 0.5 K per 0.01 m^3/m^3 at 1.4 GHz and V-pol (Hornbuckle and England, 2004). Moreover, the difference in vegetation structure (i.e., the distribution of the dielectric constant) can also contribute to the opacity of the vegetation canopy; Wang et al. (1984) observed no radiometric sensitivity to soil moisture through a grass canopy with 8-kg/m^2 biomass density at 1.4 GHz, whereas for a corn canopy with 8-kg/m^2 biomass density it was 0.5 K per 0.01 m^3/m^3 at 1.4 GHz and V-pol (Hornbuckle and England, 2004).

In Chapter 7, it was identified that for low-to-intermediate vegetation, i.e., wheat with under 4-kg/m^2 VWC, the use of P-band did not achieve a substantially higher retrieval

performance than L-band when accounting for the vegetation contribution using the SCA-V with the tau-omega model. Consequently, this motivated an investigation of corn in this chapter, which has a similar vertical structure as wheat but can reach a much higher VWC. Hornbuckle and England (2004) reported a corn canopy achieving 6.3 kg/m^2 in VWC with a 7.49-m^{-2} plant density. The PRISM tower project managed to plant corn more densely with an ~12-m^{-2} plant density, which together with rainfall and frequent irrigation meant that the VWC peaked at ~20 kg/m^2. Accordingly, the retrieval performance at P- and L-band was evaluated and compared at this high VWC using the SMAP SCA-V and DCA tau-omega approaches in this chapter.

8.2 Data

Since quadrants 1-4 were all managed with a flat surface condition for the corn-growing cycle from November 24, 2020 to May 4, 2021 (Figure 3-2f) and station 126 located in Q2 was found to agree well with the HDAS measurements (Figure 8-1b), only Q2 was selected to be analyzed in this chapter (Figure 8-1). The corn was planted very densely with an ~12-m^{-2} density to achieve a high VWC. The entire growing cycle of corn was divided into three periods: 1) the bare soil period from November 24 to December 9, 2020, being before the corn germination; 2) the maturing period of corn from December 18, 2020 to March 7, 2021; and 3) the senescent period of corn from April 1 to May 4, 2021 (Figure 8-1).

This chapter used the daily TB observations at 40° incidence angle for P-band and at 38° incidence angle for L-band (Figure 8-1a) to approximate the fixed 40° incidence angle of SMAP (Entekhabi et al., 2014). Figure 8-1b and c show the time series of soil moisture and temperature collected from station 126 in Q2 (Figure 3-1a). The station observations were considered representative of the radiometer footprints because the HDAS measurements were relatively uniform in space (short length of boxplots) and agreed approximately with the station measurements (Figure 8-1b). Similar to Chapter 7, the daily mean soil moisture at around 6 am in the 0-5-cm layer from station 126 (Figure 8-1b) was used for both P- and L-band soil moisture retrieval evaluation in this chapter.

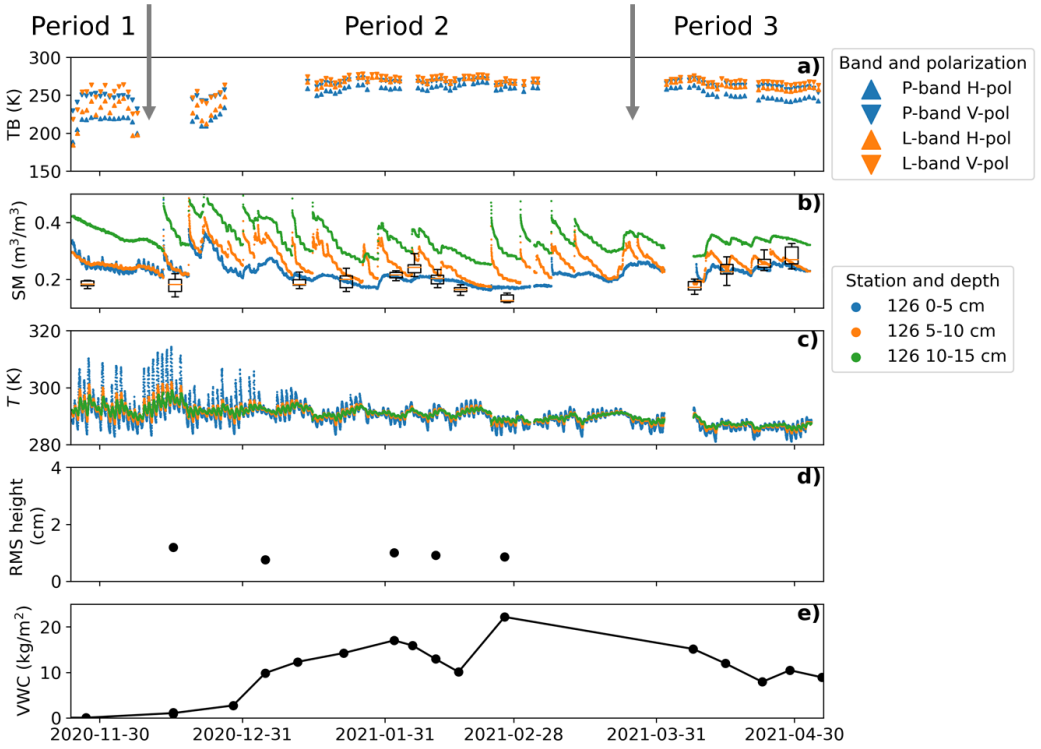

Figure 8-1: Collected data in Q2 over the entire growing cycle of corn, including a) TB observations at 6 am, with the data gaps resulting from the tower being lowered due to high wind in December 2020 and January 2021 and from the instruments being taken to the airborne experiment in March 2021; b) station time-series soil moisture with HDAS measurements (boxplots); c) station time-series soil temperature; d) RMS height averaged from the roughness measurements in two perpendicular directions; and e) observed (dots) with linearly interpolated (line) vegetation water content. For clarity only the data collected from the top 3 hydra-probes are plotted in b) and c). The boxplots in b) show the maximum, 75% percentile, median, 25% percentile, and minimum of the spatial HDAS measurements.

Figure 8-1d shows the RMS height averaged from the roughness measurements taken in two perpendicular directions. Note that these roughness measurements were not used in the formal analysis but rather to support that the roughness parameters can be assumed constant over the study period. The VWC measurements estimated from destructive vegetation samples were plotted as the dots in Figure 8-1e, with the daily

fit plotted as the line. Given the irregular rainfall and irrigation, the VWC reached ~20 kg/m^2 with the time series fluctuating to some extent.

8.3 Method

The same SCA-V and DCA tau-omega approaches as in Chapter 7.3 were implemented over the corn-covered flat soil surface at P- and L-band in this chapter. For the SCA-V approach, τ was estimated using VWC and b according to Eq. 2-7. As in the SMAP SCA-V it was assumed that $Q_R = 0$ and $N_{RV} = 2$ in this chapter. In the SCA approach, roughness and vegetation parameters need to be determined before soil moisture retrieval. However, roughness and vegetation parameters can compensate for each other and thus cannot be retrieved together and achieve a robust result (Njoku and Chan, 2006, Patton and Hornbuckle, 2012, Martens et al., 2015). Therefore, a three-step approach was employed to calibrate parameters and retrieve soil moisture for the SCA-V (Figure 8-2): 1) the H_R was calibrated using the data collected over Period 1; 2) based on the calibrated H_R, the b and ω were calibrated using the V-pol TB, soil moisture, soil temperature, and VWC observations collected in Period 3; and 3) soil moisture was retrieved using the calibrated parameters from the first two steps and the V-pol TB observations collected in Period 2.

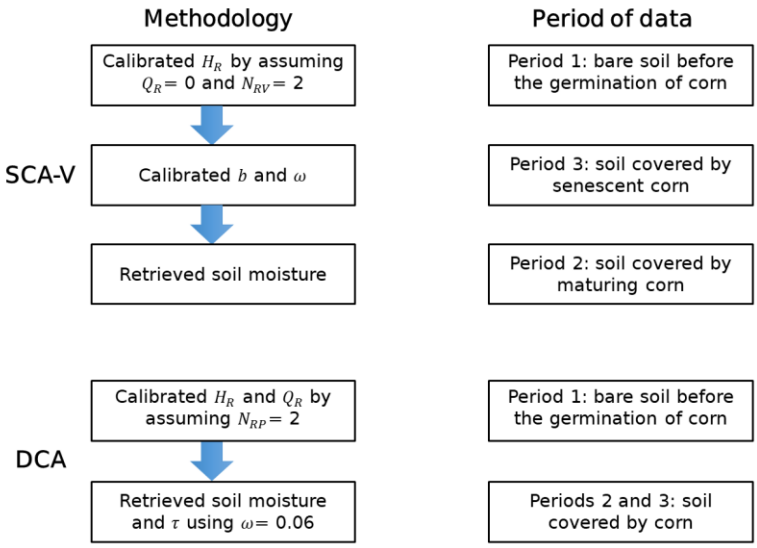

Figure 8-2: Diagram illustrating the methodology and period of data used in the SCA-V and the DCA.

In terms of the DCA, it was assumed that N_{RP}= 2 and ω= 0.06 as in the SMAP DCA implementation. Since τ was concurrently retrieved with soil moisture, only H_R and Q_R needed to be determined before the soil moisture retrieval. Consequently, a two-step approach was applied to calibrate the parameters and retrieve the soil moisture for the DCA (Figure 8-2): 1) calibrate H_R and Q_R using the data collected over Period 1; and 2) retrieve soil moisture and τ using the calibrated parameters from the first step and the dual-pol TB observations from Periods 2 and 3. The roughness parameters calibrated over the bare soil period were applied to the vegetation-covered soil period because the surface roughness was found to have little change throughout the entire period according to Figure 8-1d.

8.4 Results and Discussion

8.4.1 Single channel algorithm V-pol

Use of the SMAP SCA default parameters for croplands (Table 7-2) was first evaluated at V-pol TB over Periods 2 and 3 (result not shown), with the RMSE between the

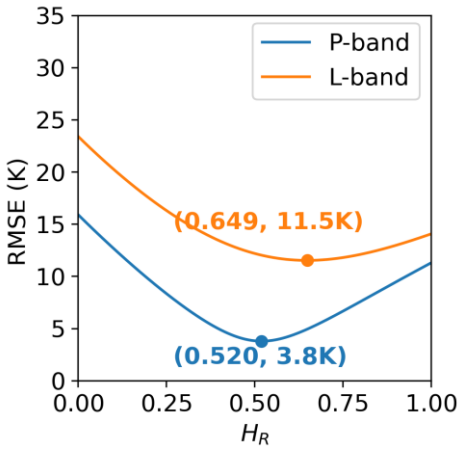

Figure 8-3: RMSE (K) between the observed and simulated V-pol TB for Period 1 using a range of H_R values. The semi-empirical model for bare soil (Eq. 4-4) was adopted as the forward model. The dots with values indicate the minimum RMSE and the corresponding H_R values for P-band (in blue) and L-band (in orange). The parameters Q_R and N_{RV} were assumed to be the same as in the SMAP SCA-V at both P- and L-band, being 0 and 2, respectively.

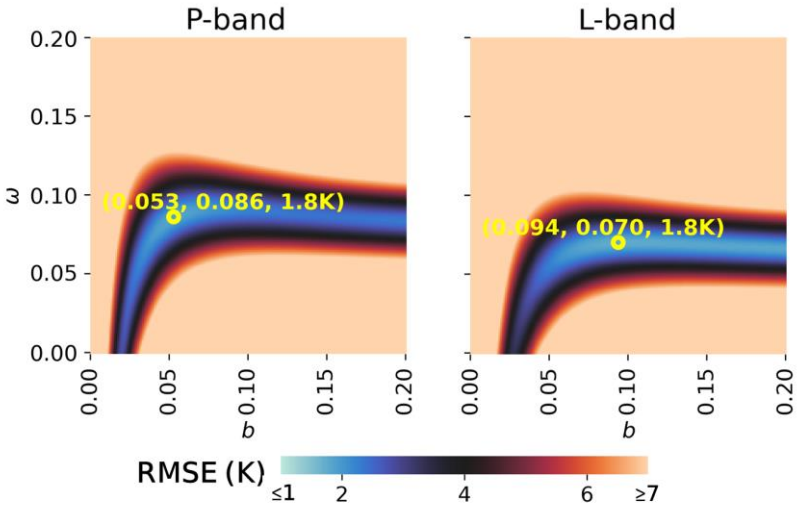

Figure 8-4: RMSE (K) between the observed and simulated TB using a range of b and ω values for P- and L-band V-pol over Period 3. The tau-omega model was adopted as the forward model. The yellow circles indicate where the minimum RMSE was reached, with the three values showing b, ω, and the minimum RMSE, respectively. The calibrated H_R values from Period 1, i.e., 0.520 and 0.649, were used for P- and L-band, respectively. The parameters Q_R and N_{RV} were assumed to be the same as in the SMAP SCA, being 0 and 2, respectively.

retrieved and measured soil moisture being extremely large (~0.5 m^3/m^3) at both P- and L-band. Consequently, the model parameters needed to be calibrated at this site.

In Figure 8-3, a range of H_R values were used to simulate the V-pol TB for P- and L-band using the semi-empirical model for bare soil (Eq. 4-4). The H_R values that produced the minimum RMSE between the simulated and observed TB were considered the optimum, marked as the dots with annotated values. Therefore, H_R was calibrated to be 0.520 and 0.649 at P- and L-band, respectively, with the calibration residuals being 3.8 K at P-band and 11.5 K at L-band.

In Figure 8-4, the soil moisture measurements collected over Period 3 were adopted to simulate TB, using the tau-omega model with calibrated H_R (Figure 8-3) and varying b and ω. As a result, b and ω were calibrated to be 0.053 and 0.086 for P-band and 0.094 and 0.070 for L-band. The calibration residual was 1.8 K at both P- and L-band. Soil moisture was subsequently retrieved at P- and L-band at V-pol using the tau-

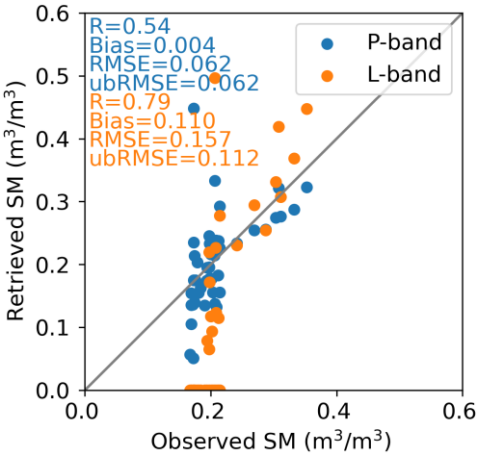

Figure 8-5: Observed versus retrieved soil moisture for Period 2 of the corn-covered soil, using the SCA-V with the tau-omega model. The calibrated H_R, b, and ω parameters were used here, i.e., H_R = 0.520, b = 0.053, and ω = 0.086 for P-band and H_R = 0.649, b = 0.094, and ω = 0.070 for L-band. The default SMAP SCA Q_R (= 0) and N_{RV} (= 2) were used for both P- and L-band.

omega model (Figure 8-5). Though the R at P-band (0.54) was slightly lower than at L-band (0.79), P-band performed better than L-band in all other metrics, particularly in RMSE, being 0.062 m^3/m^3 at P-band and 0.157 m^3/m^3 at L-band. While the RMSE/ubRMSE did not fulfill the 0.04-m^3/m^3 target accuracy of SMAP and SMOS even at P-band, the performance was acceptable considering that the VWC was as high as 20 kg/m^2. The RMSE/ubRMSE at L-band demonstrated the inability of the PLMR to sense the soil moisture underneath such a dense corn canopy.

Strikingly, Figure 8-5 presents some scatters with retrieved soil moisture of zero at L-band but not at P-band. After excluding these zero values from calculating the statistics, the RMSE at L-band was still much higher than at P-band, being 0.098 m^3/m^3 (not plotted). These zero values at L-band were mainly due to the different vegetation conditions for the calibration and validation datasets, with the VWC being up to ~15 and ~20 kg/m^2, respectively. When applying the calibrated vegetation parameters to the validation dataset at L-band, the modeled TB was lower than the observed TB even though the soil moisture was zero at the beginning of the retrieval iteration. Therefore, the soil moisture was bounded to be zero since an increase of soil moisture further

Table 8-1: Calibrated SCA-V vegetation parameters for the corn-covered flat soil over Periods 2 and 3.

Band	b	ω
P	0.062	0.086
L	0.065	0.063

decreases the modeled TB and thus enlarges the cost function. This phenomenon indicated that at L-band the calibrated parameters may not be transferred to applications with vegetation conditions substantially differing from the calibration dataset. However, the calibrated vegetation parameters at P-band were found to be applicable to broader conditions given the reduced vegetation impact.

Given the analysis above, a more comprehensive calibration was repeated using the data over Periods 2 and 3 (Table 8-1). Finally, the b and ω were calibrated to be 0.062 and 0.086 at P-band and 0.065 and 0.063 at L-band. Although these values were not used in this thesis, they will be useful for following studies on P-band in the future.

8.4.2 Dual channel algorithm

Similar to the SCA-V, the data collected in Period 1 were first used to calibrate the roughness parameters, i.e., H_R and Q_R at P- and L-band in the DCA approach (Table 8-2). The model for bare soil (Eq. 4-4) was adopted as the forward model, with N_{RP} assumed the same as in the SMAP DCA to be 2 at both P- and L-band. Subsequently, the DCA soil moisture retrieval was conducted using the calibrated H_R and Q_R in Table 8-2, with the comparison of the observed and retrieved soil moisture presented in Figure 8-6. P-band was found to perform better than L-band in all metrics, particularly in RMSE, being 0.079 m^3/m^3 at P-band and 0.111 m^3/m^3 at L-band.

Table 8-2: The calibrated DCA roughness parameters using the data for Period 1.

Band	H_R	Q_R
P	0.618	0.070
L	0.766	0.097

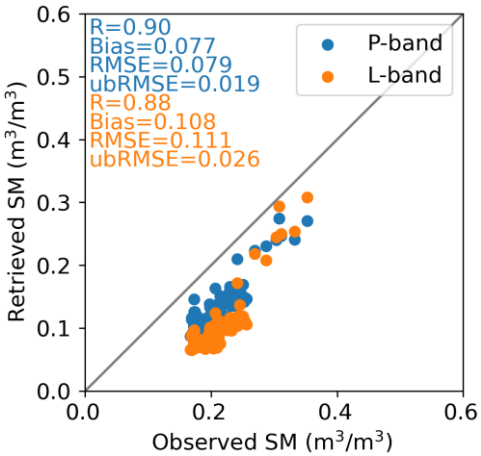

Figure 8-6: Observed versus retrieved soil moisture for Periods 2 and 3 of the corn-covered soil, using the DCA (Eq. 7-1) with the tau-omega model. The default SMAP DCA N_{RP} and ω were used for both P- and L-band, i.e., N_{RP} = 2 and ω = 0.06. The calibrated H_R and Q_R from Period 1 (Table 8-2) were used herein.

To understand the relationship between the vegetation impact and VWC, the VWC was plotted against MPDI for Periods 2 and 3 in Figure 8-7. All four quadrants were taken into account for establishing a more reliable relation between VWC and MPDI. MPDI characterizes the difference between H- and V-pol TB and was found to have a negative relationship with τ, and thus used in the LPRM to estimate τ (Owe et al.,

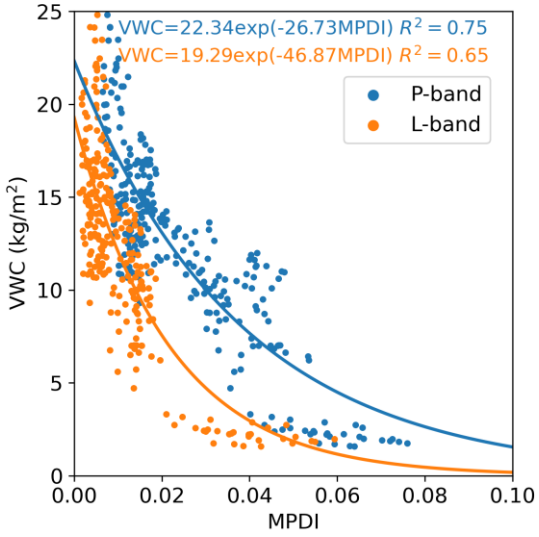

Figure 8-7: VWC against MPDI at P- and L-band for Periods 2 and 3 and all four quadrants.

2001). From Figure 8-7 it can be seen that the MPDI was higher at P-band than L-band for a given VWC, indicating the reduced vegetation impact at P-band.

Konings et al. (2015) pointed out that some redundant TB observations need to be provided for a robust soil moisture retrieval since the observations at different angles, polarizations, and times contain mutual information. From this perspective, MPDI can characterize the amount of the independent information contained at dual-polarized TB observations, and therefore P-band observations had a higher Degree of Information (DoI, Konings et al., 2015) than L-band observations according to the MPDI in Figure 8-7, possibly explaining the better retrieval accuracy at P-band. For VWC approaching 20 kg/m^2 and above, the MPDI at L-band was close to zero, which means that H- and V-pol observations did not contain useful independent information, while the MPDI at P-band was still around 0.01. In other words, the use of L-band dual-pol observations for such a high VWC added little information other than noise to the model.

Exponential relations between VWC and MPDI were established at P- and L-band utilizing the observations collected in all four quadrants, with a higher R^2 at P-band (0.75) than L-band (0.65) (Figure 8-7). These equations can be used to approximate the VWC at which P- or L-band becomes incapable of sensing the soil moisture beneath the canopy, meaning that the VWC thresholds would be around 17 and 12 kg/m^2 for P- and L-band, respectively, if 0.01 is selected as the cutoff in MPDI. However, these values should not be treated as definitive since they are also dependent on many other factors, i.e., moisture range, canopy structure, roughness, etc.

8.4.3 Model parameters across frequencies

Directly comparing the model parameters (i.e., H_R, Q_R, b, and ω) across different frequencies seems to be a straightforward way to judge the reduced roughness and vegetation impact at a specific frequency compared to others. However, this might not actually make sense. Gao et al. (2017) calibrated the H_R and b at L-, C- and X-band by assuming $\omega = 0.05$ and found H_R and b increased with increasing frequency. On the

contrary, Wang et al. (1983) discovered that H_R did not have a definitive relation to frequency. While Mo et al. (1982) obtained higher H_R and b values at C-band than those at L-band, consistent with Gao et al. (2017), they found ω was higher at L-band, being contradictory to microwave radiometry theory, which suggests that a longer wavelength band should have reduced scattering effects. Additionally, considering the results in this thesis (Figure 6-8, Figure 7-6, and Table 8-1) where no explicit frequency-dependence was found for the parameters H_R, b, and ω, it might be concluded that these model parameters should not be compared across different frequencies.

Two reasons can be attributed to the incomparability of those model parameters. First, the tau-omega and the HQN models are semi-empirical, approximating the rigorous physical process by linking the model parameters (i.e., H_R, b, and ω) to some measurable variables (e.g., RMS height, correlation length, and VWC). Meanwhile, many assumptions have been made to develop simplified analytical equations, including the homogeneity of soil moisture in space and with depth, the scattering isotropy of soil and vegetation, and the negligibility of the high-order scattering. Therefore, these parameters have to be considered as effective rather than physical (Wigneron et al., 2017).

Second, the mismatch between the sampling depth of the soil moisture measurements and the theoretical moisture retrieval depth may also lead to an incomparability of model parameters. The moisture retrieval depth is dependent on frequency and moisture profile and is thus a time-variant variable (Chapter 5), making it impractical to calibrate the model parameters using the soil moisture observations exactly within the moisture retrieval depth, let alone the challenge to measure the continuous soil moisture in a very thin layer, e.g., 1-2 cm. Due to the reasons above, it is suggested to compare the calibration residual and the retrieval performance for comparing the roughness and vegetation impact across different frequencies.

The Q_R was found to be a possible exception from both the literature and current results when estimated to be non-zero. Figure 7-6 and Table 8-2 present that the Q_R

values at P-band were lower than those at L-band. Similarly, Wang et al. (1983) has reported that while H_R is not correlated to frequency, such a relation exists for Q_R, being 0.01, 0.15, and 0.20 at 1.4, 5, and 10.7 GHz, respectively, for a soil surface with 0.73-cm RMS height. However, such a conclusion is drawn with much caution, given that relevant studies mostly assumed constant Q_R (Wigneron et al., 2001, Martens et al., 2015). It is suggested to include more frequencies in order to fully investigate this question in the future.

8.5 Chapter Summary

This chapter extended the evaluation of the tau-omega model at P- and L-band in Chapter 7 to a condition with much higher VWC, i.e., up to ~20 kg/m^2 for corn. Both the SCA-V and the DCA approaches demonstrated that P-band had a substantially better retrieval performance than L-band, indicating a reduced vegetation impact at P-band. While the RMSE at P-band was not low, i.e., 0.062 m^3/m^3 for the SCA-V and 0.079 m^3/m^3 for the DCA, this performance is considered acceptable given that the VWC achieved such a high value. Conversely, L-band was unable to sense the soil moisture underneath such a dense corn canopy, with RMSE higher than 0.1 m^3/m^3 for both the SCA-V and the DCA.

9 Conclusions, Contributions and Future Work

9.1 Conclusions

The main limitations of L-band soil moisture remote sensing are the relatively shallow moisture retrieval depth and the degraded accuracy in areas with great surface roughness and/or dense vegetation. Accordingly, this thesis analyzed data from a long-term tower-based experiment in Victoria, Australia, to determine whether using P-band can improve the representative depth and accuracy of retrieved soil moisture by taking advantage of its longer wavelength than L-band. Comprehensive model simulations and experimental observations have demonstrated the greater moisture retrieval depth and the reduced impact from surface roughness and the vegetation canopy at P-band compared to L-band using time-series data from 2019 to 2021, with various moisture, roughness, and vegetation conditions investigated. This research therefore paves the way for a future P-band radiometer-based mission for globally sensing deeper and more accurate soil moisture. Detailed conclusions for each analysis chapter are as follows.

9.1.1 Soil moisture retrieval depth

Chapter 5 compared the moisture retrieval depth of P- and L-band radiometry to demonstrate the potential of P-band for a future satellite mission with deeper subsurface moisture sensing. Theoretical simulations were first performed to predict the moisture retrieval depth with simulated soil profiles by equating the coherent and Fresnel emissivity. Empirical correlation analysis was then applied to the MPDI from observed brightness temperature and soil moisture measurements collected in the PRISM tower experiment over a flat bare soil.

For the same moisture retrieval depth, a higher correlation between soil moisture and MPDI was found at P-band than L-band, implying that P-band can either retrieve soil moisture over the same moisture retrieval depth as L-band (~5 cm) but with greater accuracy, or that a larger moisture retrieval depth (~7 cm) can be achieved while maintaining the same accuracy. These empirical findings were in line with model predictions. Additionally, predictions revealed that the moisture retrieval depth increased with wavelength, indicating that P-band can potentially provide soil moisture retrievals for a depth larger than 10 cm when using a frequency lower than 0.5 GHz. Importantly, model predictions showed that moisture retrieval depth was not only dependent on soil moisture content and observation frequency, but also on the moisture gradient of the profile.

9.1.2 Roughness impact of random and periodic surfaces

Chapter 6 compared random and periodic roughness impacts on P- and L-band passive microwave brightness temperature to demonstrate the potential improvement in soil moisture retrieval from using the longer wavelength P-band observations rather than the shorter L-band observations over flat and periodic soil. The Fraunhofer criterion and physical modeling indicated that TB observations at a longer wavelength should have a reduced impact from random roughness. A reduced impact from periodic roughness was also confirmed at P-band compared with L-band by the physical modeling. The semi-empirical model for bare soil was evaluated in this chapter and found to work better at P- than L-band, supported by the lower RMSE at P-band in the simulation results. The calibrated H_R in Q2 was applied to retrieve the soil moisture in all four quadrants, with the result showing that P-band had a reduced error compared to L-band. This evidence collectively confirms that P-band was less impacted by random and periodic roughness than L-band.

For bare flat and periodic soil surfaces, V-pol was less impacted by roughness impact than H-pol at both P- and L-band in terms of both TB simulation and soil moisture retrieval. Evaluating the SCA-V retrieval results showed that P-band had a more comparable RMSE across different surface roughness configurations than those at L-

band, with variations up to 0.012 and 0.022 m^3/m^3 for P- and L-band, respectively. Therefore, P-band did not need to have the periodic surfaces discriminated, while L-band needed differently calibrated parameters for bare periodic surfaces compared to bare flat surfaces.

9.1.3 Vegetation impact of wheat

Chapter 7 evaluated the tau-omega model over flat and periodic surfaces covered by wheat with VWC up to 4 kg/m^2 to demonstrate the potential improvement in soil moisture retrieval from using the longer wavelength P-band observations. The default SMAP SCA parameters for croplands were found to simulate TB satisfactorily at L-band V-pol but not at L-band H-pol or P-band. Therefore, at P-band V-pol, the roughness and vegetation parameters were calibrated for the flat-soil quadrant and applied to retrieve the soil moisture in all four quadrants, while the default SMAP parameters were applied to retrieve the soil moisture in all four quadrants at L-band V-pol. The RMSE between observed and retrieved soil moisture showed that neither P- or L-band had a substantial performance variation across different quadrants for the SCA or DCA.

Combining the findings for bare soil in Chapter 6, it can be concluded that P-band had a reduced roughness impact and was thus able to model both the flat and periodic soil using the calibrated parameters from the flat soil, for both bare and wheat-covered conditions. Conversely, L-band could only treat the different periodic surfaces like a flat surface when covered by a mature wheat canopy. Moreover, a lower RMSE at P-band (0.029 m^3/m^3) than L-band (0.063 m^3/m^3) was observed when omitting vegetation effects in the forward model, confirming that P-band observations were relatively unaffected by the wheat canopy. However, when using the SCA-V approach with the vegetation impact considered by the tau-omega model, the similar RMSE (~0.02 m^3/m^3) at P- and L-band did not demonstrate the expected improvement in soil moisture retrieval over the wheat-covered soil at P-band.

9.1.4 Vegetation impact of dense corn

Chapter 8 extended the investigation of vegetation impact to corn with VWC up to ~20 kg/m^2 so as to compare the retrieval performance at P- and L-band. Similar to Chapter 7, both the SCA-V and the DCA approaches were performed to retrieve the soil moisture. The default SMAP SCA-V parameters were found to work poorly over corn at both P- and L-band, motivating a local calibration of model parameters. Based on the calibrated parameters, the results from both approaches presented a substantially improved retrieval performance and a clear reduction in vegetation impact at P-band compared to L-band. While the RMSE at P-band was not low, i.e., 0.062 m^3/m^3 for the SCA-V and 0.079 m^3/m^3 for the DCA, this performance can be regarded as acceptable considering the extremely high VWC. Conversely, L-band failed to sense the soil moisture beneath such a dense corn canopy, with RMSE above 0.1 m^3/m^3 for both the SCA-V and the DCA.

9.2 Contributions

Portions of this thesis have been published in the following journal papers:

1. SHEN, X., WALKER, J. P., YE, N., WU, X., BOOPATHI, N., YEO, I.-Y., ZHANG, L. & ZHU, L. 2021. Soil moisture retrieval depth of P- and L-band radiometry: predictions and observations. IEEE Transactions on Geoscience and Remote Sensing, 59, 6814-6822.
2. SHEN, X., WALKER, J. P., YE, N., WU, X., BRAKHASI, F., BOOPATHI, N., ZHU, L., YEO, I.-Y., KIM, E., KERR, Y. & JACKSON, T. 2022. Impact of random and periodic surface roughness on P- and L-band radiometry. Remote Sensing of Environment, 269, 112825.
3. SHEN, X., WALKER, J. P., YE, N., WU, X., BRAKHASI, F., BOOPATHI, N., ZHU, L., YEO, I.-Y., KIM, E., KERR, Y. & JACKSON, T. 2022. Evaluation of the tau-omega model over bare and wheat-covered flat and periodic soil surfaces at P- and L-band. Remote Sensing of Environment, 273, 112960.

Contents of this thesis have been presented at the following international conferences:

1. SHEN, X., WALKER, J. P., YE, N., & WU, X. 2021. P-band microwave remote sensing for improved soil moisture retrieval. 24th International Congress on Modeling and Simulation (MODSIM), Sydney, Australia
2. SHEN, X., WALKER, J. P., YE, N., WU, X., BOOPATHI, N., ZHANG, L., ZHU, L., YEO, I.-Y., JACKSON, T., KERR, Y., KIM, E. & McGrath A. 2020. Moisture retrieval depths at P- and L-band. IEEE International Geoscience and Remote Sensing Symposium (IGARSS), Hawaii, USA
3. SHEN, X., WALKER, J. P., YE, N., WU, X., BOOPATHI, N., ZHANG, L., ZHU, L. & YEO, I.-Y. 2019. Soil moisture sensing depth at P- and L-band: simulations and observations. 23rd International Congress on Modeling and Simulation (MODSIM), Canberra, Australia

9.3 Future Work

While this thesis has demonstrated that P-band is a promising proposition to provide deeper and more accurate soil moisture information compared to the current L-band missions, there remain four challenges: aperture size, RFI, receiver design and calibration, and ionospheric and celestial emission effects (see Chapter 2.6). Nonetheless, it is encouraging to witness that the advancements in aerospace and remote sensing technologies, e.g., large deployable antennas, downscaling techniques, RFI mitigation techniques, etc., have been conquering these challenges and paving the way for a successful P-band mission in the near future. However, further investigation is recommended from the following aspects to accelerate the arrival of a successful P-band radiometer-based mission:

1. Extend the findings in this thesis to airborne experiments that can simulate a satellite-scale (i.e., tens of km) scenario. At satellite scale, the heterogeneous moisture, surface roughness and vegetation conditions within one footprint may or may not be averaged out. Therefore, the

demonstrated greater moisture retrieval depth and higher retrieval performance at P-band remain to be confirmed at satellite scale.

2. Compare the retrieval performance from using multi- and mono-angle observations to support the design of the future P-band mission. While taking more observations from different channels (i.e., polarization, incidence angle, frequency, etc.) is usually considered beneficial to soil moisture retrieval, noise will definitely be added to disturb the retrieval process at the same time. In some scenarios, more noise than useful information can be added to the model when trying to incorporate more observations. For example, substantially high roughness/vegetation can minimize the difference of the TB at different incidence angles and polarizations (see Figure 6-7 and Figure 8-7).

3. Incorporate radiometers at multiple frequencies (particularly below 500 MHz) to sense the soil moisture at different depths for retrieving soil moisture profiles. Providing soil moisture at a given depth has been falling behind the increasing demands of hydrological and climate applications. Since this thesis has demonstrated that the moisture retrieval depth increased as the increasing wavelength, retrieving moisture profiles can be realized by taking advantage of different frequencies.

4. Combine different remote sensing techniques (e.g., SAR and optical sensors) to enhance the coarse spatial resolution of P-band radiometers. If the same antenna size as SMAP is used on a P-band radiometer, the spatial resolution is expected to degrade to ~75 km from the 40 km of SMAP, which remains to be improved to fulfill the requirements of precision agriculture and other applications. Apart from utilizing a larger deployable antenna, a combination of other techniques with high spatial resolution can downscale the soil moisture dataset from the P-band radiometer.

References

ABELEN, S. & SEITZ, F. 2013. Relating satellite gravimetry data to global soil moisture products via data harmonization and correlation analysis. *Remote Sensing of Environment,* 136**,** 89-98.

AHMAD, S., KALRA, A. & STEPHEN, H. 2010. Estimating soil moisture using remote sensing data: A machine learning approach. *Advances in Water Resources,* 33**,** 69-80.

AL-YAARI, A., WIGNERON, J. P., KERR, Y., RODRIGUEZ-FERNANDEZ, N., O'NEILL, P. E., JACKSON, T. J., LANNOY, G. J. M. D., BITAR, A. A., MIALON, A. & RICHAUME, P. 2017. Evaluating soil moisture retrievals from ESA's SMOS and NASA's SMAP brightness temperature datasets. *Remote Sensing of Environment,* 193**,** 257-273.

AL BITAR, A., LEROUX, D., KERR, Y. H., MERLIN, O., RICHAUME, P., SAHOO, A. & WOOD, E. F. 2012. Evaluation of SMOS soil moisture products over continental US using the SCAN/SNOTEL network. *IEEE Transactions on Geoscience and Remote Sensing,* 50**,** 1572-1586.

ALEMOHAMMAD, S. H., JAGDHUBER, T., MOGHADDAM, M. & ENTEKHABI, D. 2019. Soil and vegetation scattering contributions in L-band and P-band polarimetric SAR observations. *IEEE Transactions on Geoscience and Remote Sensing,* 57**,** 8417-8429.

ALI, I., GREIFENEDER, F., STAMENKOVIC, J., NEUMANN, M. & NOTARNICOLA, C. 2015. Review of machine learning approaches for biomass and soil moisture retrievals from remote sensing data. *Remote Sensing,* 7**,** 16398-16421.

AN, R., ZHANG, L., WANG, Z., QUAYE-BALLARD, J. A., YOU, J., SHEN, X., GAO, W., HUANG, L., ZHAO, Y. & KE, Z. 2016. Validation of the ESA CCI soil moisture product in China. *International Journal of Applied Earth Observation and Geoinformation,* 48**,** 28-36.

ÅNGSTRÖM, A. 1925. The albedo of various surfaces of ground. *Geografiska Annaler,* 7**,** 323-342.

ATTEMA, E. & ULABY, F. T. 1978. Vegetation modeled as a water cloud. *Radio science,* 13**,** 357-364.

AUBERT, D., LOUMAGNE, C. & OUDIN, L. 2003. Sequential assimilation of soil moisture and streamflow data in a conceptual rainfall–runoff model. *Journal of Hydrology,* 280**,** 145-161.

BAGHDADI, N., PAILLOU, P., GRANDJEAN, G., DUBOIS, P. & DAVIDSON, M. 2000. Relationship between profile length and roughness variables for natural surfaces. *International Journal of Remote Sensing,* 21**,** 3375-3381.

BALENZANO, A., MATTIA, F., SATALINO, G. & DAVIDSON, M. W. 2010. Dense temporal series of C-and L-band SAR data for soil moisture retrieval over agricultural crops. *IEEE Journal of Selected Topics in Applied Earth Observations and Remote Sensing,* 4**,** 439-450.

BASHARINOV, A. Y. & SHUTKO, A. 1975. Simulation studies of the SHF radiation characteristics of soils under moist conditions.

BAYER, A., MAHBUB, I., CHAPPELL, M., RUTER, J. & VAN IERSEL, M. W. 2013. Water use and growth of Hibiscus acetosella 'Panama Red'grown with a soil moisture sensor-controlled irrigation system. *HortScience,* 48**,** 980-987.

BECK, H. E., PAN, M., MIRALLES, D. G., REICHLE, R. H., DORIGO, W. A., HAHN, S., SHEFFIELD, J., KARTHIKEYAN, L., BALSAMO, G. & PARINUSSA, R. M. 2021. Evaluation of 18 satellite-and model-based soil moisture products using in situ measurements from 826 sensors. *Hydrology and Earth System Sciences,* 25**,** 17-40.

BINDLISH, R., JACKSON, T. J., GASIEWSKI, A. J., KLEIN, M. & NJOKU, E. G. 2006. Soil moisture mapping and AMSR-E validation using the PSR in SMEX02. *Remote Sensing of Environment,* 103**,** 127-139.

BIRCHAK, J. R., GARDNER, C. G., HIPP, J. E. & VICTOR, J. M. 1974. High dielectric constant microwave probes for sensing soil moisture. *Proceedings of the IEEE,* 62**,** 93 - 98.

BIRCHER, S., BALLING, J. E., SKOU, N. & KERR, Y. H. 2012. Validation of SMOS brightness temperatures during the HOBE airborne campaign, western Denmark. *IEEE Transactions on Geoscience and Remote Sensing,* 50**,** 1468-1482.

BIRCHER, S., DEMONTOUX, F., RAZAFINDRATSIMA, S., ZAKHAROVA, E., DRUSCH, M., WIGNERON, J. P. & KERR, Y. H. 2016. L-band relative permittivity of organic soil surface layers—a new dataset of resonant cavity measurements and model evaluation. *Remote Sensing,* 8.

BIRCHER, S., MAHMOODI, A., MIALON, A., KERR, Y., DEMONTOUX, F., RAZAFINDRATSIMA, S., JONARD, F., RICHAUME, P., ANDREASEN, M. & WEIHERMÜLLER, L. 2015. SMOSHiLat: Improving our understanding of microwave L-band emissions from organic-rich soils in the northern cold climate zone and their impact on the SMOS soil moisture product. SMOS level 2 Soil Moisture Meeting.

BIRCHER, S., RICHAUME, P., MAHMOODI, A., MIALON, A., FERNANDEZ-MORAN, R., WIGNERON, J.-P., DEMONTOUX, F., JONARD, F., WEIHERMÜLLER, L. & ANDREASEN, M. Towards an improved soil moisture retrieval for organic-rich soils from SMOS passive microwave L-band observations. EGU General Assembly Conference Abstracts, 2017. 13342.

BLANCHARD, B. J. 1972. Measurements from aircraft to characterize watersheds. *4th Annual Earth Resources Program Review.* NASA, Lyndon B. Johnson Space Center, Houston, Tex.

BLINN, J. C. & QUADE, J. G. 1972. Microwave properties of geological materials: Studies of penetration depth and moisture effects. *4th Annual Earth Resources Program Review.* NASA, Lyndon B. Johnson Space Center, Houston, Tex.

BLONQUIST JR, J., JONES, S. B. & ROBINSON, D. 2005. A time domain transmission sensor with TDR performance characteristics. *Journal of Hydrology,* 314**,** 235-245.

BOGENA, H. R., HUISMAN, J. A., GÜNTNER, A., HÜBNER, C., KUSCHE, J., JONARD, F., VEY, S. & VEREECKEN, H. 2015. Emerging methods for noninvasive sensing of soil moisture dynamics from field to catchment scale: A review. *Wiley Interdisciplinary Reviews: Water,* 2**,** 635-647.

BORN, M. & WOLF, E. 1964. Principles of optics. Second (revised) edition. *Macmillan Co., New York,* 12**,** 124.

BRACAGLIA, M., FERRAZZOLI, P. & GUERRIERO, L. 1995. A fully polarimetric multiple scattering model for crops. *Remote Sensing of Environment,* 54**,** 170-179.

BROCCA, L., PONZIANI, F., MORAMARCO, T., MELONE, F., BERNI, N. & WAGNER, W. 2012. Improving landslide forecasting using ASCAT-derived soil moisture data: A case study of the Torgiovannetto landslide in central Italy. *Remote Sensing,* 4**,** 1232-1244.

BURGIN, M., CLEWLEY, D., LUCAS, R. M. & MOGHADDAM, M. 2011. A generalized radar backscattering model based on wave theory for multilayer multispecies vegetation. *IEEE Transactions on Geoscience and Remote Sensing,* 49**,** 4832-4845.

BURKE, W., SCHMUGGE, T. & PARIS, J. 1979. Comparison of 2.8- and 21-cm microwave radiometer observations over soils with emission model calculations. *Journal of Geophysical Research: Oceans,* 84**,** 287-294.

CÁCERES, M. D., VILALTA, J. M., COLL, L., LLORENS, P., CASALS, P., POYATOS, R., PAUSAS, J. G. & BROTONS, L. 2015. Coupling a water balance model with forest inventory data to predict drought stress. *Agricultural and Forest Meteorology,* 213**,** 77-90.

CAMPBELL, G., CALISSENDORFF, C. & WILLIAMS, J. 1991. Probe for measuring soil specific heat using a heat-pulse method. *Soil Science Society of America Journal,* 55**,** 291-293.

CAMPBELL, G. S. & ANDERSON, R. Y. 1998. Evaluation of simple transmission line oscillators for soil moisture measurement. *Computers and Electronics in Agriculture,* 20**,** 31-44.

CAMPS, A., PARK, H. & GONZALEZ-GAMBAU, V. An imaging algorithm for synthetic aperture interferometric radiometers with built-in RFI mitigation. 2014 13th Specialist Meeting on Microwave Radiometry and Remote Sensing of the Environment (MicroRad), 2014. IEEE, 39-43.

CANO, A., SALEH, K., WIGNERON, J.-P., ANTOLÍN, C., BALLING, J. E., KERR, Y. H., KRUSZEWSKI, A., MILLÁN-SCHEIDING, C., SØBJÆRG, S. S., SKOU, N. & LÓPEZ-BAEZA, E. 2010. The SMOS mediterranean ecosystem L-band characterisation experiment (MELBEX-I) over natural shrubs. *Remote Sensing of Environment,* 114**,** 844-853.

CHAN, S. K., BINDLISH, R., O'NEILL, P. E., NJOKU, E., JACKSON, T., COLLIANDER, A., CHEN, F., BURGIN, M., DUNBAR, S. & PIEPMEIER, J. 2016. Assessment of the SMAP Passive Soil Moisture Product. *IEEE Transactions on Geoscience and Remote Sensing,* 54**,** 4994-5007.

CHAPIN, E., CHAU, A., CHEN, J., HEAVEY, B., HENSLEY, S., LOU, Y., MACHUZAK, R., MOGHADDAM, M. & IEEE 2012. AirMOSS: An Airborne P-band SAR to Measure Root-Zone Soil Moisture. *2012 IEEE Radar Conference.*

CHEN, K.-S., WU, T.-D., TSANG, L., LI, Q., SHI, J. & FUNG, A. K. 2003. Emission of rough surfaces calculated by the integral equation method with comparison to three-dimensional moment method simulations. *IEEE Transactions on Geoscience and Remote Sensing,* 41**,** 90-101.

CHEN, L., XING, M., HE, B., WANG, J., SHANG, J., HUANG, X. & XU, M. 2021. Estimating soil moisture over winter wheat fields during growing season using machine-learning methods. *IEEE Journal of Selected Topics in Applied Earth Observations and Remote Sensing,* 14**,** 3706-3718.

CHEN, Y. & OR, D. 2006. Effects of Maxwell - Wagner polarization on soil complex dielectric permittivity under variable temperature and electrical conductivity. *Water Resources Research,* 42**,** 770-775.

CHIFFLARD, P., KRANL, J., ZUR STRASSEN, G. & ZEPP, H. 2018. The significance of soil moisture in forecasting characteristics of flood events. A statistical analysis in two nested catchments. *Journal of Hydrology and Hydromechanics,* 66**,** 1-11.

CHOUDHURY, B. J., SCHMUGGE, T. J., CHANG, A. & NEWTON, R. W. 1979. Effect of surface roughness on the microwave emission from soils. *Journal of Geophysical Research: Oceans,* 84**,** 5699-5706.

CHOUDHURY, B. J., SCHMUGGE, T. J. & MO, T. 1982. A parameterization of effective soil temperature for microwave emission. *Journal of Geophysical Research: Oceans,* 87**,** 1301–1304.

COLLIANDER, A., COSH, M. H., MISRA, S., JACKSON, T. J., CROW, W. T., CHAN, S., BINDLISH, R., CHAE, C., COLLINS, C. H. & YUEH, S. H. 2017a. Validation and scaling of soil moisture in a semi-arid environment: SMAP validation experiment 2015 (SMAPVEX15). *Remote Sensing of Environment,* 196**,** 101-112.

COLLIANDER, A., JACKSON, T. J., BINDLISH, R., CHAN, S., DAS, N., KIM, S., COSH, M., DUNBAR, R., DANG, L. & PASHAIAN, L. 2017b. Validation of SMAP surface soil moisture products with core validation sites. *Remote Sensing of Environment,* 191**,** 215-231.

CONEL, J. E. 1970. Microwave emission from granular silicates-Determination of the absorption coefficient from plate measurements and the effects of scattering. *Technical Memorandum 33-458.* Jet Propulsion Laboratory, California Institute of Technology, Pasadena, California.

COUNCIL, N. R. 2010. *Spectrum management for science in the 21st century*, National Academies Press.

CROW, W. T., BERG, A. A., COSH, M. H., LOEW, A., MOHANTY, B. P., PANCIERA, R., DE ROSNAY, P., RYU, D. & WALKER, J. P. 2012. Upscaling sparse ground-based soil moisture observations for the validation of coarse-resolution satellite soil moisture products. *Reviews of Geophysics,* 50.

CROW, W. T., MILAK, S., MOGHADDAM, M., TABATABAEENEJAD, A., JARUWATANADILOK, S., YU, X., SHI, Y., REICHLE, R. H., HAGIMOTO, Y. & CUENCA, R. H. 2018. Spatial and temporal variability of root-zone soil moisture acquired from hydrologic modeling and AirMOSS P-band radar. *IEEE Journal of Selected Topics in Applied Earth Observations and Remote Sensing,* 11**,** 4578-4590.

DAS, N. N., ENTEKHABI, D., DUNBAR, R. S., CHAUBELL, M. J., COLLIANDER, A., YUEH, S., JAGDHUBER, T., CHEN, F., CROW, W. & O'NEILL, P. E. 2019. The SMAP and Copernicus Sentinel 1A/B microwave active-passive high resolution surface soil moisture product. *Remote Sensing of Environment,* 233**,** 111380.

DAS, N. N., ENTEKHABI, D., DUNBAR, R. S., COLLIANDER, A., CHEN, F., CROW, W., JACKSON, T. J., BERG, A., BOSCH, D. D. & CALDWELL, T. 2018. The SMAP mission combined active-passive soil moisture product at 9 km and 3 km spatial resolutions. *Remote Sensing of Environment,* 211**,** 204-217.

DAS, N. N., ENTEKHABI, D., KIM, S., YUEH, S. & O'NEILL, P. Combining SMAP and Sentinel data for high-resolution Soil Moisture product. 2016 IEEE International Geoscience and Remote Sensing Symposium (IGARSS), 2016. IEEE, 129-131.

DAVIS, J. & CHUDOBIAK, W. 1975. In situ meter for measuring relative permittivity of soils. *Geol. Surv. Can. Pap,* 75**,** 75-79.

DE JEU, R. A., HOLMES, T. R., PANCIERA, R. & WALKER, J. P. 2009. Parameterization of the land parameter retrieval model for L-band observations using the NAFE'05 data set. *IEEE Geoscience and Remote Sensing Letters,* 6**,** 630-634.

DE JEU, R. A. M., WAGNER, W., HOLMES, T. R. H., DOLMAN, A. J., VAN DE GIESEN, N. C. & FRIESEN, J. 2008. Global soil moisture patterns observed by space borne microwave radiometers and scatterometers. *Surveys in Geophysics,* 29**,** 399-420.

DENTE, L., FERRAZZOLI, P., SU, Z., VAN DER VELDE, R. & GUERRIERO, L. 2014. Combined use of active and passive microwave satellite data to constrain a discrete scattering model. *Remote sensing of environment,* 155**,** 222-238.

DOBSON, M. C., ULABY, F. T., HALLIKAINEN, M. T. & EL-RAYES, M. A. 1985. Microwave dielectric behavior of wet soil-part II: Dielectric mixing models. *IEEE Transactions on Geoscience and Remote Sensing,* GE-23**,** 35-46.

DORIGO, W., WAGNER, W., ALBERGEL, C., ALBRECHT, F., BALSAMO, G., BROCCA, L., CHUNG, D., ERTL, M., FORKEL, M. & GRUBER, A. 2017a. ESA CCI Soil Moisture for improved Earth system understanding: State-of-the art and future directions. *Remote Sensing of Environment,* 203**,** 185-215.

DORIGO, W. A., CHUNG, D., GRUBER, A., HAHN, S., MISTELBAUER, T., PARINUSSA, R. M., REIMER, C., VAN DER SCHALIE, R., DE JEU, R. A. M. & WAGNER, W. 2017b. Soil moisture [in: "state of the climate in 2016"]. *Bulletin of the American Meteorological Society,* 98**,** S30-S32.

DORIGO, W. A., GRUBER, A., DE JEU, R. A. M., WAGNER, W., STACKE, T., LOEW, A., ALBERGEL, C., BROCCA, L., CHUNG, D., PARINUSSA, R. M. & KIDD, R. 2015. Evaluation of the ESA CCI soil moisture product using ground-based observations. *Remote Sensing of Environment,* 162**,** 380-395.

DORIGO, W. A., WAGNER, W., HOHENSINN, R., HAHN, S., PAULIK, C., XAVER, A., GRUBER, A., DRUSCH, M., MECKLENBURG, S., VAN OEVELEN, P., ROBOCK, A. & JACKSON, T. 2011. The International Soil Moisture Network: a data hosting facility for global in situ soil moisture measurements. *Hydrology and Earth System Sciences,* 15**,** 1675-1698.

DRUSCH, M., HOLMES, T., ROSNAY, P. D. & BALSAMO, G. 2009. Comparing ERA-40-based L-band brightness temperatures with skylab observations: A calibration/validation study using the community microwave emission model. *Journal of Hydrometeorology,* 10**,** 213-226.

DUBOIS-FERNANDEZ, P., DU PLESSIS, O. R., LE COZ, D., DUPAS, J., VAIZAN, B., DUPUIS, X., CANTALLOUBE, H., COULOMBEIX, C., TITIN-SCHNAIDER, C. & DREUILLET, P. The onera ramses sar system. 2002 IEEE International Geoscience and Remote Sensing Symposium (IGARSS), 2002. IEEE, 1723-1725.

DUBOIS, P. C., VAN ZYL, J. & ENGMAN, T. 1995. Measuring soil moisture with imaging radars. *IEEE Transactions on Geoscience and Remote Sensing,* 33**,** 915-926.

EBTEHAJ, A. & BRAS, R. L. 2019. A physically constrained inversion for high-resolution passive microwave retrieval of soil moisture and vegetation water content in L-band. *Remote Sensing of Environment,* 233**,** 111346.

ENTEKHABI, D., NJOKU, E. G., O'NEILL, P. E., KELLOGG, K. H., CROW, W. T., EDELSTEIN, W. N., ENTIN, J. K., GOODMAN, S. D., JACKSON, T. J., JOHNSON, J., KIMBALL, J., PIEPMEIER, J. R., KOSTER, R. D., MARTIN, N., MCDONALD, K. C., MOGHADDAM, M., MORAN, S., REICHLE, R., SHI, J. C., SPENCER, M. W., THURMAN, S. W., TSANG, L. & VAN ZYL, J. 2010. The Soil Moisture Active Passive (SMAP) Mission. *Proceedings of the IEEE,* 98**,** 704-716.

ENTEKHABI, D., YUEH, S., O'NEILL, P. E., KELLOGG, K. H., ALLEN, A., BINDLISH, R., BROWN, M., CHAN, S., COLLIANDER, A. & CROW, W. T. 2014. SMAP handbook–Soil Moisture Active Passive: Mapping soil moisture and freeze/thaw from space.

ESA 2017. SMOS data products. https://earth.esa.int/documents/10174/1854456/SMOS-Data-Products-Brochure.

ESCORIHUELA, M. J., CHANZY, A., WIGNERON, J. P. & KERR, Y. H. 2010. Effective soil moisture sampling depth of L-band radiometry: A case study. *Remote Sensing of Environment,* 114**,** 995-1001.

ESCORIHUELA, M. J., KERR, Y. H., ROSNAY, P. D., WIGNERON, J. P., CALVET, J. C. & LEMAITRE, F. 2007. A simple model of the bare soil microwave emission at L-band. *IEEE Transactions on Geoscience and Remote Sensing,* 45**,** 1978-1987.

ETMINAN, A., TABATABAEENEJAD, A. & MOGHADDAM, M. 2020. Retrieving root-zone soil moisture profile from P-band radar via hybrid global and local optimization. *IEEE Transactions on Geoscience and Remote Sensing,* 58**,** 5400-5408.

FAGERLUND, E., KLEMAN, B., SELLIN, L. & SVENSSON, H. 1970. Physical studies of nature by thermal mapping. *Earth-Science Reviews,* 6**,** 169-180.

FERNANDEZ-MORAN, R., WIGNERON, J. P., LOPEZ-BAEZA, E., AL-YAARI, A., COLL-PAJARON, A., MIALON, A., MIERNECKI, M., PARRENS, M., SALGADO-HERNANZ, P. M. & SCHWANK, M. 2015. Roughness and vegetation parameterizations at L-band for soil moisture retrievals over a vineyard field. *Remote Sensing of Environment,* 170**,** 269-279.

FERRAZZOLI, P. & GUERRIERO, L. 1995. Radar sensitivity to tree geometry and woody volume: A model analysis. *IEEE Transactions on Geoscience and Remote Sensing,* 33**,** 360-371.

FERRAZZOLI, P. & GUERRIERO, L. 1996. Passive microwave remote sensing of forests: A model investigation. *IEEE Transactions on Geoscience and Remote Sensing,* 34**,** 433-443.

FERRAZZOLI, P., GUERRIERO, L. & WIGNERON, J. P. 2002. Simulating L-band emission of forests in view of future satellite applications. *IEEE Transactions on Geoscience and Remote Sensing,* 40**,** 2700-2708.

FREEMAN, A., SHEN, Y. & WERNER, C. L. 1990. Polarimetric SAR calibration experiment using active radar calibrators. *IEEE Transactions on Geoscience and Remote Sensing,* 28**,** 224-240.

FUNG, A. & KUO, N. 2006. Backscattering from multi-scale and exponentially correlated surfaces. *Journal of Electromagnetic Waves and Applications,* 20**,** 3-11.

FUNG, A. K. 1994. Microwave scattering and emission models and their applications.

FUNG, A. K., LI, Z. & CHEN, K. S. 1992. Backscattering from a randomly rough dielectric surface. *IEEE Transaction on Geoscience & Remote Sensing,* 30**,** 356-369.

FUNG, A. K., LIU, W. Y., CHEN, K. S. & TSAY, M. K. 2002. An improved IEM model for bistatic scattering from rough surfaces. *Journal of Electromagnetic Waves & Applications,* 16**,** 689-702.

GAO, B.-C. 1996. NDWI—A normalized difference water index for remote sensing of vegetation liquid water from space. *Remote Sensing of Environment,* 58**,** 257-266.

GAO, L., CHAUBELL, M., SADEGHI, M. & WIGNERON, J.-P. 2021. Reappraisal of SMAP inversion algorithms for soil moisture and vegetation optical depth. *Remote Sensing of Environment,* 264**,** 112627.

GAO, L., SADEGHI, M., FELDMAN, A. F. & EBTEHAJ, A. 2020. A spatially constrained multichannel algorithm for inversion of a first-order microwave emission model at L-band. *IEEE Transactions on Geoscience and Remote Sensing,* 58**,** 8134-8146.

GAO, Y. 2016. *Joint active passive microwave soil moisture retrieval.* Monash University.

GAO, Y., COLLIANDER, A., BURGIN, M. S., WALKER, J. P., CHAE, C., DINNAT, E. & COSH, M. H. Multi-frequency radiometer-based soil moisture retrieval algorithm parametrization using in situ validation sites. 2017 IEEE International Geoscience and Remote Sensing Symposium (IGARSS), 2017. IEEE, 3945-3948.

GAO, Y., WALKER, J. P., YE, N., PANCIERA, R., MONERRIS, A., RYU, D., RÜDIGER, C. & JACKSON, T. J. 2018. Evaluation of the tau–omega model for passive microwave soil moisture retrieval using SMAPEx datasets. *IEEE Journal of Selected Topics in Applied Earth Observations and Remote Sensing,* 11**,** 888-895.

GAO, Z., XU, X., WANG, J., YANG, H., HUANG, W. & FENG, H. 2013. A method of estimating soil moisture based on the linear decomposition of mixture pixels. *Mathematical & Computer Modelling,* 58**,** 606-613.

GARRISON, J., SHAH, R., NOLD, B., MANSELL, J., VEGA, M., RAYMOND, J., BINDLISH, R., KURUM, M., PIEPMEIER, J. & KIM, S. SNOOPI: Demonstrating P-band reflectometry from orbit. 2021 IEEE International Geoscience and Remote Sensing Symposium (IGARSS), 2021. IEEE, 164-167.

GASKIN, G. J. & MILLER, J. D. 1996. Measurement of soil water content using a simplified impedance measuring technique. *Journal of Agricultural Engineering Research,* 63**,** 153-159.

GHULAM, A., QIN, Q., TEYIP, T. & LI, Z. L. 2007. Modified perpendicular drought index (MPDI): a real-time drought monitoring method. *ISPRS Journal of Photogrammetry and Remote Sensing,* 62**,** 150-164.

GIRALDEZ, A. E. Saocom-1 Argentina L band SAR mission overview. Coastal and Marine Applications of SAR Symp, 2003.

GRANT, J. P., GRIEND, A. A. V. D., WIGNERON, J. P., SALEH, K., PANCIERA, R. & WALKER, J. P. 2010. Influence of forest cover fraction on L-band soil moisture retrievals from heterogeneous pixels using multi-angular observations. *Remote Sensing of Environment,* 114**,** 1026-1037.

GRIEND, A. A. V. D., CAMILLO, P. J. & GURNEY, R. J. 1985. Discrimination of soil physical parameters, thermal inertia, and soil moisture from diurnal surface temperature fluctuations. *Water Resources Research,* 21**,** 997-1009.

GUERRIERO, L., FERRAZZOLI, P., VITTUCCI, C., RAHMOUNE, R., AURIZZI, M. & MATTIONI, A. 2016. L-band passive and active signatures of vegetated soil: Simulations with a unified model. *IEEE Journal of Selected Topics in Applied Earth Observations and Remote Sensing,* 9**,** 2520-2531.

HALLIKAINEN, M. T., ULABY, F. T., DOBSON, M. C., ELRAYES, M. A. & WU, L. 1985. Microwave dielectric behavior of wet soil-part 1: Empirical models and experimental observations. *IEEE Transactions on Geoscience and Remote Sensing,* GE-23**,** 25-34.

HE, L., HONG, Y., WU, X., YE, N., WALKER, J. P. & CHEN, X. 2018. Investigation of SMAP active–passive downscaling algorithms using combined Sentinel-1 SAR and SMAP radiometer data. *IEEE Transactions on Geoscience and Remote Sensing,* 56**,** 4906-4918.

HOEKSTRA, P. & DELANEY, A. 1974. Dielectric properties of soils at UHF and microwave frequencies. *Journal of Geophysical Research,* 79**,** 1699-1708.

HOLMES, T. R. H., ROSNAY, P. D., JEU, R. D., WIGNERON, R. J. P., KERR, Y., CALVET, J. C., ESCORIHUELA, M. J., SALEH, K. & LEMAîTRE, F. 2006. A new parameterization of the effective temperature for L band radiometry. *Geophysical Research Letters,* 33**,** 359-377.

HORN, R. The dlr airborne sar project e-sar. 1996 IEEE International Geoscience and Remote Sensing Symposium (IGARSS), 1996. IEEE, 1624-1628.

HORN, R., NOTTENSTEINER, A., REIGBER, A., FISCHER, J. & SCHEIBER, R. F-SAR—DLR's new multifrequency polarimetric airborne SAR. 2009 IEEE International Geoscience and Remote Sensing Symposium (IGARSS), 2009. IEEE, II-902-II-905.

HORNBUCKLE, B. & ENGLAND, A. 2004. Radiometric sensitivity to soil moisture at 1.4 GHz through a corn crop at maximum biomass. *Water Resources Research,* 40.

HUANG, S. & TSANG, L. 2012. Electromagnetic scattering of randomly rough soil surfaces based on numerical solutions of Maxwell equations in three-dimensional simulations using a hybrid UV/PBTG/SMCG method. *IEEE Transactions on Geoscience and Remote Sensing,* 50**,** 4025-4035.

HUANG, S., TSANG, L., NJOKU, E. G. & CHAN, K. S. 2010. Backscattering coefficients, coherent reflectivities, and emissivities of randomly rough soil surfaces at L-band for SMAP applications based on numerical solutions of Maxwell equations in three-

dimensional simulations. *IEEE Transactions on Geoscience and Remote Sensing,* 48**,** 2557-2568.

HUANG, Y., LIAO, G., LI, J. & XU, J. 2018. Narrowband RFI suppression for SAR system via fast implementation of joint sparsity and low-rank property. *IEEE Transactions on Geoscience and Remote Sensing,* 56**,** 2748-2761.

HUNT, K. M. & TURNER, A. G. 2017. The effect of soil moisture perturbations on Indian monsoon depressions in a numerical weather prediction model. *Journal of Climate,* 30**,** 8811-8823.

ITU 2015. International Telecommunication Union recommendation: Radio noise. ITU-R P.372-12.

JACKSON, R., IDSO, S. & REGINATO, R. 1976. Calculation of evaporation rates during the transition from energy - limiting to soil - limiting phases using albedo data. *Water Resources Research,* 12**,** 23-26.

JACKSON, T. J. 1993. III. Measuring surface soil moisture using passive microwave remote sensing. *Hydrological Processes,* 7**,** 139–152.

JACKSON, T. J., BINDLISH, R., COSH, M. H., ZHAO, T., STARKS, P. J., BOSCH, D. D., SEYFRIED, M., MORAN, M. S., GOODRICH, D. C. & KERR, Y. H. 2011. Validation of Soil Moisture and Ocean Salinity (SMOS) soil moisture over watershed networks in the US. *IEEE Transactions on Geoscience and Remote Sensing,* 50**,** 1530-1543.

JACKSON, T. J., LE VINE, D. M., GRIFFIS, A. J., GOODRICH, D. C., SCHMUGGE, T. J., SWIFT, C. T. & O'NEILL, P. E. 1993. Soil moisture and rainfall estimation over a semiarid environment with the ESTAR microwave radiometer. *IEEE Transactions on Geoscience and Remote Sensing,* 31**,** 836-841.

JACKSON, T. J., LE VINE, D. M., SWIFT, C. T., SCHMUGGE, T. J. & SCHIEBE, F. R. 1995. Large area mapping of soil moisture using the ESTAR passive microwave radiometer in Washita'92. *Remote Sensing of Environment,* 54**,** 27-37.

JACKSON, T. J. & O'NEILL, P. E. 1990. Attenuation of soil microwave emission by corn and soybeans at 1.4 and 5 GHz. *IEEE Transactions on Geoscience and Remote Sensing,* 28**,** 978-980.

JACKSON, T. J. & SCHMUGGE, T. J. 1991. Vegetation effects on the microwave emission of soils. *Remote Sensing of Environment,* 36**,** 203-212.

JACKSON, T. J., SCHMUGGE, T. J. & WANG, J. R. 1982. Passive microwave sensing of soil moisture under vegetation canopies. *Water Resources Research,* 18**,** 1137-1142.

JAEGER, J. Conduction of heat in a solid with periodic boundary conditions, with an application to the surface temperature of the moon. Mathematical Proceedings of the Cambridge Philosophical Society, 1953. Cambridge University Press, 355-359.

JIANG, T., ZHAO, K., ZHENG, X., CHEN, S. & WAN, X. 2019. Dynamic bp in the L band and its role in improving the accuracy of soil moisture retrieval. *Chinese Geographical Science,* 29**,** 283-292.

JIN, R., LI, Q. & LIU, H. 2019. A subspace algorithm to mitigate energy unknown RFI for synthetic aperture interferometric radiometer. *IEEE Transactions on Geoscience and Remote Sensing,* 58**,** 227-237.

JOHANNSEN, C. J. 1970. *The detection of available soil moisture by remote sensing techniques.* Purdue University.

JOHNSON, J. T., JEZEK, K. C., AKSOY, M., BRINGER, A., YARDIM, C., ANDREWS, M., CHEN, C.-C., BELGIOVANE, D., LEUSKI, V. & DURAND, M. The Ultra-wideband Software-Defined Radiometer (UWBRAD) for ice sheet internal temperature sensing: Results from recent observations. 2016 IEEE International Geoscience and Remote Sensing Symposium (IGARSS), 2016. IEEE, 7085-7087.

JOHNSON, J. T., JEZEK, K. C., MACELLONI, G., BROGIONI, M., TSANG, L., DINNAT, E. P., WALKER, J. P., YE, N., MISRA, S. & PIEPMEIER, J. R. 2021. Microwave radiometry at frequencies from 500 to 1400 MHz: An emerging technology for earth observations. *IEEE Journal of Selected Topics in Applied Earth Observations and Remote Sensing,* 14**,** 4894-4914.

KANKAKU, Y., SAGISAKA, M. & SUZUKI, S. PALSAR-2 launch and early orbit status. 2014 IEEE International Geoscience and Remote Sensing Symposium (IGARSS), 2014. IEEE, 3410-3412.

KARTHIKEYAN, L., PAN, M., WANDERS, N., KUMAR, D. N. & WOOD, E. F. 2017a. Four decades of microwave satellite soil moisture observations: Part 1. A review of retrieval algorithms. *Advances in Water Resources,* 109**,** 106-120.

KARTHIKEYAN, L., PAN, M., WANDERS, N., KUMAR, D. N. & WOOD, E. F. 2017b. Four decades of microwave satellite soil moisture observations: Part 2. Product validation and inter-satellite comparisons. *Advances in Water Resources*.

KERR, Y. H., AL-YAARI, A., RODRIGUEZ-FERNANDEZ, N., PARRENS, M., MOLERO, B., LEROUX, D., BIRCHER, S., MAHMOODI, A., MIALON, A. & RICHAUME, P. 2016. Overview of SMOS performance in terms of global soil moisture monitoring after six years in operation. *Remote Sensing of Environment,* 180**,** 40-63.

KERR, Y. H., WALDTEUFEL, P., RICHAUME, P., FERRAZZOLI, P. & WIGNERON, J. P. 2017. Algorithm Theoretical Basis Document (ATBD) for the SMOS Level 2 Soil Moisture Processor Development Continuation Project v3.10. https://earth.esa.int/documents/10174/1854519/SMOS_L2_SM_ATBD: SM-ESL (CBSA).

KERR, Y. H., WALDTEUFEL, P., RICHAUME, P., FERRAZZOLI, P. & WIGNERON, J. P. 2019. Algorithm theoretical basis document (ATBD) for the SMOS level 2 soil moisture processor development continuation project v4.0.

https://earth.esa.int/eogateway/documents/20142/37627/SMOS-L2-SM-ATBD.pdf: SM-ESL (CBSA).

KERR, Y. H., WALDTEUFEL, P., WIGNERON, J.-P., DELWART, S., CABOT, F., BOUTIN, J., ESCORIHUELA, M.-J., FONT, J., REUL, N., GRUHIER, C., JUGLEA, S. E., DRINKWATER, M. R., HAHNE, A., MARTIN-NEIRA, M. & MECKLENBURG, S. 2010. The SMOS mission: New tool for monitoring key elements of the global water cycle. *Proceedings of the IEEE,* 98**,** 666-687.

KILIC, L., PRIGENT, C., AIRES, F., BOUTIN, J., HEYGSTER, G., TONBOE, R. T., ROQUET, H., JIMENEZ, C. & DONLON, C. 2018. Expected performances of the Copernicus Imaging Microwave Radiometer (CIMR) for an all - weather and high spatial resolution estimation of ocean and sea ice parameters. *Journal of Geophysical Research: Oceans,* 123**,** 7564-7580.

KIM, S.-B., TSANG, L., JOHNSON, J. T., HUANG, S., VAN ZYL, J. J. & NJOKU, E. G. 2011. Soil moisture retrieval using time-series radar observations over bare surfaces. *IEEE Transactions on Geoscience and Remote Sensing,* 50**,** 1853-1863.

KIRDIASHEV, K. P., CHUKHLANTSEV, A. A. & SHUTKO, A. M. 1979. Microwave radiation of the earth's surface in the presence of vegetation cover. *Radiotekhnika i Elektronika,* 24**,** 256-264.

KONINGS, A. G., MCCOLL, K. A., PILES, M. & ENTEKHABI, D. 2015. How many parameters can be maximally estimated from a set of measurements? *IEEE Geoscience and Remote Sensing Letters,* 12**,** 1081-1085.

KONINGS, A. G., PILES, M., DAS, N. & ENTEKHABI, D. 2017. L-band vegetation optical depth and effective scattering albedo estimation from SMAP. *Remote Sensing of Environment,* 198**,** 460-470.

KONINGS, A. G., PILES, M., RÖTZER, K., MCCOLL, K. A., CHAN, S. K. & ENTEKHABI, D. 2016. Vegetation optical depth and scattering albedo retrieval using time series of dual-polarized L-band radiometer observations. *Remote Sensing of Environment,* 172**,** 178-189.

KOSTER, R. D., DIRMEYER, P. A., GUO, Z., BONAN, G., CHAN, E., COX, P., GORDON, C., KANAE, S., KOWALCZYK, E. & LAWRENCE, D. 2004. Regions of strong coupling between soil moisture and precipitation. *Science,* 305**,** 1138-1140.

KOYAMA, C. N., LIU, H., TAKAHASHI, K., SHIMADA, M., WATANABE, M., KHUUT, T. & SATO, M. 2017. In-situ measurement of soil permittivity at various depths for the calibration and validation of low-frequency SAR soil moisture models by using GPR. *Remote Sensing,* 9**,** 580.

KRAFT, D. 1988. A software package for sequential quadratic programming.

KURUM, M. 2013. Quantifying scattering albedo in microwave emission of vegetated terrain. *Remote Sensing of Environment,* 129**,** 66-74.

KURUM, M., O'NEILL, P. E., LANG, R. H., JOSEPH, A. T., COSH, M. H. & JACKSON, T. J. 2012. Effective tree scattering and opacity at L-band. *Remote Sensing of Environment,* 118**,** 1-9.

KUSTAS, W. P. & GOODRICH, D. C. 1994. Preface [to special section on Monsoon'90 Multidisciplinary Experiment]. *Water Resources Research,* 30**,** 1211-1225.

LANG, R. H. & SIGHU, J. S. 1983. Electromagnetic backscattering from a layer of vegetation: A discrete approach. *IEEE Transactions on Geoscience and Remote Sensing***,** 62-71.

LARSON, K. M., SMALL, E. E., GUTMANN, E., BILICH, A., AXELRAD, P. & BRAUN, J. 2008a. Using GPS multipath to measure soil moisture fluctuations: initial results. *GPS solutions,* 12**,** 173-177.

LARSON, K. M., SMALL, E. E., GUTMANN, E. D., BILICH, A. L., BRAUN, J. J. & ZAVOROTNY, V. U. 2008b. Use of GPS receivers as a soil moisture network for water cycle studies. *Geophysical Research Letters,* 35.

LAWRENCE, H., WIGNERON, J. P., DEMONTOUX, F., MIALON, A. & KERR, Y. H. 2013. Evaluating the semiempirical H–Q model used to calculate the L-band emissivity of a rough bare soil. *IEEE Transactions on Geoscience and Remote Sensing,* 51**,** 4075-4084.

LAWRENCE, H., WIGNERON, J. P., RICHAUME, P., NOVELLO, N., GRANT, J., MIALON, A., BITAR, A. A., MERLIN, O., GUYON, D. & LEROUX, D. 2014. Comparison between SMOS Vegetation Optical Depth products and MODIS vegetation indices over crop zones of the USA. *Remote Sensing of Environment,* 140**,** 396-406.

LE TOAN, T., QUEGAN, S., DAVIDSON, M., BALZTER, H., PAILLOU, P., PAPATHANASSIOU, K., PLUMMER, S., ROCCA, F., SAATCHI, S. & SHUGART, H. 2011. The BIOMASS mission: Mapping global forest biomass to better understand the terrestrial carbon cycle. *Remote sensing of environment,* 115**,** 2850-2860.

LEE, K.-H. & ANAGNOSTOU, E. N. 2004. A combined passive/active microwave remote sensing approach for surface variable retrieval using Tropical Rainfall Measuring Mission observations. *Remote Sensing of Environment,* 92**,** 112-125.

LEMMETYINEN, J., SCHWANK, M., RAUTIAINEN, K., KONTU, A., PARKKINEN, T., MäTZLER, C., WIESMANN, A., WEGMÜLLER, U., DERKSEN, C. & TOOSE, P. 2016. Snow density and ground permittivity retrieved from L-band radiometry: Application to experimental data. *Remote Sensing of Environment,* 180**,** 377-391.

LENG, P., SONG, X., DUAN, S.-B. & LI, Z.-L. 2016. A practical algorithm for estimating surface soil moisture using combined optical and thermal infrared data. *International Journal of Applied Earth Observation and Geoinformation,* 52**,** 338-348.

LI, X., AL-YAARI, A., SCHWANK, M., FAN, L., FRAPPART, F., SWENSON, J. & WIGNERON, J.-P. 2020. Compared performances of SMOS-IC soil moisture and vegetation optical depth retrievals based on Tau-Omega and Two-Stream microwave emission models. *Remote Sensing of Environment,* 236**,** 111502.

LI, X., CHENG, G., LIU, S., XIAO, Q., MA, M., JIN, R., CHE, T., LIU, Q., WANG, W. & QI, Y. 2013. Heihe watershed allied telemetry experimental research (HiWATER): Scientific objectives and experimental design. *Bulletin of the American Meteorological Society,* 94**,** 1145-1160.

LI, X., LI, X., LI, Z., MA, M., WANG, J., XIAO, Q., LIU, Q., CHE, T., CHEN, E. & YAN, G. 2009. Watershed allied telemetry experimental research. *Journal of Geophysical Research: Atmospheres,* 114.

LIU, C., CHEN, Z.-X., YUN, S., CHEN, J.-S., HASI, T. & PAN, H.-Z. 2019. Research advances of SAR remote sensing for agriculture applications: A review. *Journal of Integrative Agriculture,* 18**,** 506-525.

LIU, P.-W., DE ROO, R. D., ENGLAND, A. W. & JUDGE, J. 2012a. Impact of moisture distribution within the sensing depth on L-and C-band emission in sandy soils. *IEEE Journal of Selected Topics in Applied Earth Observations and Remote Sensing,* 6**,** 887-899.

LIU, W., BARET, F., GU, X., TONG, Q., ZHENG, L. & ZHANG, B. 2002. Relating soil surface moisture to reflectance. *Remote Sensing of Environment,* 81**,** 238-246.

LIU, Y., QIAN, J. & YUE, H. 2020. Combined Sentinel-1A with Sentinel-2A to estimate soil moisture in farmland. *IEEE Journal of Selected Topics in Applied Earth Observations and Remote Sensing,* 14**,** 1292-1310.

LIU, Y. Y., DORIGO, W. A., PARINUSSA, R. M., DE JEU, R. A. M., WAGNER, W., MCCABE, M. F., EVANS, J. P. & VAN DIJK, A. I. J. M. 2012b. Trend-preserving blending of passive and active microwave soil moisture retrievals. *Remote Sensing of Environment,* 123**,** 280-297.

LIU, Y. Y., PARINUSSA, R. M., DORIGO, W. A., DE JEU, R. A. M., WAGNER, W., VAN DIJK, A. I. J. M., MCCABE, M. F. & EVANS, J. P. 2011. Developing an improved soil moisture dataset by blending passive and active microwave satellite-based retrievals. *Hydrology and Earth System Sciences,* 15**,** 425-436.

LOBELL, D. B. & ASNER, G. P. 2002. Moisture effects on soil reflectance. *Soil Science Society of America Journal,* 66**,** 722-727.

LV, S., WEN, J., ZENG, Y., TIAN, H. & SU, Z. 2014. An improved two-layer algorithm for estimating effective soil temperature in microwave radiometry using in situ temperature and soil moisture measurements. *Remote Sensing of Environment,* 152**,** 356-363.

LV, S., ZENG, Y., SU, Z. & WEN, J. 2019. A closed-form expression of soil temperature sensing depth at L-band. *IEEE Transactions on Geoscience and Remote Sensing*.

MALTESE, A., BATES, P. D., CAPODICI, F., CANNAROZZO, M., CIRAOLO, G. & LOGGIA, G. L. 2013a. Critical analysis of thermal inertia approaches for surface soil water content retrieval. *International Association of Scientific Hydrology Bulletin,* 58**,** 1144-1161.

MALTESE, A., CAPODICI, F. & CIRAOLO, G. 2013b. Errata: Mapping soil water content under sparse vegetation and changeable sky conditions: comparison of two thermal inertia approaches. *Journal of Applied Remote Sensing,* 7**,** 073548.

MANNINEN, T., JääSKELäINEN, E., LOHILA, A., KORKIAKOSKI, M., RäSäNEN, A., VIRTANEN, T., MUHIĆ, F., MARTTILA, H., ALA-AHO, P. & MARKOVAARA-KOIVISTO, M. 2021. Very high spatial resolution soil moisture observation of heterogeneous subarctic catchment using nonlocal averaging and multitemporal SAR data. *IEEE Transactions on Geoscience and Remote Sensing*.

MARTENS, B., LIEVENS, H., COLLIANDER, A., JACKSON, T. J. & VERHOEST, N. E. C. 2015. Estimating effective roughness parameters of the L-MEB model for soil moisture retrieval using passive microwave observations from SMAPVEX12. *IEEE Transactions on Geoscience and Remote Sensing,* 53**,** 4091-4103.

MASON, P. J., ZILLMAN, J. W., SIMMONS, A., LINDSTROM, E. J., HARRISON, D. E., DOLMAN, H., BOJINSKI, S., FISCHER, A., LATHAM, J. & RASMUSSEN, J. 2010. Implementation plan for the global observing system for climate in support of the UNFCCC (2010 Update). *Lecture Notes in Physics,* 275**,** 287-306.

MATSUSHIMA, D., ASANUMA, J. & KAIHOTSU, I. 2018. Thermal Inertia Approach Using a Heat Budget Model to Estimate the Spatial Distribution of Surface Soil Moisture over a Semiarid Grassland in Central Mongolia. *Journal of Hydrometeorology,* 19**,** 245-265.

MäTZLER, C. 1998. Improved Born approximation for scattering of radiation in a granular medium. *Journal of Applied Physics,* 83**,** 6111-6117.

MCNAIRN, H., JACKSON, T. J., WISEMAN, G., BéLAIR, S., BERG, A., BULLOCK, P., COLLIANDER, A., COSH, M. H., KIM, S.-B. & MAGAGI, R. 2014. The soil moisture active passive validation experiment 2012 (SMAPVEX12): prelaunch calibration and validation of the SMAP soil moisture algorithms. *IEEE Transactions on Geoscience and Remote Sensing,* 53**,** 2784-2801.

MEESTERS, A. G., DE JEU, R. A. & OWE, M. 2005. Analytical derivation of the vegetation optical depth from the microwave polarization difference index. *IEEE Geoscience and Remote Sensing Letters,* 2**,** 121-123.

MEGURO, A., SHINTATE, K., USUI, M. & TSUJIHATA, A. 2009. In-orbit deployment characteristics of large deployable antenna reflector onboard Engineering Test Satellite VIII. *Acta Astronautica,* 65**,** 1306-1316.

MERLIN, O., WALKER, J. P., KALMA, J. D., KIM, E. J., HACKER, J., PANCIERA, R., YOUNG, R., SUMMERELL, G., HORNBUCKLE, J. & HAFEEZ, M. 2008. The

NAFE'06 data set: Towards soil moisture retrieval at intermediate resolution. *Advances in Water Resources,* 31**,** 1444-1455.

MERLIN, O., WALKER, J. P., PANCIERA, R., YOUNG, R., KALMA, J. D. & KIM, E. J. 2007. Soil moisture measurement in heterogeneous terrain. *Modsim International Congress on Modelling & Simulation Land Water & Environmental Management Integrated Systems for Sustainability.*

MIALON, A., RICHAUME, P., LEROUX, D., BIRCHER, S., BITAR, A. A., PELLARIN, T., WIGNERON, J. P. & KERR, Y. H. 2015. Comparison of Dobson and Mironov dielectric models in the SMOS soil moisture retrieval algorithm. *IEEE Transactions on Geoscience and Remote Sensing,* 53**,** 3084-3094.

MIALON, A., WIGNERON, J. P., ROSNAY, P. D., ESCORIHUELA, M. J. & KERR, Y. H. 2012. Evaluating the L-MEB model from long-term microwave measurements over a rough field, SMOSREX 2006. *IEEE Transactions on Geoscience and Remote Sensing,* 50**,** 1458-1467.

MIRONOV, V., KERR, Y., WIGNERON, J. P., KOSOLAPOVA, L. & DEMONTOUX, F. 2013a. Temperature- and texture-dependent dielectric model for moist soils at 1.4 GHz. *IEEE Geoscience and Remote Sensing Letters,* 10**,** 419-423.

MIRONOV, V. & SAVIN, I. 2015. A temperature-dependent multi-relaxation spectroscopic dielectric model for thawed and frozen organic soil at 0.05-15 GHz. *Physics and Chemistry of the Earth,* 83-84**,** 57-64.

MIRONOV, V. L., BOBROV, P. P. & FOMIN, S. V. 2013b. Multirelaxation generalized refractive mixing dielectric model of moist soils. *IEEE Geoscience and Remote Sensing Letters,* 10**,** 603-606.

MIRONOV, V. L., BOBROV, P. P. & FOMIN, S. V. Dielectric model of moist soils with varying clay content in the 0.04 to 26.5 GHz frequency range. International Siberian Conference on Control and Communications, 2014. 1-4.

MIRONOV, V. L., DOBSON, M. C., KAUPP, V. H., KOMAROV, S. A. & KLESHCHENKO, V. N. 2004. Generalized refractive mixing dielectric model for moist soils. *IEEE Transactions on Geoscience and Remote Sensing,* 42**,** 773-785.

MIRONOV, V. L., KOSOLAPOVA, L. G. & FOMIN, S. 2009. Physically and mineralogically based spectroscopic dielectric model for moist soils. *IEEE Transactions on Geoscience and Remote Sensing,* 47**,** 2059-2070.

MIRONOV, V. L., KOSOLAPOVA, L. G., LUKIN, Y. I., KARAVAYSKY, A. Y. & MOLOSTOV, I. P. 2017a. Temperature-and texture-dependent dielectric model for frozen and thawed mineral soils at a frequency of 1.4 GHz. *Remote Sensing of Environment,* 200**,** 240-249.

MIRONOV, V. L., MOLOSTOV, I. P., LUKI, Y. I., KARAVAYSKY, A. Y. & FOMIN, S. V. 2017b. Frequency-, temperature-, and texture-dependent dielectric model for

frozen and thawed arctic mineral soils. *2017 Progress in Electromagnetics Research Symposium - Spring (Piers)*, 2546-2553.

MITTELBACH, H., HIRSCHI, M., PRATOLA, C., SMOLANDER, T., LAHOZ, W. A., DWYER, N., RAUTIAINEN, K. & SENEVIRATNE, S. I. 2014. Product validation and intercomparison report (PVIR) version 1.0. Available online: http://www.esa-soilmoisture-cci.org/node/119: European Space Agency.

MO, T., CHOUDHURY, B. J., SCHMUGGE, T. J., WANG, J. R. & JACKSON, T. J. 1982. A model for microwave emission from vegetation - covered fields. *Journal of Geophysical Research: Oceans,* 87**,** 11229-11237.

MO, T. & SCHMUGGE, T. J. 1987. A parameterization of the effect of surface roughness on microwave emission. *IEEE Transactions on Geoscience and Remote Sensing,* GE-25**,** 481-486.

MONTPETIT, B., ROYER, A., WIGNERON, J. P., CHANZY, A. & MIALON, A. 2015. Evaluation of multi-frequency bare soil microwave reflectivity models. *Remote Sensing of Environment,* 162**,** 186-195.

MONTZKA, C., COSH, M., BAYAT, B., AL BITAR, A., BERG, A., BINDLISH, R., BOGENA, H., BOLTEN, J., CABOT, F. & CALDWELL, T. 2020. Soil moisture product validation good practices protocol version 1.0. *Good Practices for Satellite Derived Land Product Validation*, 123.

MORAN, M. S., PETERS-LIDARD, C. D., WATTS, J. M. & MCELROY, S. 2004. Estimating soil moisture at the watershed scale with satellite-based radar and land surface models. *Canadian journal of remote sensing,* 30**,** 805-826.

NADLER, A. & LAPID, Y. 1996. An improved capacitance sensor for in situ monitoring of soil moisture. *Soil Research,* 34**,** 361-368.

NARAYAN, U., LAKSHMI, V. & NJOKU, E. G. 2004. Retrieval of soil moisture from passive and active L/S band sensor (PALS) observations during the Soil Moisture Experiment in 2002 (SMEX02). *Remote Sensing of Environment,* 92**,** 483-496.

NEELAM, M., COLLIANDER, A., MOHANTY, B. P., COSH, M. H., MISRA, S. & JACKSON, T. J. 2020. Multiscale surface roughness for improved soil moisture estimation. *IEEE Transactions on Geoscience and Remote Sensing,* 58**,** 5264-5276.

NEWTON, R., HEILMAN, J. & VAN BAVEL, C. 1983. Integrating passive microwave measurements with a soil moisture/heat flow model. *Agricultural Water Management,* 7**,** 379-389.

NEWTON, R. W., BLACK, Q. R., MAKANVAND, S., BLANCHARD, A. J. & JEAN, B. R. 1982. Soil moisture information and thermal microwave emission. *IEEE Transactions on Geoscience and Remote Sensing*, 275-281.

NEWTON, R. W. & ROUSE, J. W. 1980. Microwave radiometer measurements of soil moisture content. *IEEE Transactions on Antennas and Propagation,* 28**,** 680 - 686.

NICHOLS, W. E., CUENCA, R. H., SCHMUGGE, T. J. & WANG, J. R. 1993. Pushbroom microwave radiometer results from HAPEX-MOBILHY. *Remote Sensing of Environment,* 46**,** 119-128.

NJOKU, E. & O'NEILL, P. 1982. Multifrequency microwave radiometer measurements of soil moisture. *IEEE Transactions on Geoscience and Remote Sensing,* 20**,** 468-475.

NJOKU, E. G. 1976. *Microwave remote sensing of near-surface moisture and temperature profiles.* Massachusetts Institute of Technology.

NJOKU, E. G. & CHAN, S. K. 2006. Vegetation and surface roughness effects on AMSR-E land observations. *Remote Sensing of Environment,* 100**,** 190-199.

NJOKU, E. G. & ENTEKHABI, D. 1996. Passive microwave remote sensing of soil moisture. *Journal of Hydrology,* 184**,** 101-129.

NJOKU, E. G., JACKSON, T. J., LAKSHMI, V., CHAN, T. K. & NGHIEM, S. V. 2003. Soil moisture retrieval from AMSR-E. *IEEE Transactions on Geoscience and Remote Sensing,* 41**,** 215-229.

NJOKU, E. G. & KONG, J. A. 1977. Theory for passive microwave remote sensing of near - surface soil moisture. *Journal of Geophysical Research,* 82**,** 3108-3118.

NJOKU, E. G. & LI, L. 1999. Retrieval of land surface parameters using passive microwave measurements at 6-18 GHz. *IEEE Transactions on Geoscience and Remote Sensing,* 37**,** 79-93.

NJOKU, E. G., SCHIEDGE, J. & KAHLE, A. B. 1980. Joint microwave and infrared studies for soil moisture determination. Jet Propulsion Laboratory.

NJOKU, E. G., WILSON, W. J., YUEH, S. H. & RAHMAT-SAMII, Y. 2000. A large-antenna microwave radiometer-scatterometer concept for ocean salinity and soil moisture sensing. *IEEE Transactions on Geoscience and Remote Sensing,* 38**,** 2645-2655.

O'NEILL, P., BINDLISH, R., CHAN, S., CHAUBELL, J., COLLIANDER, A., NJOKU, E. & JACKSON, T. 2021a. SMAP algorithm theoretical basis document (ATBD) level 2 & 3 soil moisture (passive) data products revision G. https://nsidc.org/data/smap/technical-references: Jet Propulsion Laboratory.

O'NEILL, P., CHAN, S., BINDLISH, R., CHAUBELL, M., COLLIANDER, A., CHEN, F., DUNBAR, S., JACKSON, T., PENG, J., MOUSAVI, M., COSH, M., BONGIOVANNI, T., WALKER, J., WU, X., BERG, A., MCNAIRN, H., THIBEAULT, M., MARTÍNEZ-FERNÁNDEZ, J., GONZÁLEZ-ZAMORA, Á., LOPEZ-BAEZA, E., JENSEN, K., SEYFRIED, M., BOSCH, D., STARKS, P., COLLINS, C. H., PRUEGER, J., SU, Z., VELDE, R. V. D., ASANUMA, J., PALECKI, M., SMALL, E., ZREDA, M., CALVET, J., CROW, W., KERR, Y., YUEH, S. & ENTEKHABI, D. 2021b. Calibration and validation for the L2/3_SM_P version 8 and L2/3_SM_P_E version 5 data products. https://nsidc.org/data/smap/technical-references: Jet Propulsion Laboratory.

OH, Y. & KAY, Y. C. 1998. Condition for precise measurement of soil surface roughness. *IEEE Transactions on Geoscience and Remote Sensing,* 36**,** 691-695.

OH, Y., SARABANDI, K. & ULABY, F. T. 1992. An empirical model and an inversion technique for radar scattering from bare soil surfaces. *IEEE Transactions on Geoscience and Remote Sensing,* 30**,** 370 - 381.

OKI, T. & KANAE, S. 2006. Global hydrological cycles and world water resources. *Science,* 313**,** 1068.

OWE, M., DE JEU, R. A. M. & HOLMES, T. 2008. Multisensor historical climatology of satellite-derived global land surface moisture. *Journal of Geophysical Research: Earth Surface (2003–2012),* 113**,** F01002.

OWE, M., DE JEU, R. A. M. & WALKER, J. 2001. A methodology for surface soil moisture and vegetation optical depth retrieval using the microwave polarization difference index. *IEEE Transactions on Geoscience and Remote Sensing,* 39**,** 1643-1654.

PALOSCIA, S., PAMPALONI, P., CHIARANTINI, L., COPPO, P., GAGLIANI, S. & LUZI, G. 1993. Multifrequency passive microwave remote sensing of soil moisture and roughness. *International Journal of Remote Sensing,* 14**,** 467-483.

PANCIERA, R., TANASE, M. A., LOWELL, K. & WALKER, J. P. 2014. Evaluation of IEM, Dubois, and Oh radar backscatter models using airborne L-band SAR. *IEEE Transactions on Geoscience and Remote Sensing,* 52**,** 4966-4979.

PANCIERA, R., WALKER, J. P., JACKSON, T. J., GRAY, D. A., TANASE, M. A., RYU, D., MONERRIS, A., YARDLEY, H., RÜDIGER, C. & WU, X. 2013. The soil moisture active passive experiments (SMAPEx): Toward soil moisture retrieval from the SMAP mission. *IEEE Transactions on Geoscience and Remote Sensing,* 52**,** 490-507.

PANCIERA, R., WALKER, J. P., KALMA, J. D., KIM, E. J., HACKER, J. M., MERLIN, O., BERGER, M. & SKOU, N. 2008. The NAFE'05/CoSMOS data set: Toward SMOS soil moisture retrieval, downscaling, and assimilation. *IEEE Transactions on Geoscience and Remote Sensing,* 46**,** 736-745.

PANCIERA, R., WALKER, J. P., KALMA, J. D., KIM, E. J., SALEH, K. & WIGNERON, J. P. 2009a. Evaluation of the SMOS L-MEB passive microwave soil moisture retrieval algorithm. *Remote Sensing of Environment,* 113**,** 435-444.

PANCIERA, R., WALKER, J. P. & MERLIN, O. 2009b. Improved understanding of soil surface roughness parameterization for L-band passive microwave soil moisture retrieval. *IEEE Geoscience and Remote Sensing Letters,* 6**,** 625-629.

PARDé, M., ZRIBI, M., WIGNERON, J., DECHAMBRE, M., FANISE, P., KERR, Y., CRAPEAU, M., SALEH, K., CALVET, J. & ALBERGEL, C. 2011. Soil moisture estimations based on airborne CAROLS L-band microwave data. *Remote Sensing,* 3**,** 2591-2604.

PARINUSSA, R. M., LAKSHMI, V., JOHNSON, F. M. & SHARMA, A. 2016. A new framework for monitoring flood inundation using readily available satellite data. *Geophysical Research Letters*.

PARK, C.-H., MONTZKA, C., JAGDHUBER, T., JONARD, F., DE LANNOY, G., HONG, J., JACKSON, T. & WULFMEYER, V. 2019. A dielectric mixing model accounting for soil organic matter. *Vadose Zone Journal,* 18.

PARRENS, M., WIGNERON, J. P., RICHAUME, P., BITAR, A. A., MIALON, A., FERNANDEZ-MORAN, R., AL-YAARI, A., O'NEILL, P. & KERR, Y. 2017. Considering combined or separated roughness and vegetation effects in soil moisture retrievals. *International Journal of Applied Earth Observation & Geoinformation,* 55**,** 73-86.

PATTON, J. & HORNBUCKLE, B. 2012. Initial validation of SMOS vegetation optical thickness in Iowa. *IEEE Geoscience and Remote Sensing Letters,* 10**,** 647-651.

PEISCHL, S., WALKER, J. P., RÜDIGER, C., YE, N., KERR, Y. H., KIM, E., BANDARA, R. & ALLAHMORADI, M. 2012a. The AACES field experiments: SMOS calibration and validation across the Murrumbidgee River catchment. *Hydrology and Earth System Sciences,* 16**,** 1697-1708.

PEISCHL, S., WALKER, J. P., RYU, D., KERR, Y. H., PANCIERA, R. & RUDIGER, C. 2012b. Wheat canopy structure and surface roughness effects on multiangle observations at L-band. *IEEE Transactions on Geoscience and Remote Sensing,* 50**,** 1498-1506.

PELLARIN, T., KERR, Y. H. & WIGNERON, J. P. 2006. Global simulation of brightness temperatures at 6.6 and 10.7 GHz over land based on SMMR data set analysis. *IEEE Transactions on Geoscience and Remote Sensing,* 44**,** 2492-2505.

PENG, B., ZHAO, T., SHI, J., LU, H., MIALON, A., KERR, Y. H., LIANG, X. & GUAN, K. 2017a. Reappraisal of the roughness effect parameterization schemes for L-band radiometry over bare soil. *Remote Sensing of Environment,* 199**,** 63-77.

PENG, J., LOEW, A., MERLIN, O. & VERHOEST, N. E. 2017b. A review of spatial downscaling of satellite remotely sensed soil moisture. *Reviews of Geophysics,* 55**,** 341-366.

PEPLINSKI, N. R., ULABY, F. T. & DOBSON, M. C. 1995a. Correction to 'Dielectric properties of soils in the 0.3-1.3-GHz range'. *IEEE Transactions on Geoscience and Remote Sensing,* 33**,** 1340.

PEPLINSKI, N. R., ULABY, F. T. & DOBSON, M. C. 1995b. Dielectric properties of soils in the 0.3-1.3-GHz range. *IEEE Transactions on Geoscience and Remote Sensing,* 33**,** 803-807.

PETROPOULOS, G. P., IRELAND, G. & BARRETT, B. 2015. Surface soil moisture retrievals from remote sensing: Current status, products & future trends. *Physics and Chemistry of the Earth,* 83–84**,** 36-56.

PHAM, H., KIM, E. J. & ENGLAND, A. W. 2005. An analytical calibration approach for microwave polarimetric radiometers. *IEEE Transactions on Geoscience and Remote Sensing,* 43**,** 2443-2451.

POHN, H., OFFIELD, T. & WATSON, K. 1974. Thermal inertia mapping from satellite-discrimination of geologic units in Oman. *Journal of Research of the US Geological Survey,* 2**,** 147-158.

PRIGENT, C., WIGNERON, J.-P., ROSSOW, W. B. & PARDO-CARRION, J. R. 2000. Frequency and angular variations of land surface microwave emissivities: Can we estimate SSM/T and AMSU emissivities from SSM/I emissivities? *IEEE Transactions on Geoscience and Remote Sensing,* 38**,** 2373-2386.

PROMES, P. M., JACKSON, T. J. & NEILL, P. E. O. 1988. Significance of agricultural row structure on the microwave emissivity of soils. *IEEE Transactions on Geoscience and Remote Sensing,* 26**,** 580-589.

PULLIAINEN, J., KARNA, J.-P. & HALLIKAINEN, M. 1993. Development of geophysical retrieval algorithms for the MIMR. *IEEE Transactions on Geoscience and Remote Sensing,* 31**,** 268-277.

RAJU, S., CHANZY, A., WIGNERON, J.-P., CALVET, J.-C., KERR, Y. & LAGUERRE, L. 1995. Soil moisture and temperature profile effects on microwave emission at low frequencies. *Remote Sensing of Environment,* 54**,** 85-97.

REECE, C. F. 1996. Evaluation of a line heat dissipation sensor for measuring soil matric potential. *Soil Science Society of America Journal,* 60**,** 1022-1028.

ROBOCK, A., VINNIKOV, K. Y., SRINIVASAN, G., ENTIN, J. K., HOLLINGER, S. E., SPERANSKAYA, N. A., LIU, S. X. & NAMKHAI, A. 2000. The global soil moisture data bank. *Bulletin of the American Meteorological Society,* 81**,** 1281-1299.

RODELL, M., VELICOGNA, I. & FAMIGLIETTI, J. S. 2009. Satellite-based estimates of groundwater depletion in India. *Nature,* 460**,** 999-1002.

RODRÍGUEZ-FERNÁNDEZ, N. J., ANTERRIEU, E., ROUGé, B., BOUTIN, J., PICARD, G., PELLARIN, T., ESCORIHUELA, M. J., AL BITAR, A., RICHAUME, P. & MIALON, A. SMOS-HR: A high resolution L-band passive radiometer for Earth science and applications. 2019 IEEE International Geoscience and Remote Sensing Symposium (IGARSS), 2019. IEEE, 8392-8395.

ROSNAY, P. D., CALVET, J. C., KERR, Y., WIGNERON, J. P., LEMAîTRE, F., ESCORIHUELA, M. J., SABATER, J. M., SALEH, K., BARRIé, J. & BOUHOURS, G. 2006. SMOSREX: A long term field campaign experiment for soil moisture and land surface processes remote sensing. *Remote Sensing of Environment,* 102**,** 377-389.

SABAGHY, S., WALKER, J. P., RENZULLO, L. J. & JACKSON, T. J. 2018. Spatially enhanced passive microwave derived soil moisture: Capabilities and opportunities. *Remote Sensing of Environment,* 209**,** 551-580.

SCHMUGGE, T., JACKSON, T. & MCKIM, H. 1980. Survey of methods for soil moisture determination. *Water Resources Research,* 16**,** 961-979.

SCHMUGGE, T. J. & CHOUDHURY, B. J. 1981. A comparison of radiative transfer models for predicting the microwave emission from soils. *Radio Science,* 16**,** 927-938.

SCHOLZE, M., KAMINSKI, T., KNORR, W., BLESSING, S., VOSSBECK, M., GRANT, J. P. & SCIPAL, K. 2016. Simultaneous assimilation of SMOS soil moisture and atmospheric CO2 in-situ observations to constrain the global terrestrial carbon cycle. *Remote Sensing of Environment,* 180**,** 334-345.

SCHULTE, R., FEALY, R., CREAMER, R., TOWERS, W., HARTY, T. & JONES, R. 2012. A review of the role of excess soil moisture conditions in constraining farm practices under Atlantic conditions. *Soil Use and Management,* 28**,** 580-589.

SCHWANK, M., VOLKSCH, I., WIGNERON, J.-P., KERR, Y. H., MIALON, A., DE ROSNAY, P. & MATZLER, C. 2009. Comparison of two bare-soil reflectivity models and validation with L-band radiometer measurements. *IEEE Transactions on Geoscience and Remote Sensing,* 48**,** 325-337.

SCHWANK, M., WIGNERON, J. P., LOPEZ-BAEZA, E., VOLKSCH, I., MATZLER, C. & KERR, Y. H. 2012. L-Band Radiative Properties of Vine Vegetation at the MELBEX III SMOS Cal/Val Site. *IEEE Transactions on Geoscience & Remote Sensing,* 50**,** 1587-1601.

SCIPAL, K., DRUSCH, M. & WAGNER, W. 2008. Assimilation of a ERS scatterometer derived soil moisture index in the ECMWF numerical weather prediction system. *Advances in water resources,* 31**,** 1101-1112.

SENEVIRATNE, S. I., CORTI, T., DAVIN, E. L., HIRSCHI, M., JAEGER, E. B., LEHNER, I., ORLOWSKY, B. & TEULING, A. J. 2010. Investigating soil moisture–climate interactions in a changing climate: A review. *Earth-Science Reviews,* 99**,** 125-161.

SHAMAN, J. & DAY, J. F. 2005. Achieving operational hydrologic monitoring of mosquitoborne disease. *Emerging Infectious Diseases,* 11**,** 1343-1350.

SHEN, X., AN, R., QUAYE - BALLARD, J. A., ZHANG, L. & WANG, Z. 2016. Evaluation of the European Space Agency Climate Change Initiative Soil Moisture Product over China using variance reduction factor. *Journal of the American Water Resources Association,* 52**,** 1524-1535.

SHEN, X., WALKER, J. P., YE, N., WU, X., BOOPATHI, N., YEO, I.-Y., ZHANG, L. & ZHU, L. 2021. Soil moisture retrieval depth of P- and L-band radiometry: predictions and observations. *IEEE Transactions on Geoscience and Remote Sensing,* 59**,** 6814-6822.

SHEN, X., WALKER, J. P., YE, N., WU, X., BRAKHASI, F., BOOPATHI, N., ZHU, L., YEO, I.-Y., KIM, E., KERR, Y. & JACKSON, T. 2022a. Impact of random and

periodic surface roughness on P- and L-band radiometry. *Remote Sensing of Environment,* 269**,** 112825.

SHEN, X., WALKER, J. P., YE, N., WU, X., BRAKHASI, F., BOOPATHI, N., ZHU, L., YEO, I.-Y., KIM, E., KERR, Y. & JACKSON, T. 2022b. Evaluation of the tau-omega model over bare and wheat-covered flat and periodic soil surfaces at P- and L-band. *Remote Sensing of Environment,* 273**,** 112960.

SHI, J., CHEN, K. S., LI, Q. & JACKSON, T. J. 2002. A parameterized surface reflectivity model and estimation of bare-surface soil moisture with L-band radiometer. *IEEE Transactions on Geoscience and Remote Sensing,* 40**,** 2674-2686.

SHI, J., DONG, X., ZHAO, T., DU, J., JIANG, L., DU, Y., LIU, H., WANG, Z., JI, D. & XIONG, C. WCOM: The science scenario and objectives of a global water cycle observation mission. 2014 IEEE International Geoscience and Remote Sensing Symposium (IGARSS), 2014. IEEE, 3646-3649.

SHI, J., WANG, J., HSU, A. Y., O'NEILL, P. E. & ENGMAN, E. T. 1997. Estimation of bare surface soil moisture and surface roughness parameter using L-band SAR image data. *IEEE Transactions on Geoscience and Remote Sensing,* 35**,** 1254-1266.

SHIKLOMANOV, I. A. 1993. World fresh water resources. *In:* GLEICK, P. H. (ed.) *Water in Crisis: A Guide to the World's Fresh Water Resources.* New York: Oxford University Press.

SKOU, N., MISRA, S., BALLING, J. E., KRISTENSEN, S. S. & SOBJAERG, S. S. 2009. L-band RFI as experienced during airborne campaigns in preparation for SMOS. *IEEE Transactions on Geoscience and Remote Sensing,* 48**,** 1398-1407.

SORIANO-DISLA, J. M., JANIK, L. J., VISCARRA ROSSEL, R. A., MACDONALD, L. M. & MCLAUGHLIN, M. J. 2014. The performance of visible, near-, and mid-infrared reflectance spectroscopy for prediction of soil physical, chemical, and biological properties. *Applied Spectroscopy Reviews,* 49**,** 139-186.

SRIVASTAVA, H. S., PATEL, P. & NAVALGUND, R. R. How far SAR has fulfilled its expectation for soil moisture retrieval. Microwave Remote Sensing of the Atmosphere and Environment V, 2006. International Society for Optics and Photonics, 641001.

SRIVASTAVA, P. K., O'NEILL, P., COSH, M., KURUM, M., LANG, R. & JOSEPH, A. 2015. Evaluation of dielectric mixing models for passive microwave soil moisture retrieval using data from ComRAD ground-based SMAP simulator. *IEEE Journal of Selected Topics in Applied Earth Observations and Remote Sensing,* 8**,** 4345-4354.

STEVENS, M. T., MCKINLEY, G. B. & VAHEDIFARD, F. 2016. A comparison of ground vehicle mobility analysis based on soil moisture time series datasets from WindSat, LIS, and in situ sensors. *Journal of Terramechanics,* 65**,** 49-59.

STILES, J. M. & SARABANDI, K. 2000. Electromagnetic scattering from grassland. I. A fully phase-coherent scattering model. *Geoscience and Remote Sensing, IEEE Transactions on,* 38**,** 339-348.

STOCKER, B. D., ZSCHEISCHLER, J., KEENAN, T. F., PRENTICE, I. C., SENEVIRATNE, S. I. & PEñUELAS, J. 2019. Drought impacts on terrestrial primary production underestimated by satellite monitoring. *Nature Geoscience*.

STOGRYN, A. 1970. The brightness temperature of a vertically structured medium. *Radio Science,* 5**,** 1397-1406.

TABATABAEENEJAD, A., BURGIN, M., DUAN, X. & MOGHADDAM, M. 2014. P-band radar retrieval of subsurface soil moisture profile as a second-order polynomial: First AirMOSS results. *IEEE Transactions on Geoscience and Remote Sensing,* 53**,** 645-658.

TABATABAEENEJAD, A., CHEN, R. H., BURGIN, M. S., DUAN, X., CUENCA, R. H., COSH, M. H., SCOTT, R. L. & MOGHADDAM, M. 2020. Assessment and validation of AirMOSS P-band root-zone soil moisture products. *IEEE Transactions on Geoscience and Remote Sensing,* 58**,** 6181-6196.

TAL, E. 2016. The water cycle. https://energyeducation.ca/wiki/images/thumb/b/b1/Diagram_of_the_Water_Cycle.jpg/750px-Diagram_of_the_Water_Cycle.jpg.

TELENORGROUP The electromagnetic spectrum. https://www.telenor.com/sustainability/responsible-business/safe-services/mobile-phones-and-health/.

TOBIN, K. J., CROW, W. T. & BENNETT, M. E. 2021. Root Zone Soil Moisture Comparisons: AirMOSS, SMERGE, and SMAP. *IEEE Geoscience and Remote Sensing Letters*.

TORRES, R., SNOEIJ, P., GEUDTNER, D., BIBBY, D., DAVIDSON, M., ATTEMA, E., POTIN, P., ROMMEN, B., FLOURY, N. & BROWN, M. 2012. GMES Sentinel-1 mission. *Remote Sensing of Environment,* 120**,** 9-24.

TRENBERTH, K. E., FASULLO, J. T. & KIEHL, J. 2009. Earth's global energy budget. *Bulletin of the American Meteorological Society,* 90.

TSANG, L. & KONG, J. 1975. The brightness temperature of a half‐space random medium with nonuniform temperature profile. *Radio Science,* 10**,** 1025-1033.

ULABY, F. T., LONG, D. G., BLACKWELL, W. J., ELACHI, C., FUNG, A. K., RUF, C., SARABANDI, K., ZEBKER, H. A. & VAN ZYL, J. 2014. *Microwave radar and radiometric remote sensing*, University of Michigan Press Ann Arbor.

ULABY, F. T., MOORE, R. K. & FUNG, A. K. 1982. *Microwave remote sensing active and passive-Volume II: Radar remote sensing and surface scattering and enission theory*, Artech House Inc.

ULABY, F. T., MOORE, R. K. & FUNG, A. K. 1986. *Microwave remote sensing active and passive-Volume III: From theory to applications*, Artech House Inc.

ULABY, F. T., RAZANI, M. & DOBSON, M. C. 1983. Effects of vegetation cover on the microwave radiometric sensitivity to soil moisture. *IEEE Transactions on Geoscience and Remote Sensing*, 51-61.

ULABY, F. T., SARABANDI, K., MCDONALD, K., WHITT, M. & DOBSON, M. C. 1990. Michigan microwave canopy scattering model. *International Journal of Remote Sensing,* 11**,** 1223-1253.

VAN DER SCHALIE, R., KERR, Y. H., WIGNERON, J. P., RODRÍGUEZ-FERNÁNDEZ, N. J., AL-YAARI, A. & JEU, R. A. M. D. 2016. Global SMOS soil moisture retrievals from the Land Parameter Retrieval Model. *International Journal of Applied Earth Observation & Geoinformation,* 45**,** 125-134.

VAN DER SCHALIE, R., PARINUSSA, R. M., RENZULLO, L. J., VAN DIJK, A. I. J. M., SU, C. H. & DE JEU, R. A. M. 2015. SMOS soil moisture retrievals using the land parameter retrieval model: Evaluation over the Murrumbidgee Catchment, southeast Australia. *Remote Sensing of Environment*.

VOLO, T. J., VIVONI, E. R., MARTIN, C. A., EARL, S. & RUDDELL, B. L. 2014. Modelling soil moisture, water partitioning, and plant water stress under irrigated conditions in desert urban areas. *Ecohydrology,* 7**,** 1297-1313.

WAGNER, N., EMMERICH, K., BONITZ, F. & KUPFER, K. 2011. Experimental investigations on the frequency- and temperature-dependent dielectric material properties of soil. *IEEE Transactions on Geoscience and Remote Sensing,* 49**,** 2518-2530.

WAGNER, W., DORIGO, W. A., DE JEU, R. A. M., FERNANDEZ, D., BENVENISTE, J., HAAS, E. & ERTL, M. Fusion of active and passive microwave observations to create an essential climate variable data record on soil moisture. Proceedings of the XXII International Society for Photogrammetry and Remote Sensing (ISPRS) Congress, Melbourne, Australia, 2012.

WAITE, W. P., SADEGHI, A. M. & SCOTT, H. D. 1984. Microwave bistatic reflectivity dependence on the moisture content and matric potential of bare soil. *IEEE Transactions on Geoscience and Remote Sensing*, 394-405.

WALKER, J. P. & HOUSER, P. R. 2004. Requirements of a global near-surface soil moisture satellite mission: accuracy, repeat time, and spatial resolution. *Advances in water resources,* 27**,** 785-801.

WALKER, V. A., HORNBUCKLE, B. K., COSH, M. H. & PRUEGER, J. H. 2019. Seasonal evaluation of SMAP soil moisture in the US corn belt. *Remote Sensing,* 11**,** 2488.

WANG, J., HSU, A., SHI, J., O'NEILL, P. & ENGMAN, E. 1997. A comparison of soil moisture retrieval models using SIR-C measurements over the Little Washita River watershed. *Remote Sensing of Environment,* 59**,** 308-320.

WANG, J., SHIUE, J., SCHMUGGE, T. & ENGMAN, E. 1990. The L-band PBMR measurements of surface soil moisture in FIFE. *IEEE Transactions on Geoscience and Remote Sensing,* 28**,** 906-914.

WANG, J. R. & CHOUDHURY, B. J. 1981. Remote sensing of soil moisture content, over bare field at 1.4 GHz frequency. *Journal of Geophysical Research: Oceans,* 86**,** 5277-5282.

WANG, J. R., NEWTON, R. W. & ROUSE, J. W. 1980. Passive microwave remote sensing of soil moisture: The effect of tilled row structure. *IEEE Transactions on Geoscience and Remote Sensing***,** 296-302.

WANG, J. R., O'NEILL, P. E., JACKSON, T. J. & ENGMAN, E. T. 1983. Multifrequency measurements of the effects of soil moisture, soil texture, and surface roughness. *IEEE Transactions on Geoscience and Remote Sensing,* 21:1**,** 44-51.

WANG, J. R. & SCHMUGGE, T. J. 1980. An empirical model for the complex dielectric permittivity of soils as a function of water content. *IEEE Transactions on Geoscience and Remote Sensing,* GE-18**,** 288-295.

WANG, J. R., SHIUE, J. C., CHUANG, S. L., SHIN, R. T. & DOMBROWSKI, M. 1984. Thermal microwave emission from vegetated fields: A comparison between theory and experiment. *IEEE Transactions on Geoscience and Remote Sensing***,** 143-150.

WANG, L. & QU, J. J. 2009. Satellite remote sensing applications for surface soil moisture monitoring: A review. *Frontiers of Earth Science in China,* 3**,** 237-247.

WEI, M. Y. Soil moisture: report of a workshop held in Tiburon, California, 25-27 January 1994. NASA Conference Publication, 1995.

WIESMANN, A. & MäTZLER, C. 1999. Microwave emission model of layered snowpacks. *Remote Sensing of Environment,* 70**,** 307-316.

WIGNERON, J.-P., CHANZY, A., CALVET, J.-C. & BRUGUIER, N. 1995. A simple algorithm to retrieve soil moisture and vegetation biomass using passive microwave measurements over crop fields. *Remote Sensing of Environment,* 51.

WIGNERON, J.-P., KERR, Y., CHANZY, A. & JIN, Y.-Q. 1993a. Inversion of surface parameters from passive microwave measurements over a soybean field. *Remote Sensing of Environment,* 46**,** 61-72.

WIGNERON, J. P., CALVET, J. C., KERR, Y. & CHANZY, A. 1993b. Microwave emission of vegetation: sensitivity to leaf characteristics. *IEEE Transactions on Geoscience and Remote Sensing,* 31**,** 716-726.

WIGNERON, J. P., CHANZY, A., KERR, Y. H., LAWRENCE, H., SHI, J., ESCORIHUELA, M. J., MIRONOV, V., MIALON, A., DEMONTOUX, F. & ROSNAY, P. D. 2011. Evaluating an improved parameterization of the soil emission in L-MEB. *IEEE Transactions on Geoscience and Remote Sensing,* 49**,** 1177-1189.

WIGNERON, J. P., CHANZY, A., ROSNAY, P. D., RUDIGER, C. & CALVET, J. C. 2008. Estimating the effective soil temperature at L-band as a function of soil properties. *IEEE Transactions on Geoscience and Remote Sensing,* 46**,** 797-807.

WIGNERON, J. P., JACKSON, T. J., O'NEILL, P., DE LANNOY, G., DE ROSNAY, P., WALKER, J. P., FERRAZZOLI, P., MIRONOV, V., BIRCHER, S., GRANT, J. P., KURUM, M., SCHWANK, M., MUNOZ-SABATER, J., DAS, N., ROYER, A., AL-YAARI, A., AL BITAR, A., FERNANDEZ-MORAN, R., LAWRENCE, H., MIALON, A., PARRENS, M., RICHAUME, P., DELWART, S. & KERR, Y. 2017. Modelling the passive microwave signature from land surfaces: A review of recent results and application to the L-band SMOS & SMAP soil moisture retrieval algorithms. *Remote Sensing of Environment,* 192**,** 238-262.

WIGNERON, J. P., KERR, Y., WALDTEUFEL, P., SALEH, K., ESCORIHUELA, M. J., RICHAUME, P., FERRAZZOLI, P., ROSNAY, P. D., GURNEY, R. & CALVET, J. C. 2007. L-band Microwave Emission of the Biosphere (L-MEB) Model: Description and calibration against experimental data sets over crop fields. *Remote Sensing of Environment,* 107**,** 639-655.

WIGNERON, J. P., LAGUERRE, L. & KERR, Y. H. 2001. A simple parameterization of the L-band microwave emission from rough agricultural soils. *IEEE Transactions on Geoscience and Remote Sensing,* 39**,** 1697-1707.

WIGNERON, J. P., PARDE, M., WALDTEUFEL, P. & CHANZY, A. 2004. Characterizing the dependence of vegetation model parameters on crop structure, incidence angle, and polarization at L-band. *IEEE Transactions on Geoscience and Remote Sensing,* 42**,** 416-425.

WILHEIT, T. T. 1978. Radiative transfer in a plane stratified dielectric. *IEEE Transactions on Geoscience Electronics,* 16**,** 138-143.

WOODHOUSE, I. H. 2005. Introduction to microwave remote sensing. *Photogrammetric Record,* 24**,** E64-E74.

WU, T.-D., CHEN, K.-S., SHI, J., LEE, H.-W. & FUNG, A. K. 2008. A study of an AIEM model for bistatic scattering from randomly rough surfaces. *IEEE Transactions on Geoscience and Remote Sensing,* 46**,** 2584-2598.

XU, L., ABBASZADEH, P., MORADKHANI, H., CHEN, N. & ZHANG, X. 2020. Continental drought monitoring using satellite soil moisture, data assimilation and an integrated drought index. *Remote Sensing of Environment,* 250**,** 112028.

YAN, S., JIANG, L., CHAI, L., YANG, J. & KOU, X. 2015. Calibration of the L-MEB model for Croplands in HiWATER Using PLMR Observation. *Remote Sensing,* 7**,** 10878-10897.

YARDIM, C., JOHNSON, J. T., JEZEK, K. C., ANDREWS, M. J., DURAND, M., DUAN, Y., TAN, S., TSANG, L., BROGIONI, M. & MACELLONI, G. 2021. Greenland ice sheet subsurface temperature estimation using ultrawideband microwave radiometry. *IEEE Transactions on Geoscience and Remote Sensing,* 60**,** 1-12.

YE, N., WALKER, J., BINDLISH, R., CHAUBELL, J., DAS, N. N., GEVAERT, A., JACKSON, T. & RÜDIGER, C. 2019. Evaluation of SMAP downscaled brightness temperature using SMAPEx-4/5 airborne observations. *Remote Sensing of Environment,* 221**,** 363-372.

YE, N., WALKER, J. P., WU, X., JEU, R. D., GAO, Y., JACKSON, T. J., JONARD, F., KIM, E., MERLIN, O., PAUWELS, V. R. N., RENZULLO, L. J., RÜDIGER, C., SABAGHY, S., HEBEL, C. V., YUEH, S. H. & ZHU, L. 2020a. The Soil Moisture Active Passive Experiments: Validation of the SMAP products in Australia. *IEEE Transactions on Geoscience and Remote Sensing***,** 1-18.

YE, N., WALKER, J. P., YEO, I., JACKSON, T. J., KERR, Y., KIM, E., MCGRATH, A., POPSTEFANIJA, I., GOODBERLET, M. & HILLS, J. 2020b. Toward P-band passive microwave sensing of soil moisture. *IEEE Geoscience and Remote Sensing Letters***,** 1-5.

YOSHIOKA, K. 1989. Soil moisture gauge using terrestrial gamma-rays. *Nuclear Geophysics,* 3**,** 397-401.

YU, L., GAO, W., SHAMSHIRI, R. R., TAO, S., REN, Y., ZHANG, Y. & SU, G. 2021. Review of research progress on soil moisture sensor technology. *International Journal of Agricultural and Biological Engineering,* 14**,** 32-42.

YUAN, Q., SHEN, H., LI, T., LI, Z., LI, S., JIANG, Y., XU, H., TAN, W., YANG, Q. & WANG, J. 2020. Deep learning in environmental remote sensing: Achievements and challenges. *Remote Sensing of Environment,* 241**,** 111716.

YUAN, X., MA, Z., PAN, M. & SHI, C. 2015. Microwave remote sensing of short-term droughts during crop growing seasons. *Geophysical Research Letters,* 42**,** 4394-4401.

YUEH, S., SHAH, R., XU, X., ELDER, K. & STARR, B. 2020. Experimental demonstration of soil moisture remote sensing using P-band satellite signals of opportunity. *IEEE Geoscience and Remote Sensing Letters,* 17**,** 207-211.

ZENG, J. Y., LI, Z., CHEN, Q., BI, H. Y., QIU, J. X. & ZOU, P. F. 2015. Evaluation of remotely sensed and reanalysis soil moisture products over the Tibetan Plateau using in-situ observations. *Remote Sensing of Environment,* 163**,** 91-110.

ZHANG, D. & ZHOU, G. 2016. Estimation of soil moisture from optical and thermal remote sensing: A review. *Sensors,* 16**,** 1308.

ZHANG, L., ZHAO, T., JIANG, L. & ZHAO, S. 2010. Estimate of phase transition water content in freeze–thaw process using microwave radiometer. *IEEE transactions on geoscience and remote sensing,* 48**,** 4248-4255.

ZHANG, Y. 2020. *Towards improved crop growth and yield estimation: observation constrained wheat modelling*. Thesis, Monash University.

ZHAO, B., DAI, Q., ZHUO, L., ZHU, S., SHEN, Q. & HAN, D. 2021a. Assessing the potential of different satellite soil moisture products in landslide hazard assessment. *Remote Sensing of Environment,* 264**,** 112583.

ZHAO, T., HU, L., SHI, J., LÜ, H., LI, S., FAN, D., WANG, P., GENG, D., KANG, C. S. & ZHANG, Z. 2020a. Soil moisture retrievals using L-band radiometry from variable angular ground-based and airborne observations. *Remote Sensing of Environment,* 248**,** 111958.

ZHAO, T., SHI, J., ENTEKHABI, D., JACKSON, T. J., HU, L., PENG, Z., YAO, P., LI, S. & KANG, C. S. 2021b. Retrievals of soil moisture and vegetation optical depth using a multi-channel collaborative algorithm. *Remote Sensing of Environment,* 257**,** 112321.

ZHAO, T., SHI, J., LV, L., XU, H., CHEN, D., CUI, Q., JACKSON, T., YAN, G., JIA, L., CHEN, L., ZHAO, K., XINGMING, Z., ZHAO, L., ZHENG, C., JI, D., XIONG, C., WANG, T., LI, R., PAN, J. & ZHANG, Z. 2020b. Soil moisture experiment in the Luan River supporting new satellite mission opportunities. *Remote Sensing of Environment,* 240**,** 111680.

ZHAO, W. & LI, Z.-L. 2013. Sensitivity study of soil moisture on the temporal evolution of surface temperature over bare surfaces. *International Journal of Remote Sensing,* 34**,** 3314-3331.

ZHENG, D., LI, X., WANG, X., WANG, Z., WEN, J., VAN DER VELDE, R., SCHWANK, M. & SU, Z. 2019. Sampling depth of L-band radiometer measurements of soil moisture and freeze-thaw dynamics on the Tibetan Plateau. *Remote Sensing of Environment,* 226**,** 16-25.

ZHENG, D., LI, X., WEN, J., HOFSTE, J. G., VAN DER VELDE, R., WANG, X., WANG, Z., BAI, X., SCHWANK, M. & SU, Z. 2021. Active and passive microwave signatures of diurnal soil freeze-thaw transitions on the Tibetan Plateau. *IEEE Transactions on Geoscience and Remote Sensing*.

ZHENG, D., LI, X., ZHAO, T., WEN, J., VELDE, R. V. D., SCHWANK, M., WANG, X., WANG, Z. & SU, Z. 2020. Impact of Soil Permittivity and Temperature Profile on L-Band Microwave Emission of Frozen Soil. *IEEE Transactions on Geoscience and Remote Sensing***,** 1-14.

ZHENG, D., WANG, X., VAN DER VELDE, R., FERRAZZOLI, P., WEN, J., WANG, Z., SCHWANK, M., COLLIANDER, A., BINDLISH, R. & SU, Z. 2018. Impact of surface roughness, vegetation opacity and soil permittivity on L-band microwave emission and soil moisture retrieval in the third pole environment. *Remote Sensing of Environment,* 209**,** 633-647.

ZHENG, X., ZHAO, K. & ZHANG, S. 2012. Results of soil moisture inversion from radiometer biased by periodic change of row structure on farmland. *Journal of Remote Sensing,* 16**,** 1310-1230.

ZHU, L. 2019. *Towards multi-SAR-mission retrieval of soil moisture.* Thesis, Monash University.

ZHU, L., WALKER, J. P. & SHEN, X. 2020. Stochastic ensemble methods for multi-SAR-mission soil moisture retrieval. *Remote Sensing of Environment,* 251**,** 112099.

ZHU, L., WALKER, J. P., TSANG, L., HUANG, H., YE, N. & RÜDIGER, C. 2019a. A multi-frequency framework for soil moisture retrieval from time series radar data. *Remote Sensing of Environment,* 235**,** 111433.

ZHU, L., WALKER, J. P., TSANG, L., HUANG, H., YE, N. & RÜDIGER, C. 2019b. Soil moisture retrieval from time series multi-angular radar data using a dry down constraint. *Remote Sensing of Environment,* 231**,** 111237.

ZHU, L., WALKER, J. P., YE, N. & RÜDIGER, C. 2019c. Roughness and vegetation change detection: A pre-processing for soil moisture retrieval from multi-temporal SAR imagery. *Remote Sensing of Environment,* 225**,** 93-106.

ZREDA, M., DESILETS, D., FERRé, T. P. A. & SCOTT, R. L. 2008. Measuring soil moisture content non-invasively at intermediate spatial scale using cosmic-ray neutrons. *Geophysical Research Letters,* 35**,** L21402.

ZREDA, M., SHUTTLEWORTH, W., ZENG, X., ZWECK, C., DESILETS, D., FRANZ, T. & ROSOLEM, R. 2012. COSMOS: The cosmic-ray soil moisture observing system. *Hydrology and Earth System Sciences,* 16**,** 4079-4099.

ZWIEBACK, S., BOSCH, D. D., COSH, M. H., STARKS, P. J. & BERG, A. 2019. Vegetation–soil moisture coupling metrics from dual-polarization microwave radiometry using regularization. *Remote Sensing of Environment,* 231**,** 111257.